UNIVERSITY OF SOUTHAMPTON

FACULTY OF SCIENCE

Department of Physics and Astronomy

Engineering the magnetic properties of epitaxial RE - Fe_2 Laves phase alloy and multilayer films

by

Jean-Marc L. Beaujour

Thesis for the Degree of Doctor of Philosophy

August 2003

UNIVERSITY OF SOUTHAMPTON

ABSTRACT

FACULTY OF SCIENCE
DEPARTMENT OF PHYSICS AND ASTRONOMY

Doctor of Philosophy

ENGINEERING THE MAGNETIC PROPERTIES OF EPITAXIAL RE-Fe_2 LAVES PHASE ALLOY AND MULTILAYER FILMS

by Jean-Marc L. Beaujour

Epitaxial Laves phase based alloy and multilayer films grown by molecular beam epitaxy enable the study of the influence of epitaxial strain upon the magnetic properties of the materials. In particular, the temperature dependence of anisotropy constant of highly magnetostrictive materials such as $DyFe_2$ and $TbFe_2$ synthesized on a substrate is the signature of the built-in epitaxial strain effect.

The magnetisation reversal mechanism in $DyFe_2 - YFe_2$ multilayer and $DyFe_2$ / $TbFe_2$ alloy films can be described by the principle of coherent rotation. However, in the case of $DyFe_2 - YFe_2$ multilayer films, if the YFe_2 layer is sufficiently thick, the interfacial interaction give rise to the formation of magnetic exchange springs in the YFe_2 layer.

The $DyFe_2 - YFe_2$ superlattices form convenient model systems to study the effect of magnetic exchange springs, since the relative thickness of the $DyFe_2$ and YFe_2 layers are readily controlled in the growth process. Moreover, the magnetic exchange springs can be tailored to engineer novel magnetic phases such as negative coercivity, and magnetic compensation points.

Contents

List of tables and illustrations

Figure 4.2 Sketch of a bi-axial vector VSM. The magnet produces a magnetic field directed along the x-axis. One pair of sensing coils are parallel to the applied field and sense the magnetisation component longitudinal to the field $m_{\|} = m_x$. A 2nd set of coils is mounted at right angles to the applied field and senses the magnetisation component transverse to the field is $m_{\perp} = m_y$.

Figure 4.3 Photograph of a sample prepared for magnetisation measurements. The specimen is a 4000 Å epitaxial $DyFe_2$ film. The yellow disk is the film of Laves phase compounds. The green-ish part of the sample is the Nb-Fe buffer layer, which cannot be removed by the etching solution. The low temperature easy axis of the 4000 Å $DyFe_2$ film is shown versus one of the sample edges.

Figure 4.4
a) The magnetic hysteresis loop of a 4000 Å $DyFe_2$ epitaxial film, measured at 10 K. The dashed lines correspond to the primary M-B loop as given by the VSM. The diamagnetic sapphire substrate contribution is clearly apparent at high field. The solid line is the corrected M-B loop, which exhibits saturation feature for large applied field
b) The room temperature magnetic profile of a [100Å Nb / 30Å Fe] film, similar to the buffer layer found at the bottom of the epitaxial Laves phase superlattices. The negative slope of the linear feature is due to the diamagnetic nature of the sapphire substrate. The step at 0 T is clearly due to the 30 Å Fe seed layer. The curve displays a small hysteresis loop in low fields.

Figure 5.01 Schematic representation of a cubic crystal Laves phase deformed by a shear strain as observed in epitaxially grown RE-Fe_2 films.
a) The top picture shows the cubic Laves phase as found in bulk. At the bottom, the geometry of the RE-Fe_2 crystal strained by the sapphire substrate can be seen: $a_{\perp}^{s} < a_{\|}^{s}$.
b) Sketch of a single crystalline Laves phase in the bulk form.
c) Compression of the cubic crystal in the growth direction as a result of **(d)** its expansion in the film plane.

Figure 5.02 Selection of hysteresis loops of a 1000 Å thick epitaxial YFe_2 thin film. The magnetic field B_{app} is along the in-plane [001] direction. The larger magnetization of saturation is obtained at 10K, and it decreases with increasing temperature.

Figure 5.03 Room temperature hysteresis loops of epitaxial a 4000 Å thick YFe_2 film for different in-plane directions of the applied field. The magnetisation is in arbitrary unit (a.u).

Figure 5.04 The in-plane hysteresis loop of a 1000 Å MBE grown $DyFe_2$ film for different temperatures, and fields applied along an in-plane [001] direction. B_{irr} is the field from which the magnetisation reversal occurs.

Figure 5.05 Magnetic curves of single crystalline $DyFe_2$ thin film at 290 K, when the field is applied along different cubic crystallographic direction.

Figure 5.06 Coercivity for different angle between the applied field and the crystallographic direction for single crystalline $DyFe_2$ at 290 K.

Figure 5.07 $(B_C - B_{irr})$ as a function of temperature T for MBE grown $DyFe_2$ film. The dashed line is a linear fit of the evolution of $(B_C - B_{irr})$ versus T, for $T > 100$ K.

Figure 5.08 Magnetisation curves for single crystalline $TbFe_2$ at 290 K for magnetic field applied along different sample crystallographic axis.

Figure 6.1
a) The hysteresis loop of a single-domain particle. The magnetic field is applied along the easy axis. A, B, C and D designate the points of phase transition.
b) The geometrical configuration of a circular system of single domains particle. B_{app} is along the easy axis and the vector magnetisation M_{sat} rotates to the direction of the increasing magnetic field.

Figure 6.2
a) Sketch of the magnetisation arrangement of a magnetic 2-phase system: (*i*) and (*j*) are 2 single domain particles of magnetisation $M_{sat}^{(i)}$ and $M_{sat}^{(j)}$ respectively.
b) The system on the left is alternative-ly equivalent to a single domain particle with an easy axis which results from the combinaison of the uniaxial anisotropy of (*i*) and of (*j*).

Figure 6.3 The in-plane crystallographic directions of the (110) MBE grown $Tb_{(1-x)}Dy_xFe_2$ alloy films. The growth direction [110] (*i.e.* the *z* direction) is pointing out of the plane of the page.

Figure 6.4 Room temperature magnetisation data of a 4000 Å $Tb_{0.8}Dy_{0.2}Fe_2$ alloy film epitaxially grown.
a) Hysteresis loops. B_C is the coercive field and M_{rem} is the remanent magnetisation.
b) Polar plot of B_C for diverse direction of the applied magnetic field. (bullets).

Figure 6.5 Room temperature hysteresis curves of a series of epitaxially grown terfenol-type film $Tb_{(1-x)}Dy_xFe_2$: $DyFe_2$, $Tb_{0.27}Dy_{0.73}Fe_2$, and $TbFe_2$. All the films are 4000 Å thick. The field was applied along $[\bar{1}\,10]$.

Figure 6.6 Epitaxial strain in $Tb_{0.7}Dy_{0.3}Fe_2$ (110) thin film.
Thermal evolution of the crystallographic parameters $a_{\parallel}$, $a_{\perp}$ in epitaxial form of the Terfenol-D and a_{bulk}. Those parameters were deduced from neutron diffraction measurements [10]. The dotted lines are guides to the eyes.

Figure 6.7 The coercivity B_C of epitaxial $Tb_{(1-x)}Dy_xFe_2$ film as a function of the $DyFe_2$ concentration *x*, at room temperature. The solid line is the theoretical prediction based on Eq. 6.08.

Figure 6.8 Spin arrangements in $DyFe_2 - YFe_2$ multilayer system when the field is decreased from high positive value to 0 T.

Figure 6.9 Magnetometry measurements performed at 120 K with $\vec{B}_{app}$ along the [001] direction. The remanent magnetisation $\vec{m}_{rem}$ and the coercive field B_C are indicated.
a) 4000 Å $Dy_{0.5}Y_{0.5}Fe_2$ alloy film grown epitaxially.
b) Epitaxial [50Å $DyFe_2$ - 50Å YFe_2]×40 multilayer film.

Figure 6.10 A selection of the magnetisation curves for the superlattice samples [x $DyFe_2$ - (100-x) YFe_2]×40. The magnetic field B_{app} is applied along [001].
a) x = 80 Å **b)** x = 60 Å **c)** x = 45 Å

Figure 6.11 The experimentally determined easy axis coercivity B_C at 10 K, as a function of x/100 (bullets). The dashed line is a theoretical plot based on Eq. 6.12.

Figure 6.12 Temperature dependence of the coercivity B_C (bullets) for two superlattices. The temperature range covered is 10 K up to 260 K. The dashed lines represent the best fits of the data using the SDWP theory for temperatures below 150 K. The parameters B_C^0 and C determined from the fit are precised.

Figure 7.1 Low temperature (25K) hysteresis loop for an exchange spring coupled SmCo/Fe multilayer sample. The single and double arrows indicate respectively irreversible and reversible switching process. The related spin configurations are given in the inserts. [3]

Figure 7.2 The evolution of the angle θ_i in the monoatomic layer i as a function of the applied field. The soft phase, constitued of 31 monoatomic layers, is sandwiched between two infinite hard layers.

Figure 7.3 Schematic spin profile at the hard/soft phase interface.
The front of the drawing shows the approximate orientation of the TM spins in the soft layer. The background shows a plot of θ_i versus i.

Figure 7.4 The generalised reduced magnetisation $\langle\cos\theta\rangle$ plotted versus B_{app} / B_B. In zero field, the spins in the soft layer are anti-parallel to the field. So the reduced magnetisation is <cos θ> = -1.0

Figure 7.5 The hysteresis loop of [100Å $DyFe_2$ – 75Å YFe_2] × 23 multilayer sample at 100K. The coercivity B_C and the bending field B_B are indicated. The insert shows how B_B is experimentally determined from the M-B_{app} loop.

Figure 7.6 The temperature dependence of the the coercive field B_C and the bending field B_B of the multilayer sample: [100Å $DyFe_2$ – 75Å YFe_2] × 23.

Figure 7.7 Magnetometry measurements of a 4000 Å $Dy_{0.5}Y_{0.5}Fe_2$ alloy film grown by molecular beam epitaxy. The hysteresis loop was measured with the magnetic field applied along a [001] axis.

Figure 8.7
a) Schematic representation of the variation of the local anisotropy easy axis with position with weak exchange interaction between the magnetic moments.
b) Variation of the local anisotropy when a strong exchange interaction unbalances the local magneto-crystalline anisotropy.

Figure 8.8 M-B loop (B_{app} along [001] direction) at 20 K for multilayer samples with the thickness ratio x / $4x$ where:
a) x = 20, 30, 40 Å
b) x = 45, 50, 55 Å

Figure 8.9 Minor loops for [50 Å $DyFe_2$ / 200 Å YFe_2] × 16 at 20 K for various asymmetric magnetic cycles.

Figure 8.10 Dependence of the coercivity B_C with:
a) the thickness of the $DyFe_2$ layer, **b)** the maximum reversal field B_{irr}

Figure 8.11 The hysteresis loop at 20 K of the negative coercivity multilayer [50 Å $DyFe_2$ / 200 Å YFe_2] × 16. Also included is the spin arrangement at different applied field.
a) Development of magnetic exchange springs in the YFe_2 layer
b) Anti-ferromagnetic state
c) Magnetisation reversal and simultaneous formation of exchange springs
The large (small) arrows represent Dy (Fe) magnetic moments.

Figure 8.12 Selected hysteresis loop of [60 Å $DyFe_2$ / 240 Å YFe_2] × 13 when:
a) the temperature T is below 80 K **b)** the temperature T is above 100 K.
The field is applied in the [001] direction.

Figure 8.13 Magnetic behaviour of the multilayer [60 Å $DyFe_2$ / 240 Å YFe_2] × 13 at 100 K.
a) Hysteresis loop for positive applied field B_{app}.
b) First derivative of the magnetisation M versus B_{app}. M is the magnetisation when the field is swept from 0 to +12 T.

Figure 8.14 Partial hysteresis loop of the sample [60 Å $DyFe_2$ / 240 Å YFe_2] × 13, at 100 K. The sample is initially saturated along [001] by applying a large positive field. B_{min} is the maximum reversal field of the minor loop: B_{min} = -4 T, -6 T and -12 T.

Figure 8.15 Schematic representations of the magnetic moments and exchange springs in the configuration [60 Å $DyFe_2$ / 240 Å YFe_2] × 13 multilayer film for different value of the magnetic field (a, b, c, d).

Figure 8.16 Hysteresis loop of [60 Å $DyFe_2$ / 240 Å YFe_2] × 15 at 100 K, when the field is applied parallel to [001] and when it is applied parallel to [$\bar{1}$ 10]. The magnetisation is normalised by the value of the magnetisation at 12 T.

This thesis is dedicated affectionately to my parents,

Jeanne and Serge

Acknowledgements

As numerous people have given immeasurable amounts of time and effort over the last three years, without whom this PhD could not have happened, I would like to take this opportunity to thank all those who have helped me. Firstly, I would like to thank my supervisor Peter de Groot for giving me the opportunity to do this thesis research, and his guidance during the last three years.

Secondly, I would like to thank some members of the Magnetism and Superconductivity group to which I belonged for all the help and encouragement that they gave me: namely Graham Bowden (particularly for rendering my English writing more English, and much less French), Sergey Gordeev (for the numerous corrections he brought to my attention, all the advice and explanations that he patiently gave me), and Sasha Zhukov (for the stimulating discussions about magnetism). I must acknowledge that the work done could not be carried out without the active collaboration of the Oxford MBE Group, led by Drs. M. Wells and R. Ward.

This work was supported by QinetiQ (former DERA) at Farnborough (UK). I thank Dr. G. J. Tomka (QinetiQ) for useful discussions.

I also want to thank my family for their constant support. Finally, I must thank a couple of very interesting people I met during my PhD: Donald Kahari, Emanuele Di Nicolo, Mamadou Bah, Clarence Chongo, Teddy Chungu and Mathew Mwanza.

Also, I would like to thank some French fellows for their support during my two last years PhD: Floriane Bozon, Mia Komen, Coralie Lagrange, Melissa Remoue, Frantz Leroy.

Chapter 1

Introduction

Metallic superlattices and multilayers have been studied for more than 60 years [1]. However, until recently those investigations have had little impact on magnetism research. The breakthrough occurred during the early 1970's, when the considerable advances in vacuum technologies resulted in major progress being made in modern deposition methods. Using a variety of techniques, it has become possible to manipulate atomic planes, lines of atoms and small clusters to create new man-made materials engineered on an atomic scale.

One of these modern deposition methods is Molecular Beam Epitaxy (MBE). Originally, MBE was reserved for semi-conductor production. But in the late 1980's it was adapted to the preparation of magnetic multilayer films. It has revitalized basic research in magnetism [2, 3]. The MBE technique can be used to grow high purity epitaxial films. It has enabled the production of magnetic films which are artificially structured on the nanometre scale. In particular, it is possible to create layered systems with variable thicknesses made of single crystals or polycrystalline ferromagnetic, anti-ferromagnetic or paramagnetic materials. For example, multilayer films can be fabricated so that their properties are dominated by the interfaces contribution and structurally adjusted to meet desired characteristics [4]. The MBE synthesized structures display many novel properties compared to bulk materials. Since the physical dimensions of the layers are comparable to certain characteristic length scales, such as the electron wavelength or the length of exchange interaction, it is possible to engineer devices with specific properties [5]. Moreover, much of modern condensed matter materials physics, basic and applied, is

now based on the development of artificial materials in unusual configurations. Two important technological interests are the miniaturisation of magnetic read heads and new methods for increasing magnetic storage density. In addition, the excellent crystallographic structures and well defined dimensions imply that it is feasible to build theoretical models whose predictions can be compared to the experimental data with good accuracy.

Another important application is that of increasing the energy product (BH) of permanent magnet systems. Maximising this parameter requires identifying materials with a high saturation magnetisation M_{sat} and a high coercivity B_C in excess of $B_C > \pi M_{sat}$ [6]. Moreover, the desirable qualities of a permanent magnet material are a high remanence M_{rem}, and nearly linear 2nd quadrant B(H) characteristics. Fig. 1.1 reviews the development of permanent magnets with increasing $(BH)_{max}$ over the last century.

Alnico materials, developed in the 1930's were the first modern permanent compounds offering considerable magnetic hardness over the magnetic steels previously available. The manufacturing process consists in precipitating elongated Fe-Co ferromagnetic particles throughout the matrix of Al-Ni. Their properties rely on the shape anisotropy associated with the particles. They are characterised by a $(BH)_{max}$ of 1.5 - 7.5 MGOe, and display excellent corrosion resistance. Due to their high Curie temperature (~850°C), they are still used for certain applications nowadays. Nevertheless, they possess a low coercive force, meaning that they can be easily demagnetised, and must therefore be handled properly. In the mid 1950's, *ferrites* or *ceramic magnets* became commercially available. They are fine particle magnets produced by powder metallurgical methods. They exhibit high coercivities, nearly linear demagnetization curves, and a maximum energy product $(BH)_{max}$ of 1 - 3.5 MGOe. The magnetism of ferrites is founded in the high magneto-crystalline shape anisotropy of the particles. They constitute the most commercially important permanent magnets because of their low cost, and also because they are particularly well suited for many applications, including electric motors and capacitors [7].

However, it became apparent in the 1960's that attempts to further enhance or improve the magnetic properties of *ferrites* and *alnico* magnets were exhausted. The

search then began for other materials, with high uniaxial magneto-crystalline anisotropy, high coercivity, and high saturation magnetisation.

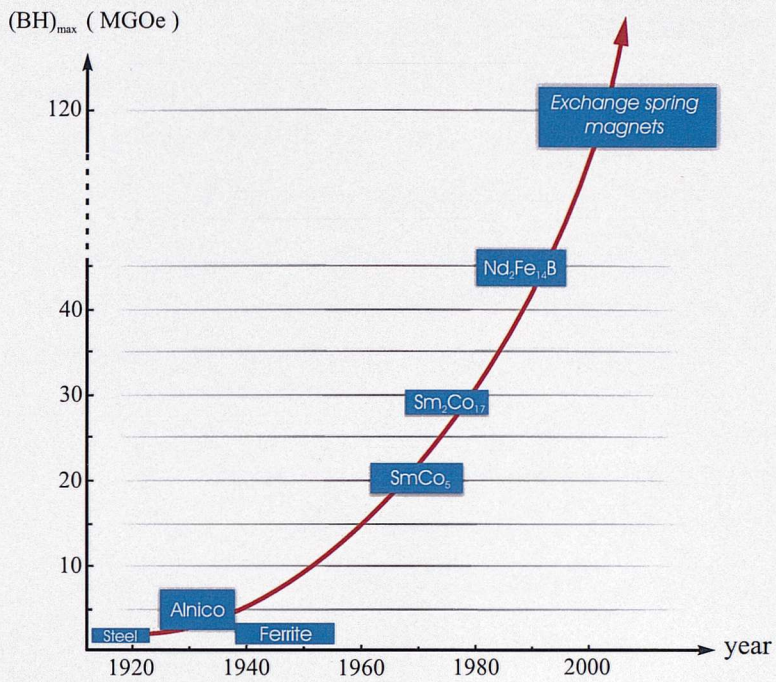

Figure 1.1 Progress in permanent magnets, with large maximum energy product $(BH)_{max}$, as a function of year.

Rare-Earth / Transition-Metal (RE-TM) intermetallic compound magnets represented the most promising candidates, and advances in the development of these magnetic materials over the last 40 years have had a profound and far-reaching impact on magnetic devices. Because RE metals have a low Curie temperature T_C (generally below ambient temperature), they are combined with elements that exhibit both good magnetic properties and high T_C (greater than 500 - 600 K), such as the transition elements of iron, cobalt or nickel. The RE-TM alloy magnets that have received the most attention include alloys of $SmCo_5$ and Sm_2Co_{17}. They exhibit a maximum energy product of 20 MGOe and 30 MGOe respectively. However, the cost and availability of the principle constituents in SmCo based materials limit their commercial success. So in the 1980's a considerable effort was expended to replace

scarce Co with abundant Fe in combination with RE metals. This, ultimately, leads to the development of NdFeB based magnets, with $(BH)_{max} \geq 40$ MGOe. The $Nd_2Fe_{14}B$ compound delivers the highest performance ever achieved industrially to date, *i.e.* a maximum energy product of 45 MGOe.[1]

More recently, the properties of layered magnets, at the nano-atomic level, have attracted much attention [6, 8-14]. The underlying reason for this interest stems from the work of Coey and Skomski [9] who have argued, on theoretical grounds, that nano-structured magnets with a giant energy product of 120 MGOe might be feasible, if the exchange spring mechanism in those materials could be suppressed. Exchange springs magnets are based on the interfacial coupling of soft and hard ferromagnetic nano-composites. The hard phase, usually a binary or ternary RE–TM intermetallic compound, provides high magnetic anisotropy and coercive fields. The magnetically soft phase (a TM), is pinned by the hard phase through the strong exchange coupling. The FM coupling between hard/soft phase leads to an enhancement of the magnetisation, with the added benefit of reducing the overall RE content. To induce strong exchange coupling, the soft phase must have a high Curie temperature ($T_C^{(Fe)} \sim 1000$ K). One of the technological advantages of exchange spring magnets is that they contain less RE content than single component hard RE-TM intermetallics, which lowers the cost of materials while improving corrosion resistance.

Commercial interests entail that the research into exchange springs magnets is mainly directed towards nano-dispersed hard and soft magnetic phase structures such as SmCo-TM (TM = Co, Fe) [10, 15-19]. The magnets are fabricated by rapid quenching and subsequent annealing or mechanical alloying to form a nano-composite with randomly oriented hard grains [11, 12].

As mentioned earlier, magnetic exchange springs have been mainly investigated in ferromagnetically coupled structures, and studies of anti-ferromagnetically coupled multilayer films are rarer. In this thesis, the magnetic properties of epitaxial Laves phase multilayer films $DyFe_2$ - YFe_2 have been investigated. This essentially 2-D system is ideal for the investigation of the physics of magnetic exchange springs in

[1] Recently, *Magnetic Component Engineering Inc.* has announced that *N5062* a sintered, high energy product NdFeB permanent magnet alloy is available. It is guaranteed to have a maximum energy product of 50 MGOe. (http://www.magneticcomponent.com)

an anti-ferromagnetically coupled layered system. In particular, it avoids the structural complexities of the random two phase 3-D system discussed by Coey [6, 9].

The aim of this work is to propose a solid experimental and theoretical framework for the understanding of how to use the characteristics of the single Laves phase materials in order to synthesize RE-Fe_2-based nano-composite structures with novel magnetic properties.

The magnetisation reversal mechanism of the $DyFe_2$ – YFe_2 multilayer films and the epitaxially strained $Tb_{(1-x)}Dy_xFe_2$, is studied. Interest of the Laves phase RE-Fe_2-type material arises from the strong exchange of the transition metal and the large magnetostriction of the RE.

To elucidate the magnetic properties of the epitaxial Laves phase multilayer and alloy films, it is important to understand first the basic of magnetism in RE Laves phase. The origin of their magnetic properties is reviewed in chapter 2.

The growth of the epitaxial single phase RE-Fe_2 films is described in chapter 3. In particular, a brief review of the MBE method is given, together with why well ordered single crystal RE-Fe_2 films can be stabilized on sapphire substrate.

In chapter 4, the epitaxial RE-Fe_2 Laves phase (RE = Dy, Y, Tb) are magnetically characterised. The effect of the strain induced by the substrate on the magnetic properties of the Laves phase films is also reported, since this has an important effect on the magnetic properties of the film [20]. Finally, the crystallographic characteristics of the bulk RE-Fe_2 material are compared to those of the epitaxially grown films.

In chapter 5, the experimental methods used to characterise the magnetic films are detailed. The design and the principle of the Vibrating Sample Magnetometer, the main investigatory technique used in this work for the magnetic measurements, are explained. Also, the preparation of the samples for the measurements is described.

In chapter 6, the magnetic measurements of exchange coupled $DyFe_2$ - YFe_2 multilayer films with thin YFe_2 layer, and of epitaxially strained $Tb_{(1-x)}Dy_xFe_2$ alloy films are presented and discussed. The magnetic switching behaviour in both the systems is investigated, and it is shown how to engineer their coercivity. In addition,

the simplest model of nucleation mechanism in single phase materials by Stoner and Wohlfarth [21] is reviewed, and it is generalised to heterophase structures. Theoretical predictions are then compared to the experimental data.

The formation of magnetic exchange springs in the anti-ferromagnetically coupled $DyFe_2$ - YFe_2 multilayer films is detailed in chapter 7. It is shown that the bending field, the onset of the magnetic exchange spring, can be engineered by varying the thickness of the layers. A one-dimensional model is used to describe the magnetic spin configuration in the multilayer films. Finally, it is proved that the magnetic properties of a variety of exchange springs can be expressed in a universal form.

Given that the relative thickness of the magnetically hard and soft layers is readily controlled by the growth process, the impact of micro-structural changes upon the magnetic profile of the exchange springs $DyFe_2$ - YFe_2 films can be investigated. In chapter 8, the effects of the magnetic exchange springs on the irreversible switching field of the superlattices are presented and discussed. It is shown that it is possible to engineer multilayer films which possess negative coercivities. In addition, it is also possible to grow films that are magnetically compensated. Practical applications for such magnetic systems are proposed.

Finally, the findings of this work are summarized.

References

[1] J. W. H. duMond and J. P. Youtz, *Phys. Rev.* **48**: 127 (1935)

[2] M. N. Baibich, *et al.*, *Phys. Rev. Lett.* **61**: 2472-2475 (1998)

[3] J. Nogues and I. K. Schuller, *J. Magn. Magn. Mater.* **192** (2): 203-232 (1999)
A. E. Berkowitz and K. Takano, *J. Magn. Magn. Mater.* **200**: 552-570 (1999)

[4] B. Dieny *et al.*, *Phys. Rev. B* **43** (1): 1297-1300 (1991)

[5] M. Hehn, *Science* **272**: 1782 (1996)
T. Aign, *Phys. Rev.* **81**: 5656 (1998)
W. Weber, *Phys. Rev. B* **54**: 4075 (1996)

[6] J. M. D. Coey, *Solid State Commun.* **102** (2-3): 101-105 (1997)

[7] ASM Handbook, vol. 2, Properties and Selection: *Nonferrous Alloys and Special Purpose Materials*, ASM International, Materials Park, OH, 1990, pp. 788-792

[8] E. F. Kneller and R. Hawig, *IEEE Trans. Magn.* **27**: 3588-3600 (1991)

[9] R. Skomski and J. M. D. Coey, *Phys. Rev. B* 48 (21): 15812-15816 (1993)
R. Skomski, *J. Appl. Phys.* **76** (10): 7059-7064 (1994)
J. M. D. Coey and R. Skomski, *Phys. Script.* **T49A**: 315-321 (1993)

[10] T. Schrefl *et al.*, *J. Magn. Magn. Mater.* **127** (3): L273-L277 (1993)

[11] L. Withanawasam *et al.*, *J. Appl. Phys.* **75** (10): 6646-6648 (1994)

[12] J. Ding *et al.*, *J. Magn. Magn. Mater.* **124** (L1) (1993)

[13] I. A. Al Omari and D. J. Sellmyer, *Phys. Rev. B* **52** (5): 3441-3447, 1995

[14] M. Shindo *et al.*, *J. Magn. Magn. Mater.* **161** (L1) 1996

[15] R. Coehoorn *et al.*, *J. Magn. Magn. Mater.* **80** (1): 101-104 (1989)

[16] K. O'Donnell *et al.*, *J. Appl. Phys.* **76** (10): 7068-7070 (1994)

[17] J. M. Yao *et al.*, *J. Appl. Phys.* **76**: 7071-7073 (1994)

[18] K. Ounadjela and G. Suran, *J. Appl. Phys.* **63** (8): 3244-3246 (1988),

[19] S. Hirosawa *et al.*, *J. Appl. Phys.* **73** (10): 6488-6490 (1993)

[20] M. Mougin *et al.*, *Phys. Rev. B* **62**: 9517-9531 (2000)

[21] E. C. Stoner and E. P. Wohlfarth, *Phil. Trans. R. Soc.* **240**: 599-642 (1948)

Chapter 2

Magnetism in Rare Earth and RE-Fe_2 Laves phase compounds

Prior to the 1950's, the study of Rare Earth (RE) materials was scant because of the difficulty of chemically isolating them. But in the early 1950's, F. H. Spedding resumed his programme of producing the pure elements in relatively large quantities. Then, extensive measurements were carried out on polycrystalline samples of all the stable RE's through the 1950's, and summarised by Spedding et al. [1] at the close of this early period of RE research.

In this chapter, some of the principles of magnetism are reviewed, with particular emphasis on the RE and RE transition metal intermetallic compounds.
In the first section, the 'origin' of the magnetism, in both RE's and transition metals, is explained at the atomic level. Subsequently, the influence of the crystal field interaction at the RE ions, upon the magnetic anisotropy is briefly described. Particular attention is paid to the RE-Fe_2 compounds, whose study forms the basis of this thesis. Finally, the magneto-elasticity of the RE-Fe_2 intermetallic compounds is reviewed.

2.1 The origin of spontaneous magnetisation

Electrons possess both orbital and spin angular momenta ($\underline{\ell}$, $\underline{s}$), which also carry magnetic moments ($g_\ell \mu_B \underline{\ell}$, $g_s \mu_B \underline{s}$) respectively. From the periodic table point of view, the electrons can be viewed as occupying *shells*. The layers designated by the letters *s*, *p*, and *d* refer to the orbital angular momentum $\ell = 0$, 1, 2 respectively. In the ground state of an atom, the states are 'filled' in order of increasing energy, *i.e.* the first electron goes into the lowest energy state, the second into the next lowest, and so on. The diagram shown Fig. 2.1 is one way to illustrate the order of filling of the electron energy states.

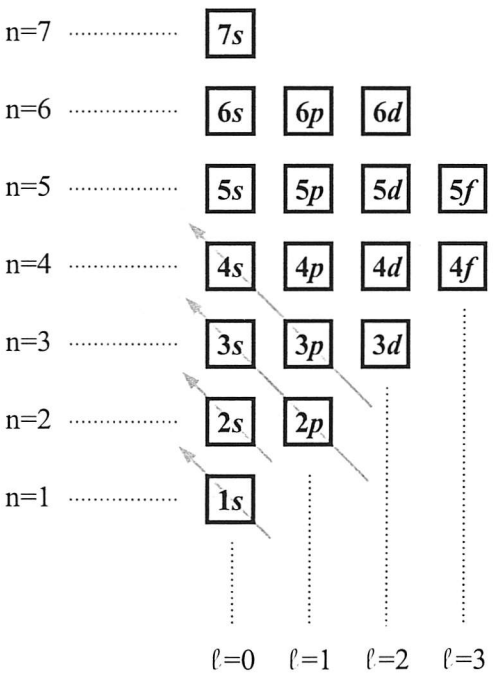

Figure 2.1 The order in which the shells are filled up. The filling starts from the bottom right to the top left of the table as indicated by the arrows. [2]

In filling these shells, two rules must be followed. The first rule is the maximisation of the spin angular momentum $\underline{S}$, as dictated by the Pauli exclusion principle: two electrons on the same shell must have their spin aligned anti-parallel. This prevents two electrons of the same spin from being at the same place at the same time. The

second rule is the maximisation of the orbital angular momentum L. According to Hund's rule, the spins of unpaired electrons must align parallel to prevent two electrons from occupying the same orbital. By occupying orbitals with different magnetic quantum number, the Coulombic repulsion energy between electrons is reduced, resulting in a more stable system.

In many atoms, the electronic spins and moments are 'paired off', giving no net atomic magnetic moment and leading to diamagnetism. However, in the case of partially filled shells, the atom shows a net magnetic moment m:

$$\vec{m} = -g\,J\,\mu_B \tag{2.01}$$

where $g = [1 + (J(J+1)+S(S+1)-L(L+1))/(2J(J+1))]$ is called Landé's splitting-factor and $\mu_B = e\hbar/2m_e$ is the Bohr magneton. J is the the total angular momentum, which is equal to |L - S| when the shell is less than half full and to |L + S| when the shell is more than half full. When the shell is just half full, the application of the first rule gives L = 0, so that J = S.

In a magnetic solid, the overlap of magnetic spin wavefunction gives rise to the coupling between neighbouring magnetic moments via the so-called exchange interaction W_{ij}:

$$W_{ij} = -2J_{ex}\,\vec{s}_i \bullet \vec{s}_j \tag{2.02}$$

If J_{ex} is positive, adjacent moments are aligned parallel and the material is called a ferromagnet. If J_{ex} is negative, adjacent moments are aligned anti-parallel and the system can be divided into two sublattices with opposite magnetisation direction. If the sublattices have equal magnetisation the material is called anti-ferromagnet. Otherwise, it is called ferrimagnet. (Fig. 2.2)

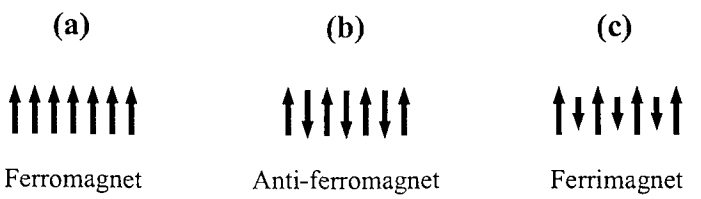

Figure 2.2 The main types of ordered magnetic structures.

As temperature increases, the aligning effect of the exchange interaction is partly offset by the lattice vibrations. At the Curie temperature T_C, the thermal energy is high enough to disrupt the spin alignments, and the material becomes paramagnetic.

In the periodic table, there are 5 groups of magnetic materials in which an electron shell is incompletely filled:

1) the transition metal group (incomplete 3*d* shell)
2) the palladium group (incomplete 4*d* shell)
3) the lanthanides group (incomplete 4*f* shell)
4) the platinum group (incomplete 5*d* shell)
5) the actinide group (incomplete 5*f* shell)

In this thesis, we shall be concerned primarily with groups 1 and 3.

2.1.1 The transition metals

Elemental Fe contains 26 electrons distributed from the inner-most shell 1*s* to the outermost shell 4*s*. In the ionic form, Fe^{2+} for example, it is characterised by the configuration $3d^6$, where the 3*d* shell becomes the outer-most electronic shell. Fig. 2.3 shows the relative energy distribution of electrons in the Fe^{2+} ion.

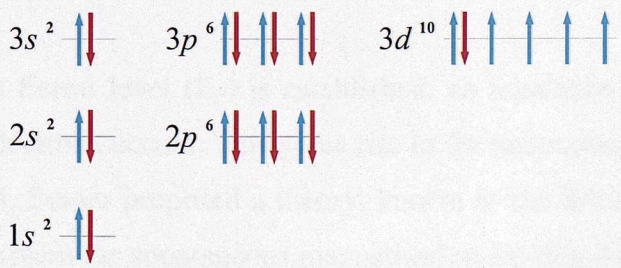

Figure 2.3 Schematic representation of the relative energy levels of the 24 electrons in the Fe^{2+} ion. The direction of the arrows indicates the two possible spin orientations.

All the shells from ($1s^2$) to ($3p^6$) are filled, and therefore cannot give rise to a magnetic moment. However, the $3d$ layer is only partially filled with 6 electrons, out of a possible 10 eigenstates.

In a solid, instead of having discrete energies as in the case of free ions, the available energy states form bands, containing an enormous number of possible energy levels. The Weiss molecular interaction field shifts the density of states $D_S(E)$ of the spin up and spin down bands relative to each other as shown schematically in Fig. 2.4.

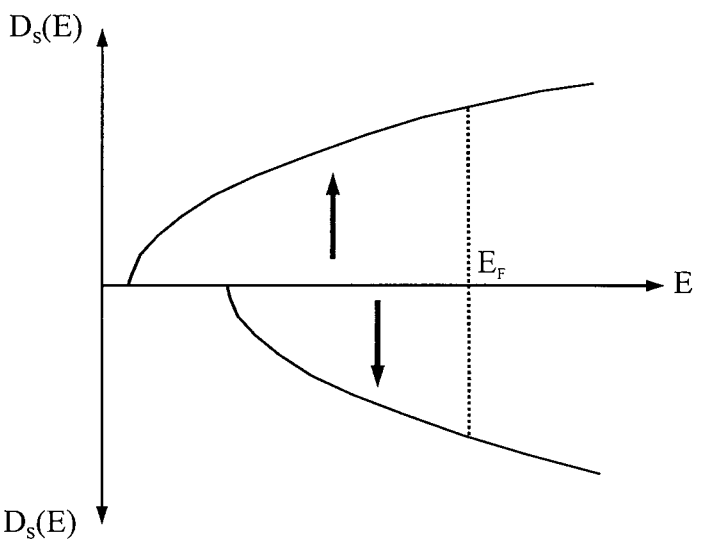

Figure 2.4 Schematic representation of the relative shift of the density of states of the spin up and spin down bands.

Once a common Fermi level (E_F) is established, an inbalance between the spin up and spin down electrons occurs. This gives rise to the spontaneous magnetic moment. As early as 1938, Stoner proposed a theory, known as the Stoner model or the rigid band model to explain the spontaneous magnetisation exhibited by $3d$ metals. [3] Initially, one assumes the electrons are free. A magnetic field B_{app} is applied and leads to the splitting of the density of states of the two spin bands. If $\mathcal{N}$ is the total number of electrons:

$$\mathcal{N} = \mathcal{N}_{\uparrow} + \mathcal{N}_{\downarrow} \tag{2.03}$$

($\mathcal{N}_\uparrow$, $\mathcal{N}_\downarrow$ are the number of spin up and spin down electrons respectively), and the spin polarisation $\mathcal{S}$ is defined as:

$$\mathcal{S} = \frac{\mathcal{N}_\uparrow - \mathcal{N}_\downarrow}{\mathcal{N}_\uparrow + \mathcal{N}_\downarrow} \tag{2.04}$$

then, to the extent that the splitting is small so $D_S(E)$ can be replaced by $D_S(E_F)$, the energy E_B of the electrons in the band is given by [4]:

$$E_B = \frac{\mathcal{N}^2}{4D_S(E_F)}\mathcal{S}^2 - \mu_0\mu_B\mathcal{N}B_{app}\mathcal{S} \tag{2.05}$$

The equilibrium polarisation is the one that will minimise E_B. The magnetisation is:

$$M = \frac{\mu_B\mathcal{N}\mathcal{S}}{\Omega_T} \tag{2.06}$$

where Ω_T is the volume per metal atom.

Stoner proposed that the exchange interaction among the electrons be paramatrized phenomenologically by:

$$E_{ex} = -\frac{I}{4}\left(\mathcal{N}_\uparrow - \mathcal{N}_\downarrow\right)^2 \tag{2.07}$$

where I is the so-called Stoner parameter. It describes the energy reduction due to the electron correlation.

By adding the Stoner term E_{ex} to the band energy E_B, the energy of the band:

$$E_B = \frac{\mathcal{N}^2}{4}\left(\frac{1}{D_S(E_F)} - I\right)\mathcal{S}^2 - \mu_0\mu_B\mathcal{N}B_{app}\mathcal{S} \tag{2.08}$$

shows that one can have spontaneous magnetisation ($\mathcal{S}$ non vanishing with B_{app}=0) if:

$$D_S(E_F)I > 1 \tag{2.09}$$

Eq. (2.09) is known as the Stoner criterion, and it is perfectly verified in the case of Fe, Co and Ni.

In the Stoner model, a rigid shift of the density of states of the spin up and spin down band occurs: the bands are not a function of magnetisation. More sophisticated versions take account of how the density of states varies with magnetisation. [5]

2.1.2 The lanthanides group

The Lanthanides or Rare Earths belong to the elements starting from La with an atomic number of 57, and ending with Lu with an atomic number of 71. They are often grouped with Yttrium which has similar chemical characteristics.
In practice, almost all the RE atoms have the same outer electronic structure of $5s^2\ 5p^6\ 5d^1\ 6s^2$ [6]. $5d^1 6s^2$ are valence electrons leading to RE^{3+} ion, and in metals they become conduction electrons. In similar circumstances to the TM, the outer-most shells are filled before the $4f$ shell. Thus, the magnetic properties of the RE ions are determined by the occupancy of the strongly localised $4f$ electronic shells, while the outer *s-p* electrons are usually involved with bonding and other electronic properties [7, 8].

For RE, the magnetic spin is:

$$\vec{s}_i = (g-1)\vec{\mathrm{J}}_i \tag{2.10}$$

and so the exchange interaction W_{ij} can be written:

$$W_{ij} = -2(g-1)^2 J_{ex} \vec{\mathrm{J}}_i \bullet \vec{\mathrm{J}}_j \tag{2.11}$$

Among the RE series, it shall be distinguished 2 groups [9]:

- the heavy RE (*e.g.* Holmium) are the elements with a $4f$ shell that is more than half full. The spin $\underline{S}$ and orbit $\underline{L}$ are anti-parallel: $\underline{J} = \underline{L} + \underline{S}$.
- the light RE (*e.g.* Praseodynium) are the elements with a $4f$ shell that is more than half full. The spin $\underline{S}$ and orbit $\underline{L}$ are parallel: $\underline{J} = \underline{L} - \underline{S}$

In RE metals, the magnetic order occurs below ambient temperature. At ambient temperature, they are paramagnetic. For example, the Gd ferromagnetism appears at temperatures below 293 K.

2.2 Spin-orbit coupling and crystal fields in 3*d* and 4*f* metals

The total Hamiltonian $\mathcal{H}$ of an elemental ion or atom incorporated in a solid is given by:

$$\mathcal{H} = \mathcal{H}_C + \mathcal{H}_{S\text{-}O} + \mathcal{H}_{C\text{-}F} \tag{2.12}$$

Where $\mathcal{H}_C$ represents the Hamiltonian associated with the electrostatic interactions which couple the moments in the multi-electrons atom or ion. $\mathcal{H}_{S\text{-}O}$, known as the spin-orbit coupling, describes the interaction between $\underline{L}$ and $\underline{S}$:

$$\mathcal{H}_{S\text{-}O} = \lambda \underline{L} \bullet \underline{S} \tag{2.13}$$

where λ is the spin-orbit coupling constant.

$\mathcal{H}_{C\text{-}F}$ represents the electrostatic interaction with the surrounding atoms or ions and is known as the crystal field. In general, the charge clouds of the electrons align along a particular symmetry axis of the crystal, and remain fixed with respect to it. Thus, the orbital moments $\underline{L}$ can be strongly coupled to the lattice by the crystal field. When a large number of Fe ions for instance, are assembled in a solid, the electrons of the 3*d* shell are exposed directly to the intense crystal field. It results in the disappearance of the orbital angular momentum, a phenomenon known as *quenching*: $\underline{J} \sim \underline{S}$ and $g = 2$. In practice, the 3*d* elements are characterised by $\mathcal{H}_{S\text{-}O} << \mathcal{H}_{C\text{-}F}$. The crystal field exerts a greater influence on $\underline{L}$ than does the spin-orbit coupling. For RE, this is not the case, partly because the spin-orbit forces are greater than in free iron group ions, and partly because the incompletely filled 4*f* shell is 'screened' from the crystal fields by the 5*s* and 5*p* electrons. The RE materials are characterised by $\mathcal{H}_{S\text{-}O} >> \mathcal{H}_{C\text{-}F}$.

As it will be seen in the next section, the crystal fields are of great significance in determining the behaviours of magnetic ions.

2.3 The magnetic anisotropy of TM and RE elements

Besides the exchange energy that makes the moments tend to be parallel or anti-parallel to each other, there is an energy that makes the magnetisation lie along certain crystallographic directions, so-called easy directions. This energy is called the magneto-crystalline anisotropy energy (MAE).

Furthermore, the magnetic response of materials to strain and stress, via the magneto-elastic energy (MEL), can affect the directions of easy magnetisation. Another source of magnetic anisotropy is the shape anisotropy. It originates from the long-range dipolar interaction, which senses the outer shape of the sample. It is important in thin films and often produces in-plane alignment.

2.3.1 The magneto-crystalline anisotropy

The main cause of the MAE term is the spin-orbit interaction (Eq. 2.13). Since the spins of the magnetic ions are coupled to the orbital clouds of the electrons through spin-orbit coupling, the symmetry of the crystal lattice is felt by the magnetic ion even though the orbital angular momentum itself may be small. Thus, different orientations of the spins with respect to the lattice vectors yield different interaction energies.

For 3*d* elements, there usually are some remaining unquenched orbitals which couple the spin moment to some directions in space.

The two most common types of MAE's are cubic and uni-axial. For cubic systems, it can be written [10]:

$$E_{mc}^{cubic} = K_1(\alpha_x^2\alpha_y^2 + \alpha_x^2\alpha_y^2 + \alpha_x^2\alpha_y^2) + K_2\alpha_x^2\alpha_y^2\alpha_z^2 + \ldots \qquad (2.14)$$

where α_i are the directional cosines of the magnetisation vector with respect to the crystallographic axes. K_1 and K_2 are the first and second order anisotropy constants respectively. K_1 is given by [11]:

$$K_1 \approx J_{ex}(g_J - 2)^4 \tag{2.15}$$

with $(g_J - 2)$ is the degree of quenching [12] and J_{ex} is the exchange constant.
For a uniaxial system, the MAE can be written:

$$E_{mc}^{uniaxial} = K_u \sin^2\theta \tag{2.16}$$

where K_u is the uniaxial anisotropy constant, and θ is the angle between the magnetisation vector and the easy axis.
The directions of easy magnetisation of a cubic or uniaxial magnetic system can be determined by minimising the MAE using (Eq. 2.14) or (Eq. 2.16).

Due to the respective strengths of the spin-orbit coupling, magneto-crystalline anisotropy is generally more pronounced in 4*f* compounds than in 3*d*. RE materials are characterised by magneto-crystalline anisotropy which is 10 to 100 times greater than those normally encountered in TM.
The electron-electron interactions in the RE-based solid due to the electrostatic interaction of the aspherical 4*f* charge distribution with the aspherical electrostatic field arising from the surrounding, is described by the crystal field Hamiltonian $\mathcal{H}_{C\text{-}F}$.
Within the Stevens formalism, $\mathcal{H}_{C\text{-}F}$ can be written:

$$\mathcal{H}_{C\text{-}F} = \sum_{n}^{\infty}\sum_{m=0}^{n} B_n^m O_n^m \tag{2.17}$$

where B_n^m are called the crystal field parameters and include terms related to the 4*f* ion and term related to the surrounding charges [13]. O_n^m are the Stevens operators: they have same transformation under rotation operations as the spherical harmonics, *e.g.* $O_2^0 = 3J^2 - J(J+1)$.

For cubic symmetry, like Laves phase RE-Fe_2, the crystalline electric field is described by the parameters B_4 and B_6 [14]

$$\mathcal{H}_{C\text{-}F} = B_4(O_4^0 + 5O_4^4) + B_6(O_6^0 - 21O_4^6) \tag{2.18}$$

The expression of the operators O_4^0, O_4^4, O_6^0 and O_4^6 versus J, J_x, J_y and J_z can be found in Ref. [8].

Bleany has evaluated the appropriate crystal-field Hamiltonian for the RE ions on the basis of a point-charge model, by taking into account the four nearest-neighbour RE ions and the twelve next nearest iron ions [14].

The anisotropy energy E_{mc} can be expressed within the framework of the model of magnetic anisotropy given by Callen and Callen [15] in the form:

$$\begin{aligned} E_{mc}^{RE\text{-}Fe_2}(\theta,\varphi) = &\frac{1}{8}\tilde{K}_0^4\left[(5\cos 4\theta + 3) - 5\sin^4\theta(1-\cos 4\varphi)\right] \\ &+\frac{1}{16}\tilde{K}_0^6\left[(21\cos 4\theta - 5) + 21(11\cos^2\theta - 1)\sin^4\theta(1-\cos 4\varphi)\right] \end{aligned} \tag{2.19}$$

where θ and φ are the polar angles of the magnetisation $\vec{M}$, referred to the cubic axes, and $\tilde{K}_0^4$ and $\tilde{K}_0^6$ are the 4th and 6th order tensor anisotropy coefficients:

$$\tilde{K}_0^n = B_n\left\langle O_0^n \right\rangle \tag{2.20}$$

Thus, the sign and magnitude of $\tilde{K}_0^n$ is determined primarily by the crystal field coefficients B_n.

To draw an analogy with the conventional expression for the magnetic anisotropy energy of a cubic crystal (Eq. 2.14), it is observed [16]:

$$\begin{aligned} K_1 &= -5\tilde{K}_0^4 - \frac{21}{2}\tilde{K}_0^6 \\ K_2 &= \frac{231}{2}\tilde{K}_0^6 \end{aligned} \tag{2.21}$$

2.3.2 The magneto-elastic effect

There are two related effects of stress and strain in a magnetic material [17]:

- the variation of strain with the direction or magnitude of the magnetisation, and
- the introduction of anisotropy in the magnetic material due to the presence of stress.

The dependence of crystalline anisotropy on strain is the basic origin of magnetostriction. The phenomenon provides a coupling of the magnetisation vector

with the lattice. Therefore, spin-orbit coupling must exist for there to be magnetostriction. [18]

The very first positive identification of magnetostriction was in 1842 when James Joule observed that a sample of nickel changes in length when it is magnetised. Subsequently, cobalt, iron and alloys of these materials were found to show a significant magnetostriction.

Because of their moderate elastic constants and the large orbital component in their moments, the RE metals show the largest known magnetostriction. In the 1960's, the RE elements terbium (Tb) and dysprosium (Dy) were found to have between 100 and 10,000 times the magnetostrictive strains found in nickel alloys.

The strain dependence of the magnetic anisotropy energy E_a can be expanded as [19]:

$$E_a = E_{mc}(\alpha_i) + E_{me}(\alpha_i \varepsilon_{ij}) + \ldots \tag{2.22}$$

where ε_{ij} are the elements of the strain tensor ($i,j = x, y, z$). ε_{ii} are compressive or tensile strain components, and ε_{ij} are shear strain components.

The first term corresponds to the anisotropy of the undistorted lattice, *i.e.* the MAE. The second term represents the magneto-elastic energy density, which for a cubic crystal may be expanded as [19]:

$$\begin{aligned} E_{me} = {} & b_0(\varepsilon_{xx} + \varepsilon_{yy} + \varepsilon_{zz}) + b_1(\alpha_x^2\varepsilon_{xx} + \alpha_y^2\varepsilon_{yy} + \alpha_z^2\varepsilon_{zz}) \\ & + b_2(\alpha_x\alpha_y\varepsilon_{xy} + \alpha_x\alpha_z\varepsilon_{xz} + \alpha_y\alpha_z\varepsilon_{yz}) \end{aligned} \tag{2.23}$$

The constants b_0, b_1, b_2 are the magneto-elastic coefficients.

To these energy terms must be added the elastic energy density:

$$\begin{aligned} E_e = {} & \tfrac{1}{2}C_{11}(\varepsilon_{xx}^2 + \varepsilon_{yy}^2 + \varepsilon_{zz}^2) + C_{12}(\varepsilon_{xx}\varepsilon_{yy} + \varepsilon_{yy}\varepsilon_{zz} + \varepsilon_{xx}\varepsilon_{zz}) \\ & + \tfrac{1}{2}C_{44}(\varepsilon_{xy}^2 + \varepsilon_{yz}^2 + \varepsilon_{xz}^2) \end{aligned} \tag{2.24}$$

where C_{11}, C_{12} and C_{44} are the cubic elastic stiffness constants.

b_1 and b_2 are related to the more usual magneto-strictive coefficients λ_{111} and λ_{100} by the relations:

$$\begin{aligned} b_1 &= -\tfrac{3}{2}\lambda_{100}(C_{11} - C_{12}) \\ b_2 &= -3\lambda_{111}C_{44} \end{aligned} \tag{2.25}$$

λ_{100} and λ_{111} are the saturation magneto-striction constants along the respective <100> and <111> axes.

The stress components are given in terms of the strain components σ_{ij} by the matrix relation: $[\varepsilon_{ij}] = [C_{ij}]^{-1} \times [\sigma_{ij}]$. The minimum energy is found by taking the partial derivatives of E_{me} and E_e with respect to the strain components and setting the derivatives equal to zero,

$$\varepsilon_{ii} = b_1 \frac{C_{12} - \alpha_i^2 (C_{11} + 2C_{12})}{(C_{11} - C_{12})(C_{11} + 2C_{12})}$$
$$\varepsilon_{ij} = -\frac{b_2 \alpha_i \alpha_j}{C_{44}} \qquad (2.26)$$

This result is a formal explanation of magnetostriction since it shows a spontaneous strain depending on the direction of the magnetisation as characterised by the direction cosines.

2.4 The Laves phase materials

In general, the RE metals are characterised by a large magnetic moment per atom and a large degree of magnetostriction. They also provide strong magneto-crystalline anisotropy. However, they exhibit paramagnetic behaviour above room temperature [20]. In order to increase the Curie temperature T_C, RE elements have been combined with transition elements of iron, cobalt or nickel. The Laves phase is the group constituted of the RE-Fe_2 intermetallics. The Fe component provides high Curie temperature (~1000°C) [21], while the RE elements give strong anisotopic behaviour [22]. The electronic structure and magnetic properties RE-Fe_2 metal compounds have been intensively studied during the past 40 years [9, 22, 23].

The indirect spin interaction between the *4f* electrons of RE and the *3d* electrons of Fe via the spins of *5d* electrons in the RE-Fe_2 compounds are crucial to determine the mechanism of magnetostriction, after F. R. de Boer [24].

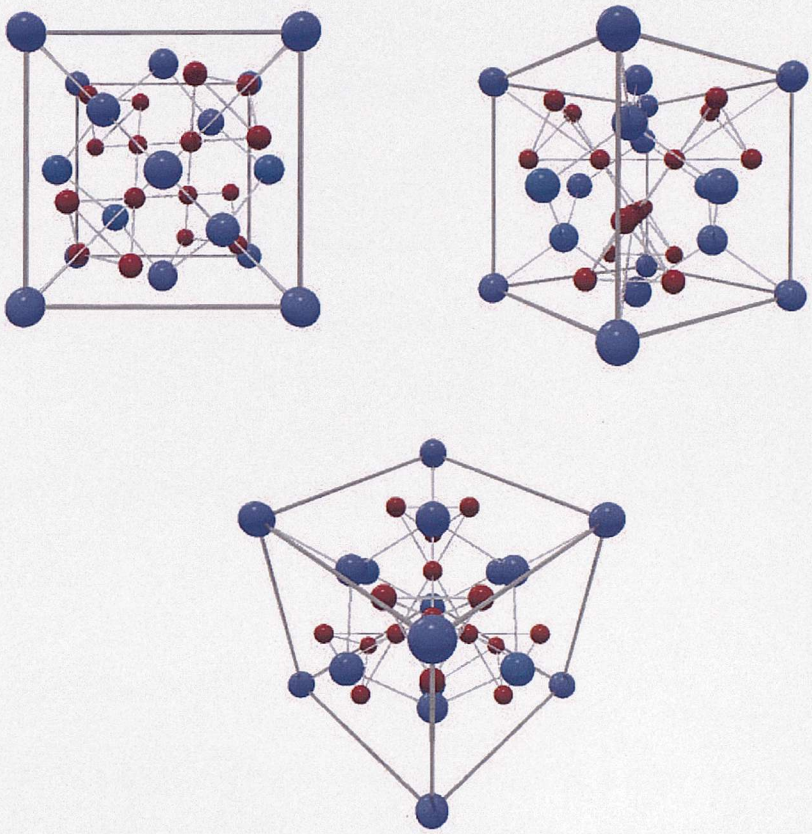

Figure 2.5 Atomic positions in the C-15 $MgCu_2$ cubic Laves phase unit cell. Iron sublattice forms a network of connected tetrahedral.

RFe_2 compounds crystallize in the cubic $MgCu_2$ – type of Laves phase structure (C-15, space group Fd3m). The local symmetry for the RE ions is cubic and trigonal for the Fe ions. The $MgCu_2$ unit cell contains eight formula units. Each RE ion has 12 Fe nearest neighbours, at a distance of $\frac{1}{8}\sqrt{11}\,a$ and 4 RE ions at a distance of $\frac{1}{4}\sqrt{3}\,a$ as nearest-neighbour shell with a radius of $\frac{1}{4}\sqrt{2}\,a$ and 6 RE ions at $\frac{1}{8}\sqrt{11}\,a$ as nearest neighbours (Fig. 2.5).

In RE-Fe_2 materials, it is generally accepted that there are three types of exchange interactions:

- the strong Fe-Fe interaction between the magnetic moments of the Fe sublattice which gives rise to a high Curie Temperature T_C

- the rather weak RE-RE interaction between the magnetic moments within the RE sublattice.
- the relatively strong RE-Fe intersublattice interactions which gives rise to FM (AFM) coupling in the heavy (light) RE compounds respectively.

2.4.1 The Fe-Fe exchange interaction

The Fe-Fe interaction between 3*d* magnetic moments is strong and long range. The wavefunctions of neighbouring Fe atoms overlap producing 3*d* electron energy bands. The Fe-Fe interaction is positive leading to FM coupling between the 3*d* moments. This interaction primarily governs the temperature dependence of the TM magnetisation.

2.4.2 The RE-RE exchange interaction

In the Laves phase compounds, the RE-RE interaction is generally the weakest. Indeed, the spatial extent of the 4*f* wavefunction is highly localised since the 4*f* shell lies deep within the ions. In the trivalent state, for example Dy^{3+}, two of the 6*s* electrons and one of the 4*f* electrons are removed but the outer 5*s* and 5*p* shells remain intact. Consequently, the remaining 4*f* electrons are partially shielded from perturbation from external fields. Thus, direct exchange between the RE atoms is rather weak.

Zener [25] has suggested that localised moments could be coupled together by an indirect exchange through the medium of the conduction electrons. In a metal containing RE ions, it is generally considered that the RE-RE interactions take place by indirect exchange (RKKY-type), mediated by the 5*d*-like conduction electrons [26]. The mechanism involves the polarisation of the 5*d* electrons by the 4*f* spins. These 5*d*-like conduction electrons subsequently interact with 5*d* electrons of the neighbouring ions. In such a picture, the effective parameter of the 4*f*-4*f* spin coupling $J_{RE\text{-}RE}$ contains information about the more fundamental interaction parameters $J_{4f\text{-}5d}$ and $J_{5d\text{-}5d}$.

2.4.3 The RE-Fe exchange interaction

The RE-Fe exchange interaction takes place between all unpaired spins in the 3*d*-4*f* system via the spins of 5*d* electrons. The interaction parameter $J_{RE\text{-}Fe}$ is responsible for the internal magnetic structure. For heavy RE's, its negative sign gives rise to antiparallel coupling of the RE and Fe moments. Whereas in the light RE, the RE and Fe moments are coupled antiferromagnetically.

The strength of the RE-Fe exchange interaction can be determined experimentally by several methods. This constant can be obtained from analysis of the ordering temperature [27], of the high field magnetisation measured on free powders [28], and from the inelastic neutron scattering spectra using a well established spin wave model [29].

References

[1] F. H. Spedding, S. Legvold, A. H. Daane, and J. D. Iennings, *Progess in Low Temperature Physics* (*Ed.* C. J. Gorten), North-Holland, Vol. **II**, p.368 (1957)

[2] James William Rohlf, *Modern Physics from A to Z*, Wiley (1994)

[3] E. C. Stoner, *Proc. Roy. Soc. London A* **165**: 372 (1938)
E. P. Wohlfarth, *Philos. Mag.* **42**: 374 (1951)

[4] H. Ibach and H. Lüth, *Solid State Physics*, Springer-Verlag (1990)

[5] More sophisticated

[6] N. W. Ashcroft and N. D. Mermin, *Solid State Physics*, Holt Saunders, Japan, (1981)

[7] H. Skriver, *Systematics and Properties of the Lanthanides* (*Ed.* S. P. Sinha), Reidel Dordrecht, pp. 213-254 (1983)

[8] J. Jensen and A. R. Mackintosh, *Rare Earth Magnetism: Structures and Excitations*, Oxford University Press, Oxford (1991)

[9] K. H. J. Buschow, *Rep. Prog. Phys.* **40**: 1179-1256 (1977)

[10] S. Chikazumi and S. H. Charap, *Physics of Magnetism*, Krieger Publishing Company, Malabar Florida (1978)

[11] A. H. Morrish, *The Physical Principle of Magnetism*, Wiley New York (1965)

[12] R. L. Comstock, *Introduction to Magnetism and Magnetic Recording*, (*ed.* Wiley - Interscience), p.180 (1999)

[13] K. W. H. Stevens, *Proc. Phys. Soc. A* **65**: 209 (1952)

[14] B. Bleaney, *Proc. Roy. Soc. A* **276**: 39 (1963)

[15] E. R. Callen and H. B. Callen, *Phys. Rev.* **139**: A455 (1965)

[16] G. J. Bowden, *Dip. Adv. Stud. Sci.*, **vol. 1**, (1990)

[17] C. Kittel, *Rev. Mod. Phys.* **21**: 541 (1949)

[18] Jan Smit, *Magnetic properties of materials*, Inter-University electronics series vol. **13**, (*ed.* MacGraw Hill), p. 14, (1971)

[19] E. Lee, *Magnetostriction and Magneto-mechanical effects*, Rept Prog. Phys. **18**: 184-229 (1955)

[20] W. Klemm and H. Bommer, *Z. Anorg. U. Allgem. Chem.* **231**: 138 (1937)

[21] D. Craik, *Magnetism: Principles and Applications* (*Ed.* Wiley and Son), New York, p.404 (1995)

[22] G. J. Bowden *et al.*, *J. Phys. C* **1**: 1376 (1968)

[23] J. H. Wernick and S. Geller, *Trans. Am. Inst. Min. Metall. Petrol. Engrs* **218**: 866 (1960)

R. L. Cohen et al., *Phys. Rev.* **134**: A94 (1964)
E. Burzo *et al.*, *Solid State Communications* **14**: 1295 (1974)
J. S. Jaswal *et al.*, *Phys. Rev. B* **41**: 9697 (1990)
J. S. Jaswal *et al.*, *Phys. Rev. Lett.* **67**: 644 (1991)
J. S. Jaswal *et al.*, *Phys. Rev. B* **48**: 6156 (1994)
J. Farrell and W. E. Wallace, *J. Chem. Phys.* **41**: 1524
M. Mansmann and W. E. Wallace, *J. Chem. Phys.* **40**: 1167

[24] F. R. de Boer and K. H. J. Buschow, *J. Alloys Compounds* **158**: 1 (1997)

[25] C. Zener, *Phys. Rev.* **81**: 440 (1951)

[26] P. G. de Gennes, *J. Phys. Radiat.* **23**: 510 (1962)
J. A. Campbell, *J. Phys. F* **2**: L47 (1972)

[27] E. Belorizky *et al.*, *J. Appl. Phys.* **61**: 3971 (1987)
N. H. Duc *et al.*, *Phys. Stat. Solid. B* **164**: 545 (1991)
N. H. Duc *et al.*, *J. Magn. Magn. Mater.* **124**: 305 (1993)

[28] R. Verhoef *et al.*, *J. Magn. Magn. Mater.* 83: 139 (1990)
F. R. de Boer and K. H. J. Buschow, *Physica B* **177**: 199 (1992)

[29] R. M. Nicklow *et al.*, *Phys. Rev. Lett.* **36**: 532 (1976)
N.C. Koon and J. J. Rhyne, *Solid. State Commun.* **26**: 537 (1978)
J. J. Rhyne *et al.*, *J. Magn. Magn. Mater.* **14**: 273 (1979)

Chapter 3

Growth of single crystal Laves phase superlattices

The study of bulk material raises the question whether the variety of results is related to the formation of domains or grains in the ferromagnet, to the sensitivity on material parameters, to interface composition and roughness etc... To separate such disorder related effects from the properties of an ideal sample, it is important to study the properties of an ideal alloyed or layered system.

Sputtering (DC or RF) and Molecular Beam Epitaxy (MBE) are generally used to fabricate metallic superlattices while ion beam sputtering [1] and pulsed laser deposition [2] are used less frequently. MBE is an inherently clean process as it uses Ultra-High Vaccuum (UHV) technology. With this technique, it is possible to design and grow samples of any element or alloy in sequence with different layer thicknesses and atomically flat interfaces to enable experimentalists to test directly the theoretical predictions. It also allows the synthesization of peculiar heterophase magnetic materials, with unique physical properties and important practical applications [3].

The magnetic properties of bulk Laves phase intermetallic compounds have attracted much attention since they were originally synthesized by Wernick and Geller in the early 1960's [4]. And, the recent realisation of epitaxial films of these materials [5, 6] has opened up new opportunities to control their properties through epitaxial strain. In this chapter, the MBE growth of C-15 Laves phase-based system is discussed, including a brief history of the MBE technique itself.

3.1 Molecular beam epitaxy

3.1.1 Historical introduction

The technique of MBE was introduced in 1968 for the growth of thin films of III-V compound semiconductors. It combined, for the first time, precise control of film thickness and composition profiles, with the ability to study film growth in real time using a variety of *in-situ* electron beam probes. In fact, the UHV system is the key advantage of the technique because it minimises incorporation of impurities into the film from background species.

Initially, high-purity epitaxial layers of GaAs and $Al_xGa_{(1-x)}As$ [7] were produced, which had a profound influence on semiconductor physics [8]. It lead to the discovery of the two-dimensional electron gas and the band gap engineering of semiconductor heterostructures.

In the late 1970's, MBE was applied to metal epitaxy, magnetic metal epitaxy. The first metals, grown with high quality by MBE were body-centered cubic (bcc) Nb and Ta [9]. Face-centered cubic (fcc) Ir and hexagonal-close packed (hcp) Ru [10], were also grown by MBE as epitaxial crystals of high quality, as well as other bcc metals such as Cr [11]. The driving force for this new research direction was the expectation that, by analogy with semiconductor film growth, MBE could provide high-perfection, epitaxial, magnetic metallic structures with novel magnetic properties. This expectation was in fact realised by several discoveries in the late 1980's, including that of GMR [12]. It is worth noting that in the 1980's, the growth chamber was not pumped to a UHV background, precluding effective substrate cleaning prior to film growth. In addition, impurities in the sputtering gas and targets were incorporated into the films. Thus, high perfection epitaxial metal films were not obtained until the late 1980's, when UHV design features previously found only in MBE systems were incorporated.

Since the first MBE growth of lattice mismatched metallic superlattices from the Nb-Cu [13], many more systems have been fabricated. In 1986, the first high-perfection MBE epitaxial magnetic superlattices of Gd/Dy and Dy/Y were

prepared [14]. These Rare-Earth (RE) superlattices provided an elegant demonstration of indirect exchange coupling of Gd (Dy) through the non-magnetic Y layers via the RKKY interaction. This led to interest in magnetic superlattices and sandwiches incorporating 3*d* transition metals with the prospect of room temperature applications.

The recent interest in the epitaxially grown RE Laves phase-based structures have been stimulated by the demonstration by Ref. [5, 6, 15] that the (110) Nb on $(11\bar{2}0)$ sapphire substrate template enables the growth of high quality single-crystal Laves phase intermetallic layered systems. The MBE technique based on the Al_2O_3/Nb template system is responsible for the growth of almost all the epitaxial Laves phase-based structures reported to date.

3.1.2 The principle of the MBE technique

Crystal growth by Molecular Beam Epitaxy is usually described by the deposition of atomic elements onto a substrate at an elevated temperature. The MBE technique allows smooth epitaxial layers to be produced, with atomically flat interfaces, and good control of thickness and composition. Indeed, the low growth rates, typically of the order of a few Å/s, combined with the possibility to shutter the beams in a fraction of a second, allows for layer-by-layer growth and nearly atomically abrupt transitions from one material to another. To obtain high purity layers, it is critical that the material sources be extremely pure and that the process is carried out in an ultra-clean environment to minimise the inclusion of impurities into the film. In MBE, the substrate is maintained in UHV during its *in-situ* preparation prior to epitaxy and during the growth process. The background pressure in the growth chamber is typically of 4×10^{-8} mbar.

For relatively thick individual layers, detailed knowledge of the interface structure is not important because the physical properties of the multilayers are not significantly affected by the interface quality. On the other hand, for multilayers with single layers thickness of several ten of angstrom, structural characterisation is crucial. UHV MBE technique allows *in-situ* surface characterisation by sensitive diagnostic tools such as Reflection High Energy Electron Diffraction (RHEED) and Auger Electron

Spectroscopy (AES). By contrast, in sputtering rigs the substrate and targets are immersed in a gas (typically Argon) at a pressure of a few mB. The presence of sputtering gas generally excludes the use of *in-situ* structural characterisation techniques.

RHEED allows the real-time monitoring of surface lattice parameter and diffracted intensity profiles. Electrons reflect from the surface and strike a phosphor screen forming a pattern consisting of a specular reflection and a diffraction pattern which is indicative of the surface crystallography. If the surface is smooth, the RHEED diffraction patterns appear streaky. If the samples are rough, then the streaks are more 'spotty' and the diffraction pattern is not as clear. An amorphous surface, shows a haze instead of a diffraction pattern and polycrystalline surfaces result in rings circling the straight-through beam. RHEED can also be used to calibrate growth rates.

Finally, non-destructive diffraction techniques, such as X-Ray diffraction (XRD), are commonly used to analyze multilayered structure [13].

When the magnetic materials are grown on chemically different substrates, elastic fields arise that change the surface diffusion of atoms. Diffusion can be slowed down or enhanced, depending on the sign of the strain. Understanding diffusion and growth on strained layers opens up new possibilities in growth kinetics/morphologies.

3.2 MBE growth of Laves phase based structures

3.2.1 The MBE instrument

All the samples studied in this thesis, have been prepared using MBE technique [2]. The metals MBE facility is a *Balzers UMS* 630 system. It consists of 2 main vacuum chambers: the growth chamber, and the sample introduction (loadlock) chamber, as shown in Fig. 3.1.

[2] The samples were grown by Dr. R. C. C. Ward and Dr. M. R. Wells, from the Oxford MBE Laboratory, at Oxford University.

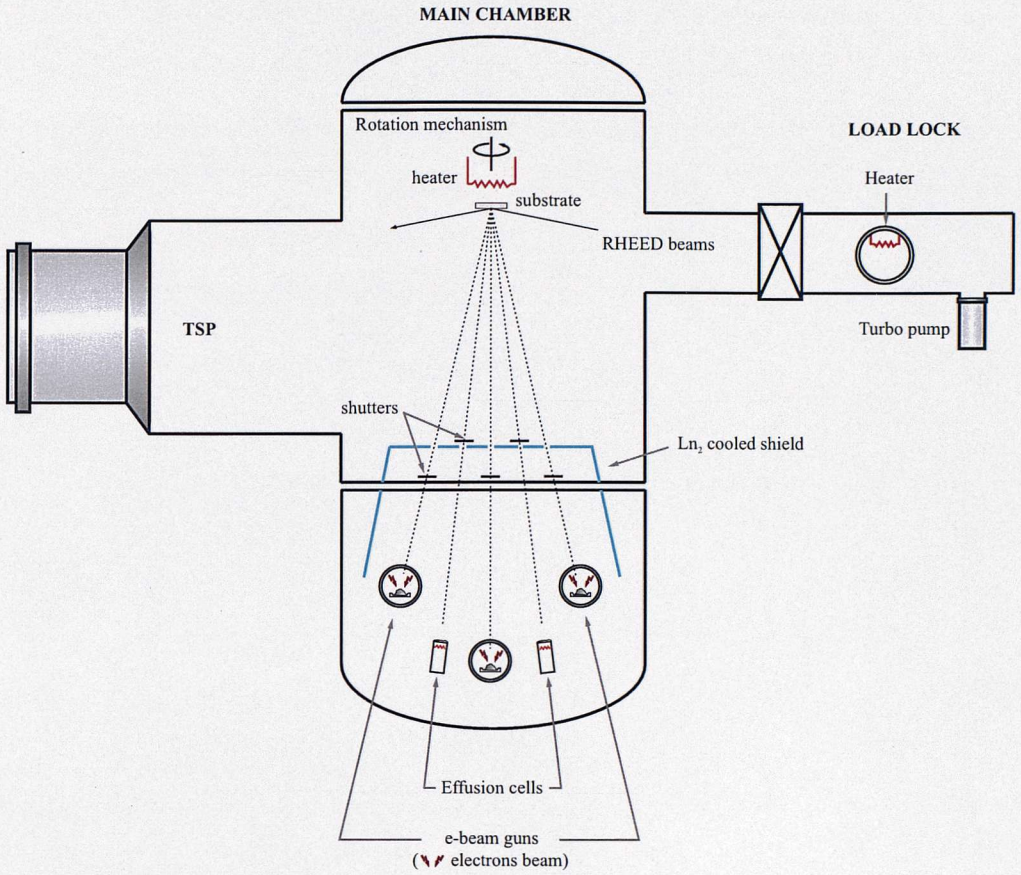

Figure 3.1 Diagram of the MBE growth chamber.

The loadlock is used to bring the samples into and out of the vacuum environment while maintaining the vacuum integrity of the other chamber. The growth chamber is pumped by a turbo-molecular pump and a Titanium Sublimation Pump (TSP). Additional trapping of impurities is provided by a liquid nitrogen cryoshield that surrounds the sources. The MBE system is configured with a total of five independently heated evaporation sources: two effusion cells and three electrons beam (e-beam) guns. The effusion cells are heated by radiation from a resistance-heated filament. They are suitable for evaporating metals with a relatively high vapour pressure at temperature below 1300°C to yield a growth rate of 0.1 nm/s. For materials that require evaporation temperature in excess of 1300°C, it is more practical to bombard the source directly with a high energy e-beam.

A combined linear shutter/quartz crystal monitor facility allows the flux monitor to be moved into the substrate position for accurate flux calibration. The substrate temperature is controllable between room temperature and 1000°C. Full computer control is available for all source control operations and depositions sequences as well as vacuum control. The system is also equipped of *in-situ* monitoring and characterisation tools. A quadrupole mass spectrometer analyses the residual gas components and a RHEED facility provides real-time characterisation of the growth interface.

3.2.2 The growth of epitaxial RE-Fe_2 structures

An epi-prepared $(11\bar{2}0)$ sapphire substrate (10×12 mm) with high crystallographic quality, is outgassed at 800°C for several hours. A clean surface is an important pre-requisite for epitaxial growth, since impurities can easily contaminate the substrate and cause crystal defects. Subsequently, a buffer layer of the bcc refractory metal (110) Nb is deposited by MBE onto the heated substrate. No reaction products form at the Al_2O_3-Nb interface.

The rate of the Nb deposition is at 0.5 Å/sec with the background pressure at 4×10^{-8} mbar. Initially, a Nb layer thickness of 500 Å was used. But lately, it was found that the thickness of the buffer layer could be reduced down to 75 Å, without detrimental effects on the growth of the Laves phase. The temperature of the Nb layer during growth is an important parameter. Indeed, in Ref. [16] it was shown that the morphology of the Nb buffer layer is temperature dependent. It is required that the Nb surface be as near as possible atomically smooth.

RHEED pattern analysis shows that Nb grows as a single crystal with (110) plane parallel to the plane of the substrate (Fig. 3.2). The epitaxial relationships are as follow $[11\bar{1}]$ Nb $\|$ [0001] Al_2O_3, and $[11\bar{2}]$ Nb $\|$ $[10\bar{1}0]$ Al_2O_3.
In addition to providing strain relief from the lattice mismatch between the RE-Fe_2 film and the substrate, the Nb layer is also used as a chemical barrier to prevent interdiffusion between the highly reactive RE metals and the substrate.

In order to relax the misfit strain between the cubic Laves phase RE-Fe_2 and the bcc Nb, a Fe seed layer of 15 Å or 30 Å is deposited at 500°C. Actually, the thin Fe layer and the Nb layer react with one another to produce a Nb-Fe alloy on the surface [5]. RHEED surface analysis show that at 500°C (100) bcc Fe grows epitaxially on (110) bcc Nb despite the large mismatch between the parameters (15%). Also, it is observed a 2-D rectangular lattice where the lattice parameters are close to those of a C-15 cubic Laves phase in (110) plane [17].

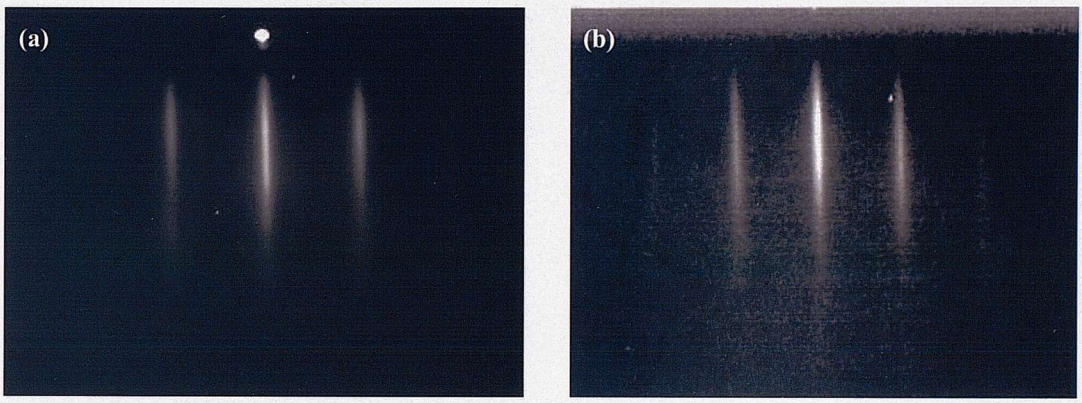

Figure 3.2 RHEED diffraction patterns (after E. Grier [17]):
a) from 100 Å Niobium buffer (110) **b)** from Laves phase superlattice (110).
The streaky appearance of the diffraction patterns for both the materials confirms their single crystalline nature and a smooth surface.

Finally, the Laves phase-based film is deposited at a rate of 5-10 Å/min, by co-deposition of the RE and Fe constituents. Depending on the substrate temperature, dots with anisotropic shape or continuous films with low surface roughness are obtained. It was found that the best conditions for a good epitaxy require a growth temperature near 750°C. For multilayers systems, the temperature is reduced to 620°C for the deposition of the second layer component to avoid interdiffusion, because the RE have a high tendancy to intermix. At this level, the epitaxial relationships are: [1 $\bar{1}$ 0] RE-Fe_2 || [1 $\bar{1}$ 0] Nb, and [001] RE-Fe_2 || [001] Nb. [3, 5]
In Fig. 3.3, a photography of the cross section of a typical multilayer sample can be seen.

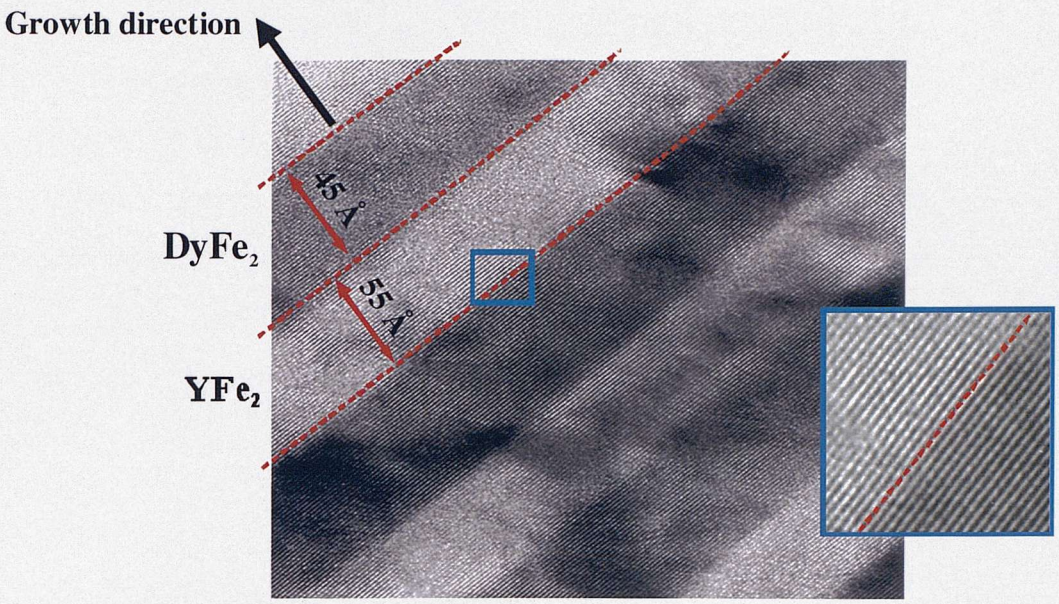

Figure 3.3 Photography of a typical multilayer sample. (after E. Grier [17])
Bright-field cross-sectional Transmission Electrons Microscopy (TEM) image of the superlattice [45 Å $DyFe_2$ / 55 Å YFe_2] × 40.
The darker (lighter) part of the picture corresponds to the $DyFe_2$ (YFe_2) layers. The enlargement enables to see the atomic layers.

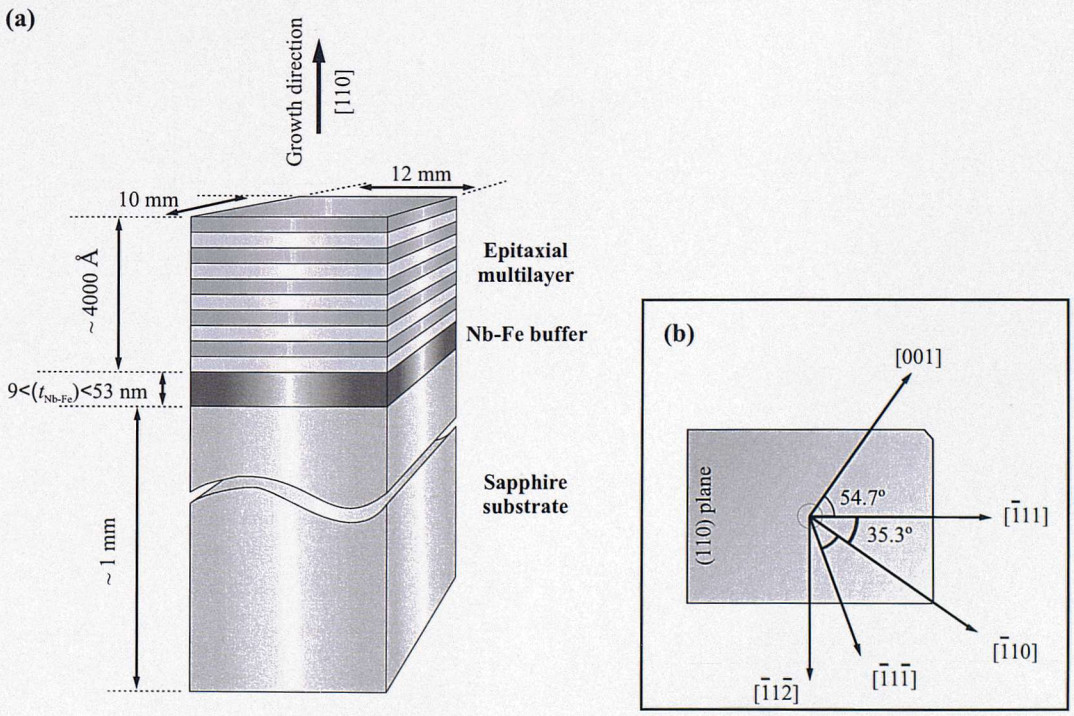

Figure 3.4
c) Typical superlattice film.
d) Crystallographic orientations within the (110) plane.

In Fig. 3.4, it is shown a schematic representation of the RE-Fe_2 multilayer samples. Also included are the in-plane crystallographic directions (Fig. 3.4.b).

In-situ RHEED analysis shows that during the first stage of growth, the patterns are diffuse, with spotty patterns evidencing a large roughness. But with increasing thickness, the RHEED patterns gradually transform into well defined and high quality streaks, a classic signature of decreasing surface roughness.

A small average interface roughness (less than ~10 Å) of the layers was determined from high resolution transmission electron measurements [17]. The composition of the bilayers was checked by microprobe analysis. The stoichiometric composition was found to be within ±2% for RE-Fe_2. The thickness was estimated by the calibration of the evaporation rates, using quartz balances and optical sensors with a 10% error.

A dedicated e*x-situ* X-Ray diffraction facility was used for rapid analysis of the samples grown. X-Ray diffraction analysis at room temperature, confirmed the epitaxial nature of the films and the growth direction [110]. This technique was also used to check the bilayer repeat distance, and to determine the RE-Fe_2 lattice parameters.

Finally, it was found that the samples exhibit an average ~0.6% lattice expansion in the film plane and a ~-0.4% contraction along the [110] growth direction [18]. The cause of the tensile strain is related to the difference in the thermal expansion coefficients of sapphire and RE-Fe_2 since the lattice misfit strain in layered and alloyed systems can be assumed to be compensated by dislocation deformation in the early stages of the film growth. Note that Nb and Al_2O_3 possess similar thermal expansion coefficients. In Ref. [6] it was shown that depending on the substrate temperature during growth, varying degrees of residual tensile strain were induced in the RE-Fe_2 films.

3.3 Conclusions

The MBE technique, with its high degree of control, allows the production of synthesized thin films with well defined geometry. Using MBE epitaxy, it is possible to grow single crystal Laves phase layered and alloyed thin films, with the growth direction along [110], and the crystallographic axis [001] in the plane of the film. Moreover, it is possible to use differing refractory templates (Nb, Mo, W) to obtain (110) or (111) growth at choice [5, 6, 15, 19].

Usually, magnetic thin films undergo stress when they are grown onto a substrate. The most probable origin of the epitaxial strain is the thermal stress which appears at the end of the growth when the substrate is cooled down to room temperature. Indeed, the thermal expansion coefficients of sapphire and metallic film are very different. The RE-Fe_2 films are left expanded in-plane and consequently compressed perpendicular to the plane. Thus, the lattice parameters of the RE-Fe_2 differ by ~1% across the RE-Fe_2-based samples in comparison with their bulk parameters. A typical strain within the superlattice system was estimated to be of the order of 0.5%. Those structural deformations of the lattice cause dramatic changes to the magnetic phase diagram of the RE-Fe_2 superlattices. Consequently, the strain and/or clamping introduced by epitaxy provide new control parameters that can be used to modify magnetic phase diagrams [20].

References

[1] A. Chaiken *et al.*, *Phys. Rev. B* **53**: 5518 (1996)

[2] D. B. Chrisey, Pulsed Laser Deposition of Thin Films, (*Eds.* G. K. Hubler), Wiley, New York (1994)

[3] J. Nogues, I. K. Schuller, *J. Magn. Magn. Mater.* **192**: 203 (1999)
R. L. Stamps, *J. Phys. D* **33**: R247 (2000)

[4] J.H. Wernick, and S. Geller, *Trans. Am. Inst. Metall. Pet. Eng.* **218**: 866 (1960)

[5] V. Oderno *et al.*, *J. Cryst. Growth* **165**: 175 (1996)

[6] M. Huth, and C. P. Flynn, *J. Appl. Phys.* **83**: 7261 (1998)

[7] A. Cho, Film Deposition by Molecular Beam Techniques, J. Vac. Sci. Tech., Vol. 8, pp.S31-S38 (1971)
A. Cho, J. Arthur, 'Molecular Beam Epitaxy', Prog. Solid-State Chem., Vol. 10, pp.157-192 (1975)

[8] D. C. Tsui *et al.*, *Phys. Rev. Lett.* **48**: 1559 (1982)

[9] S. M. Durbin *et al.*, *J. Phys. F* **11**: L223 (1981) / S. M. Durbin *et al.*, *J. Phys. F* **12**: L75 (1982)

[10] J. E. Cunningham and C. P. Flynn, *J. Phys. F* **15**: L221 (1985)

[11] P. Grunberg *et al.*, *Phys. Rev. Lett.* **57**: 2442 (1986) / P. Sonntag *et al.*, *Phys. Rev. B* **49**: 2869 (1994)

[12] M. N. Baibich *et al.*, *Phys. Rev. Lett.* **61**: 2472-2475 (1998)

[13] I. K. Schuller, *Phys. Rev. Lett.* **44**: 1597 (1980)

[14] J. Kwo *et al.*, *Phys. Rev. B* **35**: 7295 (1987) / C. F. Majkrzak *et al.*, *Phys. Rev. Lett.* **56**: 2700 (1986) / R. W. Erwin *et al.*, *Phys. Rev. B* **35**: 6808 (1987)

[15] C. T. Wang *et al.*, *I.E.E.E Trans. Magn.* **32**: 4752 (1996)

[16] G. L. Zhou and C. P. Flynn, *Phys. Rev. B* **59**: 7860 (1999)

[17] E. Grier, Thesis, Oxford University, UK (2000)

[18] Mougin, *Phys. Rev. B* **62**: 9517 (2000)

[19] C. T. Wang, R. M. Osgood III, R. L. White, and B. M. Clemens, *Magnetic Ultrathin Films, Multilayers, and Surfaces, edited* by A. Fert, H. Fujimori, G. Guntherodt, B. Heinrich, W. F. Egelhoff Jr, and E. E. Marinero, MRS Symposia Proceedings, Vol. 384 (Materials Research Society, Pittsburgh, 1995)
V. Oderno *et al.*, *Europhys. Lett.* **36**: 713 (1996) / V. Oderno *et al.*, *Phys. Rev. B* **54**: R17 375 (1996) / S. Jaren *et al.*, *J. Magn. Magn. Mater.* **165**: 172 (1997)

[20]C. P. Flynn and M. B. Salamon, *Handbook on the Physics and Chemistry of Rare Earths, edited* by K.A. Gschneidner and L. Eyring, p.1 (Elsevier, Amsterdam, 1996)

Chapter 4

Experimental methods

The usual approach to characterise a magnetic compound consists in measuring its hysteresis loop. This provides decisive information about the magnetic nature of the material: the magnetisation of saturation M_{sat}, *the remanent magnetisation* M_{rem}, *and the coercive field* B_C. *The Vibrating Sample Magnetometer (VSM) is ideally suited to determine the macroscopic magnetic properties of materials and it is widely regarded as the de facto standard of the magnetic measurement. All the magnetometry data obtained in this thesis were recorded using a commercial uni-axial VSM (at Southampton) and a Vector-VSM (at QinetiQ*[3]*).*

In this chapter, the functionality and performance of the VSM and vector VSM are reviewed and discussed. In addition, details are given of sample preparation and data interpretation is outlined.

[3] *QinetiQ* (formely *D.E.R.A*), Cody Technology Park, Farnborough, Hampshire, UK

4.1 The Vibrating Sample Magnetometer

The first uni-axial Vibrating Sample Magnetometer (VSM) was developed in 1956 by Foner and Van Oosterhart [1]. Since then, it has been accepted as the standard magnetic measurement method [2, 3]. In this section, the physical principles of the VSM are discussed, because a clear insight into its functioning is vital to the interpretation of the results.

The VSM method or 'induction method' is primarily based on Faraday's law: an *emf* ε is induced in a circuit when the magnetic flux ϕ through that circuit changes from any cause [4]:

$$\varepsilon = -\frac{d\phi}{dt} \tag{4.01}$$

In Fig. 4.1.a, an idealized configuration of the VSM can be seen. The sample, usually a sphere or a small disk is mounted on a vertical rod, and it is suspended in a region of homogeneous magnetic field, in the centre of a symmetrical array of sense coils. A vibration transducer moves the sample sinusoidally along the magnet symmetry axis, in a controlled manner. For commercial VSM's, the frequency and the amplitude of the sinusoidal motion is typically set at 66.6 Hz and 1.5 mm respectively. To simplify the analysis, it is assumed that the specimen is homogeneously magnetized and small enough to be considered as a magnetic dipole. The instantaneous voltage generated across the pick-up coils by the magnetized specimen can be calculated by applying Mallinson's principle of reciprocity [5]. This principle enables the application of the Biot-Savart law to a dipole field, hence the flux induced by the magnetic dipole $\vec{m}$ in the pick-up coils is:

$$\phi = \frac{\vec{m} \bullet \vec{B}}{I} \tag{4.02}$$

where $\vec{B}$ is the vector magnetic field which would be produced by a fictitious current I circulating in the pick-up coils.

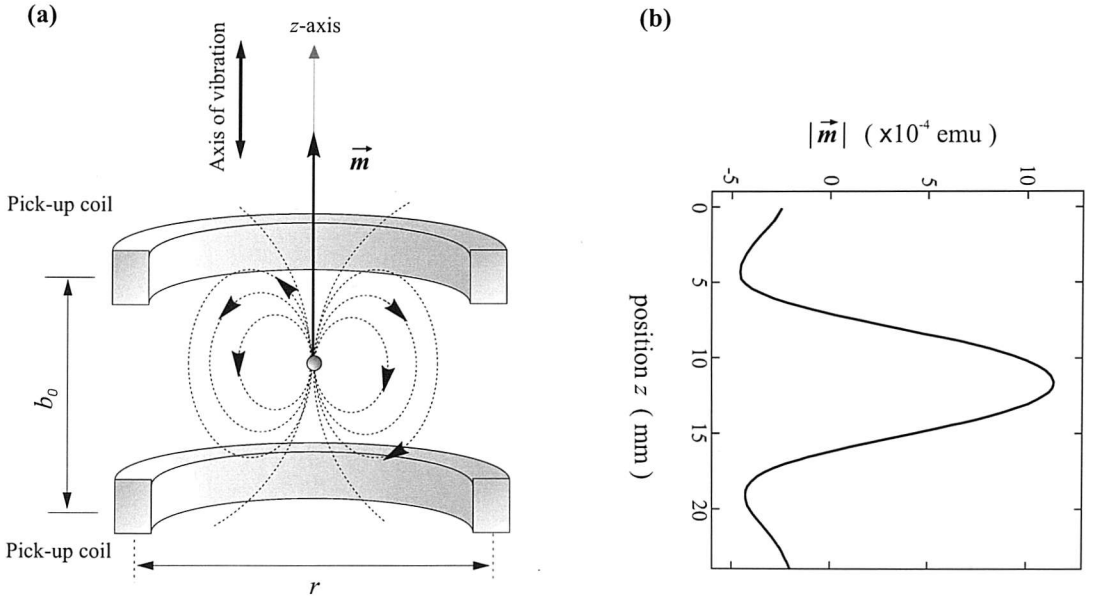

Figure 4.1
a) A schematic set up of the vibrating sample magnetometer.
The field lines of the magnetic sample enter the cross section area of both the pick-up coils, generating a changing magnetic flux.The size of the magnetized specimen is much smaller than the pick up coils dimensions: b_0 and r.
b) The sensitivity function for a 4000 Å $DyFe_2$ epitaxial film.
The vibrating specimen is magnetized by a uniform vertical magnetic field of 0.5 T. It is moved vertically along the z-axis over a distance of 25 mm.

The analysis is simplified by assuming that the magnetic moment $\vec{m}$ is pointing in the z-direction:

$$\varepsilon = -m \frac{d\left(B/I\right)}{dz} \times \frac{dz}{dt} \tag{4.04}$$

By considering that the sample oscillates at a frequency $f = 2\pi/\omega$, about the point z_0 and with a small amplitude z_a, its position is determined by:

$$z(t) = z_0 + z_a \cos \omega t \tag{4.05}$$

Then, Eq. 4.04 can be re-written:

$$\varepsilon = z_a \omega m \sin \omega t \; G(z_0) \tag{4.06}$$

where $G(z_0) = \left.\frac{d(B/I)}{dz}\right|_{z_0}$ is the so-called sensitivity function that represents the dependence of the VSM output on the position of the sample along the z-axis (Fig. 4.1.b). And $z_a\omega$ is the speed amplitude of the sample.

As it appears from Eq. 4.06, $G(z_0)$ must be a constant over all the sample volume. To establish the direct relationship between induced voltage and magnetic moment, the constant parameter $G(z_0)$ needs to be determined. The usual approach consists in using a calibrant, whose magnetisation of saturation is well known. This calibrant must also have the same geometry (size and shape) and preferably a larger magnetisation of saturation than the sample under investigation. Popular calibrants for VSM's include *Nickel*, *Platinum* and *Palladium* as they can be obtained in high purity.

In the analytical calculations discussed above, an ideal system is considered. However, in a real measuring device, the VSM is subject to background noises due to magnetic field instability, mechanical coupling between the vibrator and the detection coils, etc..., which can have dramatic effects on the precision of the measurements of the sample magnetic moment. One of the methods used to eliminate the influence of the background noise consists in winding the two sensor coils in opposite sense. Therefore, if the pick-up coils are properly matched and, if the magnetic field is uniform over their entire volume, the signal from the sample is doubled, whilst the background noise is reduced considerably. This configuration is known as the *Williams-Comstock* construction [10].

As mentioned earlier, the response of the pick-up coils is described by the sensitivity function $G(z)$, whose the generalized form may be written $G(x,y,z)$, where x, y, and z are the coordinates of the sample position. Broadly speaking, a good measuring device must minimize $G(x)$ and $G(y)$. Therefore, lateral vibration of the sample must be avoided by using a rigid sample rod. Also, the samples must be sufficiently small in x-y dimensions compared with the internal dimensions of the coils.

In a commercial magnetometer, the applied magnetic field is supplied by an electromagnet or high field superconducting magnet. The magnetic field generated must be homogeneous, not only over the sample, but over the entire volume of the

pick-up coils. Indeed, in the *Williams-Comstock* configuration, the signal produced in one coil by the varying applied field is cancelled by the signal induced by the same field in the 2nd coil.

In recent years, one of the major technical improvements on the VSM has been the rotating insert. For this type of magnetometer, known as a Vector-VSM (VVSM), the vibration transducer assembly is mounted on a rotational drive, which can provide up to 370° of sample rotation. So, it is possible to accurately rotate the sample with respect to the z-axis, and to record the angular dependence of the magnetisation. The conventional configuration for the VVSM allows rotation of the specimen, in a fixed magnetic field. However, other commercial VVSM's allow the rotation of the applied magnetic field rotation in place of sample rotation. By using a double set of pick-up coils at right angles to each other, the magnetisation vectors in the horizontal plane can be recorded simultaneously, and resolved into components $m_{\parallel}$ (component parallel to the applied field) and $m_{\perp}$ (component perpendicular to the applied field) (Fig. 4.2). This information can then be used to calculate the anisotropy energy as a function of angle θ [8]. Note also that it is also possible to install a 3rd set of sensitive coils to measure the component m_z [9].

In a VVSM, the rotation asymmetries and eccentric rotations play a major role in determining the inaccuracies of the measurements. When a sample is rotated, it never rotates around the exact center of the sample. This is known as *eccentric rotation.* Thus, the position of the sample changes as a function of rotation angle. Since the sensitivity of VSM sense coils is a very strong function of the sample position, this change in position during rotation will show up as an angle dependent error.

Another issue is that of the *image effect.* When the pick-up coils are mounted close to the pole faces, the sensitivity of the coils changes at high fields as a result of the image effect. So the sensitivity of the VVSM becomes a function of both the field and the rotation angle induced in the magnetic pole pieces.

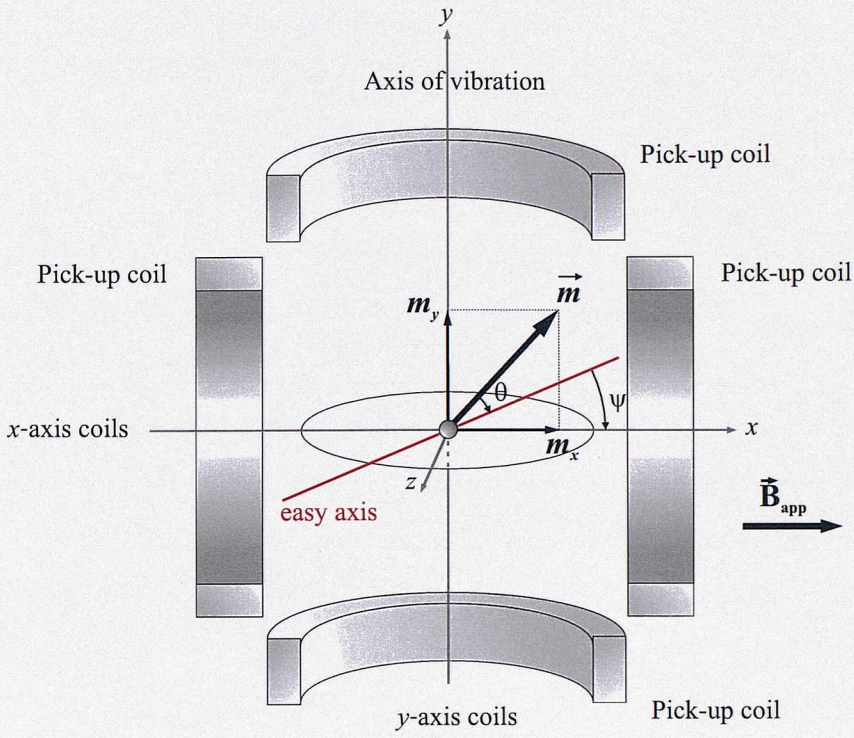

Figure 4.2 Sketch of a bi-axial vector VSM. The magnet produces a magnetic field directed along the x-axis. One pair of sensing coils are parallel to the applied field and sense the magnetisation component longitudinal to the field $m_{\parallel} = m_x$. A 2nd set of coils is mounted at right angles to the applied field and senses the magnetisation component transverse to the field is $m_{\perp} = m_y$.

4.2 Preparation of the samples

The VSM used in this work to characterize the epitaxial magnetic Laves phase materials was a computer-controlled measurement system: *Oxford Instruments* Aerosonics 3001 VSM. This magnetometer is a completely axial instrument: a *dc* magnetic field is applied axially in the vertical direction and the magnetic moment of the sample parallel to the field ($m_{\parallel}$) is measured. Its sensitivity is ~ 2×10^{-6} emu. The VSM is equipped of a superconducting magnet, which has homogeneity of 0.1 % over a 10 mm diameter sphere. It provides a magnetic field up to 12 T.

All the magnetic measurements reported in this thesis were performed at magnetic field sweep rate of 1200 mT/min. The magnetic field is probed by a Hall effect sensor with an accuracy of ~ 1 %. A cryostat allows temperature dependence measurements in the temperature range from 300 K down to 5 K. [10]

The magnetometer used to characterize the angular dependence of the magnetic properties of the TbDyFe-series films is a uni-directional VVSM. A single set of pick-up coils, are arranged in the Williams-Comstock configuration, with their symmetry axis along the applied magnetic field. Therefore, only the component $m_{\parallel}$ of the magnetic moment (component parallel to the applied field) can be measured. The maximum magnetisation value that the magnetometer can handle is 3.276×10^{-4} emu. Sample rotation in the *x-y* plane is achieved via a computer controlled motor attached to the VSM head. The rotating system provides an angle resolution of a 10^{th} of a degree and the absolute angular precision is about 1°. A water cooled electro-magnet generates a field up to 1 T in the horizontal plane, with a sweep rate from 0.001 Oe/s to 500 Oe/s. The effective magnetic field applied to the sample is gauged with a Hall probe, which is positioned next to it. The accuracy of the Hall sensor is about 1 Oe. The field was found to be homogeneous in the region of the sample vibration. No cryostat was available, so only room temperature measurements were possible.

The thin films under investigation were patterned in disk form in order to minimize local shape effects and also for symmetry concerns. As mentioned earlier, errors can be minimized providing that the sample remains sufficiently small in comparison to the pick-up coils dimension. This was achieved by preparing disk specimen with a typical size of 3 – 4 mm diameter.

High vacuum grease (*Apiezon*), *Silicone* and *Halogen* free, and a diluted solution of HNO_3 were used to etch the epitaxial films. A picture of a typical sample, prepared for magnetometry measurements, can be seen in Fig. 4.3.

The sample was first placed on the top of a hot plate of copper. The heat propagates through the sapphire, and the multilayer films. This procedure must be carried out very carefully, as an excess of heat can be destructive for the Laves phase compounds. A small drop of grease was then placed at the center of the sample metal surface, which subsequently spread out in the form of a disc.

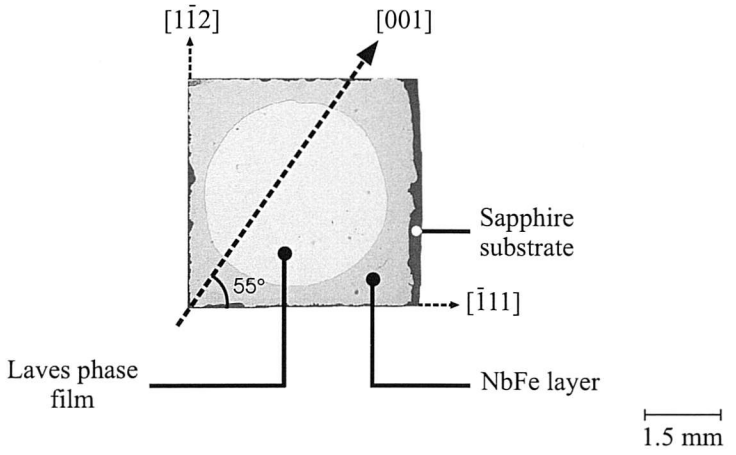

Figure 4.3 Photograph of a sample prepared for magnetisation measurements. The specimen is a 4000 Å epitaxial $DyFe_2$ film. The yellow disk is the film of Laves phase compounds. The green-ish part of the sample is the Nb-Fe buffer layer, which cannot be removed by the etching solution. The low temperature easy axis of the 4000 Å $DyFe_2$ film is shown versus one of the sample edges.

As soon as the disc of grease reached an approriate size, the sample is removed from the heating plate. It then cools down to room temperature, and the grease hardens. It is important to use grease with a melting point 10 - 30 degrees above room temperature to limit the heating of the Laves phase compounds. Also, it must be sufficiently hard at room temperature to be an efficient 'mask'. The sample was then placed in a 3 % HNO_3 solution in methanol (concentration ratio 1.00 : 0.03 CH_3OH : HNO_3), which can dissolve 4000 Å of Laves phase film in 3 - 4 minutes. The disk of grease acts as a mask, *i.e.* the Laves phase film that is not covered by grease is etched away. Note that a higher concentration of HNO_3 can easily dissolve and damage the 'mask'. Nevertheless, the etching solution cannot attack the Nb-Fe layer, which therefore remains. However, the signal induced by that layer in the magnetometric measurement is small (Fig 4.4).

Finally, the sample is rinsed in methanol, and the grease is removed using trichlo-ethylene.

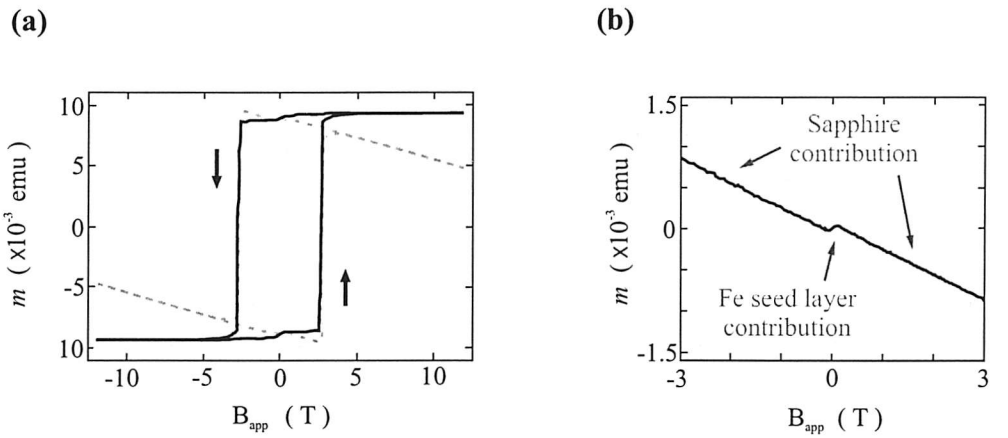

Figure 4.4
a) The magnetic hysteresis loop of a 4000 Å $DyFe_2$ epitaxial film, measured at 10 K. The dashed lines correspond to the primary M-B loop as given by the VSM. The diamagnetic sapphire substrate contribution is clearly apparent at high field. The solid line is the corrected M-B loop, which exhibits saturation feature for large applied field
b) The room temperature magnetic profile of a [100Å Nb / 30Å Fe] film, similar to the buffer layer found at the bottom of the epitaxial Laves phase superlattices. The negative slope of the linear feature is due to the diamagnetic nature of the sapphire substrate. The step at 0 T is clearly due to the 30 Å Fe seed layer. The curve displays a small hysteresis loop in low fields.

The signal measured by the VSM is the total magnetic moment of the sample, including signal from the sample holder, signal from the substrate and signal from the Nb-Fe buffer layer. The sample holder has been magnetically characterised by separate measurements, in order to confirm its negligible magnetic nature. The magnetic films studied in this thesis are on a sapphire substrate of 1 mm thick, substantially greater in volume and mass than the sample itself (~ 4000 Å). The diamagnetic input from the sapphire substrate can be clearly seen at high fields. Here, the magnetic sample saturates but the linear background from the substrate continues to increase with field (Fig. 4.4.a). It is a recurrent characteristic observed for all samples. However, this contribution can easily be removed from the total signal, using its linear diamagnetic behaviour at high field. Another persistent feature is the jump of the magnetisation as the applied magnetic field passes through zero. The measurement of a [100 Å Nb / 30 Å Fe] film, similar to the Nb-Fe buffer layer used to grow the epitaxial Laves phase films, confirms that the magnetisation step

originates from the iron (Fig. 4.4.b). However, this feature does not negate any of the conclusions reached in this thesis.

In presenting the magnetic properties of the epitaxial films, all results are expressed in Bohr magneton per formula unit (μ_B / f.u.). The unit convertion of the measured magnetic moment $m_{(emu)}$ in *emu*, to the magnetisation unit μ_B / f.u ($m_{(\mu_B)}$), is given by the following formula:

$$m_{(\mu_B)} = \frac{m_{(emu)}}{\left(N_{(RE\text{-}Fe_2)_1} + N_{(RE\text{-}Fe_2)_2}\right) \times \mu_B} \tag{4.07}$$

where $N_{(RE\text{-}Fe_2)_1}$ and $N_{(RE\text{-}Fe_2)_2}$ are respectively the total number of $(RE\text{-}Fe_2)_1$ formula unit and $(RE\text{-}Fe_2)_2$ formula unit in the entire specimen.

A detailed derivation of Eq. 4.07, and an explanation for the expression *Bohr magneton per formula unit*, is given in Appendix 1.

References

[1] S. Foner, *Rev. Sci. Instrum.* **30**, 548 (1959)

[2] M. Springford, *et al.*, *J. Phys. E* **4**: 1040 (1971)

[3] J. A. Gerber, *et al.*, *Rev. Sci. Instrum.* **53**: 691 (1982)

[4] D. Halliday, R. Resnick, *Fundamentals of Physics*, John Wiley and Sons Inc., (1970) p.598

[5] J. Mallinson, *J. Appl. Phys.* **37**: 2514 (1966)

[6] C. N. Guy and W. Howarth, *J. Phys. C* **11**: 1635 (1978)

[7] A. Zieba and S. Foner, *Rev. Sci. Instrum.* **53**: 1344 (1982)

[8] E. Jouen *et al.*, *J. Magn. Magn. Mater.* **83**: 548 (1990)

[9] N. Matasubara and F. Sai, *IEEE Trans. Magn.* **27** (6): 4748 (1991)

[10] Technical Bulletin, *Oxford Instruments*, Scientific Research Division, Vibrating Sample Magnetometry- Review of the technique

Chapter 5

Magnetic anisotropy of epitaxially strained Laves phase films

The magnetic anisotropy of a material can be determined from the dynamical and/or static response of the magnetic system. The former can be measured by ferromagnetic resonance and Brillouin light scattering [1]. The latter can be measured by torque magnetometry, torsion oscillating magnetometry [2], the magneto-optical Kerr effet [3], and various techniques such as Vector Sample Magnetometry (VSM) [4]. Mössbauer spectroscopy can also be used to probe the direction of easy magnetisation. [5, 6].

In this chapter, macroscopic magnetic measurements used to investigate the direction of easy magnetisation of built-in strained Laves phase films are reported. The large magnetostriction of $DyFe_2$ and in particular of $TbFe_2$ [7] suggests that one can manipulate the magnetisation orientation with modest strains.

First, a brief review of the current research on the anisotropy properties of strained thin films is given. The re-orientation of the easy axis of MBE Laves phase is discussed in the light of the strong influence of the thermal epitaxial strain. In particular, it is seen to what extent this effect modifies the magnetic properties of those films, and specially their anisotropy via the magnetostrictive coupling. Secondly, the reorientation of the easy axis of the (110) epitaxial films: YFe_2, $DyFe_2$ and $TbFe_2$ is investigated using macroscopic magnetometry technique.

5.1 Introduction

Perhaps, the most remarkable manifestation of the effect of stress on the properties of materials, can be found in the strong increase of the critical temperature of a high quality film of the superconducting II-I-IV compound $(La_{1.9}\,Sr_{0.1})\,CuO_4$ under pressure [8]. The superconducting transition temperature increases from 25 K to 49 K when the film is grown on a substrate that places the superconducting film under compressive epitaxial strain. It is not unreasonable to expect therefore, that strains induced during crystal growth may well modify the magnetic properties of the MBE grown RE-Fe_2 films.

In chapter 2, the various contributions to the magnetic anisotropy of magnetic films were discussed. These include:

- the magneto-crystalline anisotropy of the unstrained material, and
- the magneto-elastic coupling resulting from mechanical stress.

It is clear therefore that the properties of an unstrained magnetic material can be drastically changed by stressing or straining it [5]. In particular, the favoured direction of magnetisation in thin films [6, 10] was found to deviate from that of bulk materials [9]. By using magnetic materials that are sensitive to stress, it is possible to manipulate and control the orientation of their magnetisation with quite modest strains (~ 1%). The RE Laves phase compounds, RE-Co_2 and RE-Fe_2 are especially attractive from this point of view because they possess large magnetic anisotropy and giant magnetostriction. For example, bulk $TbFe_2$ compound possesses a magnetostriction constant $\lambda_{111} = 2460 \times 10^{-6}$ [11], whereas polycrystalline nickel exhibits a magnetostriction of saturation of only -35×10^{-6} [12].

In thin films, built-in strain can originate from:

- a different thermal expansion of the substrate and the film,
- a misfit between the substrate and the magnetic layer, and
- a misfit between the lattice parameters of neighbouring layers.

5.1.1 Thermal built-in strain

The epitaxial growth using MBE technique requires the substrate to be heated to an elevated temperature, typically around 600°C. During the deposition process, the stresses are totally relaxed in the film, and it is clamped to the substrate at the interface. But when the film is cooled down from the growth temperature to room temperature, strains develop as a result of the difference between the thermal expansion coefficients of the substrate and the magnetic film. In Ref. [13], the effects of the substrate on the strains of epitaxial $TbFe_2$ (111) films and consequently on the magnetization direction were reported. 100 Å $TbFe_2$ films were grown on three different substrates: MgO, CaF_2 and Al_2O_3, with an epitaxial W(110) buffer layer. MgO and CaF_2 possess thermal expansion coefficient larger than of the Al_2O_3 (Table I), and the thermal expansion of $TbFe_2$ is about 12×10^{-6} at room temperature [14, 15].

	Al_2O_3	MgO	CaF_2	RE-Fe_2
20°C	5.4×10^{-6}	10.5×10^{-6}	19.1×10^{-6}	16×10^{-6}
550°C	8.6×10^{-6}	14.6×10^{-6}	33.3×10^{-6}	12×10^{-6}

Table I. Thermal expansion coefficient α of Al_2O_3, MgO, CaF_2 and RE-Fe_2 bulk Laves phase at 20°C and 550°C.

From the data in Table I, the thermal strain is given by [13]:

$$\varepsilon = -(\alpha_f - \alpha_s)(T - T_d) = -\Delta\alpha\,\Delta T \qquad (5.01)$$

where α_f and α_S are the thermal expansion coefficient of the film and substrate respectively. Here, T is room temperature and T_d is the deposition temperature.

The thermal strain for Al_2O_3, MgO and CaF_2 substrates is equal to 0.4 %, 0.11 % and -0.61 % respectively. It was found that the magnetisation of the $TbFe_2$ films on the Al_2O_3 and MgO substrates with a tensile thermal strain lies in the plane of the

film. However, the magnetization direction of the $TbFe_2$ film on a CaF_2 substrate, with a compressive thermal strain, is out of the film plane.

The magnetic anisotropy properties can also be strongly modified by varying the epitaxial growth conditions of the films. Indeed, Huth and Flynn [16] showed that $TbFe_2$ (110) films grown on a $(11\bar{2}0)$ Al_2O_3 / Mo (110) substrate possess an easy axis whose direction depends on the temperature of deposition of the Laves phase material. So when the epitaxy films are prepared at 720 K (above the Curie temperature) the films show an in-plane easy magnetization. But, for films grown at 520 K (below the Curie temperature) a perpendicular anisotropy was observed.

5.1.2 Substrate-film mismatch strain

The molecular beam epitaxy technique allows single crystalline magnetic materials to be deposited with a well defined growth direction. Moreover, the film growth direction depends on the crystallographic structure of the substrate and the buffer material. In many cases of interest the film has the same crystal structure as the substrate but their respective lattice parameters may differ. Hence, a mismatch strain ε is induced by the misfit between the substrate and the magnetic layer:

$$\varepsilon = (a_{\text{layer}} - a_{\text{substrate}}) / a_{\text{substrate}} \tag{5.02}$$

where a_{layer} and $a_{\text{substrate}}$ are the lattice constant of the crystal magnetic compound and of the substrate, respectively [17]. The epitaxial layers adopt in-plane lattice parameters that closely match those of the buffer, while the perpendicular parameters adjust to satisfy the elasticity rules of the materials.

5.1.3 Lattice mismatch strain

In layered systems, the misfit between the lattice parameters of two superimposed layers can also induced change in the magnetic anisotropy properties of the films [18]. It has been shown that the epitaxial Cu / Ni / Cu (001) trilayer exhibits a strong perpendicular magnetization over a broad range of the nickel film thickness. The nickel magnetic moment prefers to point out of the plane of the film for the nickel

film thickness ranging from 20 Å to 120 Å [19]. The broad range of perpendicular anisotropy is due to the large residual strain in the nickel layer. Epitaxial nickel on copper is under a biaxial tensile stress due to the lattice mismatch in their bulk forms. The lattice mismatch gives rise to isotropic strain in the (001) plane:

$$\varepsilon_{xx} = \varepsilon_{yy} = \varepsilon_{\parallel} = (a_l - a_b)/a_b \tag{5.03}$$

(a_b is the bulk lattice constant of Ni and a_l is the lattice constant of the Ni in the layered system), and to an out-of-plane compression strain:

$$\varepsilon_{\perp} = -(2C_{12}/C_{11})\varepsilon_{\parallel} \tag{5.04}$$

due to the Poisson effect. Here the C_{ij} are the elastic constants of the bulk Ni.

5.2 Effect of the thermal epitaxial strain on the magnetisation of (110) RE-Fe_2 thin films

The strain induced in the MBE Laves phase films grown on sapphire substrate is dominantly thermal epitaxial strain [20]. It results from the difference between the thermal expansion coefficient of the sapphire substrate α_S and of the Laves phase α_R film [13], induced during the cooling process from the deposition temperature down to room temperature.

Using Eq. 5.01 and the values given by Table I, the in-plane strains at room temperature is $\varepsilon_{\parallel} = +0.38$ %. Therefore, the RE-Fe_2 crystal lattice parameter $a_{\parallel}^{s}$, which is the distance between planes perpendicular to the film surface, is expanded. The expansion in the plane is accompanied by a compression perpendicular to the plane. The lattice parameter perpendicular to the film plane $a_{\perp}^{s}$ is then smaller than the equivalent bulk lattice parameter. The perpendicular strain can be deduced from Eq. 5.04: $\varepsilon_{\perp} = -0.13$ %. From these values, it is estimated that the Laves phase films are subject to a shear strain $\varepsilon_{xy} = -0.5$ % [17]. Another method to determine the shear strain consists in using the following equation:

$$\varepsilon_{xy} = \frac{a_{\perp}^{s} - a_{\parallel}^{s}}{2a^{s}} \tag{5.05}$$

where a^s is the average parameter. The parameters $a_{\perp}^{s}$ and $a_{\parallel}^{s}$ are determined by direct measurements using grazing incident X-Ray diffraction [20].

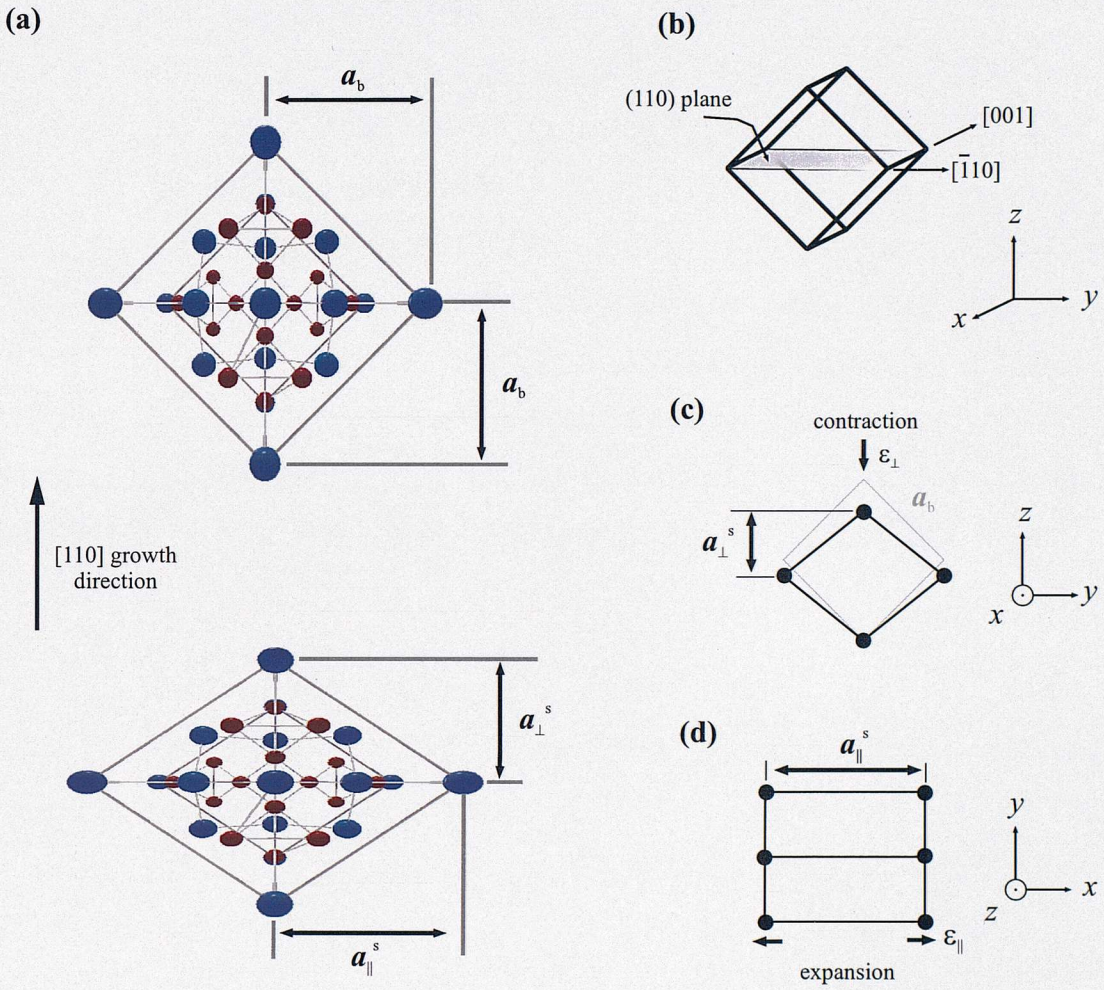

Figure 5.01 Schematic representation of a cubic crystal Laves phase deformed by a shear strain as observed in epitaxially grown RE-Fe_2 films.

a) The top picture shows the cubic Laves phase as found in bulk. At the bottom, the geometry of the RE-Fe_2 crystal strained by the sapphire substrate can be seen: $a_{\perp}^{s} < a_{\parallel}^{s}$.

b) Sketch of a single crystalline Laves phase in the bulk form.

c) Compression of the cubic crystal in the growth direction as a result of **(d)** its expansion in the film plane.

To investigate the influence of the structural deformation of the Laves phase cubic crystal upon the magnetisation, it is required to study the total energy of the system:

$$E = E_{mc} + E_e + E_{me} + E_{sh} \tag{5.06}$$

The spontaneous orientation of the magnetisation at zero field is then determined from the minimization of that energy. The different terms in Eq. 5.06 are:

- E_{mc} is the magneto-crystalline energy (Eq. 2.14):

In bulk material, the direction of easy magnetisation is related to the sign and value of both K_1 and K_2 anisotropy coefficients. In bulk $DyFe_2$, $K_1 > 0$ and $|K_2| / K_1 < 9$ [21], hence the easy axis is along <100>.

- E_{me} is the magneto-elastic (MEL) energy, and is characterised by the parameters b_0, b_1, b_2 (Eq. 2.23). The first term (proportional to b_0) in the MEL energy may be ignored, as it is independent of the magnetisation direction cosines α_i. Secondly, Mougin *et al.* [17] have argued that the magneto-elastic constant b_2 is two orders of magnitude larger than b_1. Thirdly, the strains terms ε_{xz} and ε_{yz} are equal to zero as a result of the homogeneous strains in the (110) film plane. Thus, Eq. 2.23 reduces to:

$$E_{me} = b_2 \alpha_x \alpha_y \varepsilon_{xy} \tag{5.07}$$

Thus, if b_2 and ε_{xy} are both negative, the MEL energy is minimum when the magnetisation vector $\vec{M}$ is along $[\bar{1}\,10]$ or $[1\,\bar{1}\,0]$

- E_e is the elastic energy (see Eq. 2.24). In the present case, E_e is given by:

$$E_e = \frac{1}{4} C_{44} \varepsilon_{xy}^{\,2} \tag{5.08}$$

It can be seen that the elastic energy is independent of the magnetisation direction cosines α_i.

- E_{sh} is the shape anisotropy

$$E_{sh} = \frac{1}{2} \mu_0 M^2 (\alpha_x^{\,2} + \alpha_y^{\,2}) \tag{5.09}$$

As expected, shape anisotropy favours in-plane alignment of the magnetisation vector.

With these simplifications, Eq. 5.06 becomes:

$$\begin{aligned} E = K_1(\alpha_x^2\alpha_y^2 + \alpha_y^2\alpha_z^2 + \alpha_z^2\alpha_x^2) + K_2(\alpha_x^2\alpha_y^2\alpha_z^2) \\ + b_2\alpha_x\alpha_y\varepsilon_{xy} + \frac{1}{4}C_{44}\varepsilon_{xy}^2 + \pi M^2(\alpha_x^2 + \alpha_y^2) \end{aligned} \tag{5.10}$$

The equilibrium direction of the magneisation vector is determined by minimizing the total energy E. It is clear from Eq. 5.10 that the strain term therefore modifies the usual single-ion anisotropic energy terms, and it plays an important role in determining the magnetisation direction of the film.

In $DyFe_2$ and $TbFe_2$, in particular, the MEL energy is large enough to strongly influence the magnetic easy axis of the epitaxial RE-Fe_2, which differs dramatically from that of their respective bulk materials. In Ref [15], it was shown that the ratio b_2 / K_1 is strongly temperature dependent. In particular, at low temperatures K_1 is dominant and the easy axes of the thin films and their respective bulk compounds are identical. At higher temperatures however, the MEL term dominates and the magnetisation does not follow that of the bulk compound. Thus the direction of easy magnetisation is temperature dependent.

5.3 Probing the easy axis of epitaxial RE-Fe_2 films with built-in strain

The magnetic characteristics of the bulk $DyFe_2$, $TbFe_2$ and YFe_2 compounds are summarised in Table II.

	$DyFe_2$	$TbFe_2$	YFe_2
T_C [4]	$\mu_{Fe} \times (B_{ex}^{Fe} + B_{ex}^{Dy})$ ~ T_C ~ 635 K	$\mu_{Fe} \times (B_{ex}^{Fe} + B_{ex}^{Tb})$ ~ T_C ~ 700 K	$\mu_{Fe} \times (B_{ex}^{Fe} + 0)$ ~ T_C ~ 550 K
easy axis [23]	<001>	<111>	<111>
$M_{sat.}$ (μ_B / f.u)	7 at 10 K	4.5 at 300 K	3 at 10 K
K_1 (J / m^3) at 300 K	$+2.1 \times 10^6$	-7.6×10^6	*small*
Lattice parameter (Å)	7.325	7.347	7.363
Saturation magnetostriction constant (*ppm*) [23]	$\lambda_{001} = 4 \times 10^{-6}$	$\lambda_{111} = 2450 \times 10^{-6}$	*practically non magnetostrictive*
b_2 (J / m^3) MEL coupling coefficient [17]	-1.8×10^8 at 300 K	-3.7×10^8 at 300 K	~ 0

Table II. Characteristic parameters of $DyFe_2$, $TbFe_2$ and YFe_2 bulk compound.

5.3.1 Epitaxial YFe_2 film

Fig. 5.02 shows the hysteresis loop of a 1000 Å YFe_2 epitaxial thin film at different temperatures. The compound was magnetically characterised, using a VSM. The field, in the range of 5 T, was applied along the in-plane [001] direction.

The magnetisation measurements provide a value for the magnetic moment of 3 μ_B / f.u at 10 K. If it is assumed that the Yttrium ions do not carry a magnetic

[4] It was shown by Atzmony and Daniel [22] that B_{ex}^{RE}, the exchange field RE-RE in RE-Fe_2 compounds, is between 100 T and 225 T, depending on the rare earth.

moment, then the magnetisation is attributed to the Fe atoms 1.5 μ_B per Fe atoms. This is consistent with the bulk results of A. E. Clark [22]. In his work, the iron sublattice moment was calculated from the spontaneous moment under the assumption of a full trivalent moment of the rare earth ions.

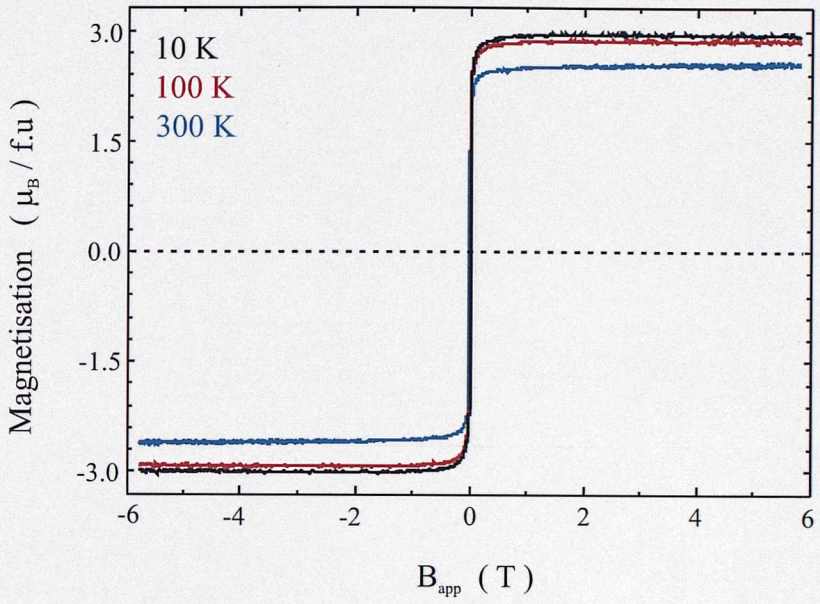

Figure 5.02 Selection of hysteresis loops of a 1000 Å thick epitaxial YFe_2 thin film. The magnetic field B_{app} is along the in-plane [001] direction. The larger magnetization of saturation is obtained at 10K, and it decreases with increasing temperature.

It was shown that the moment of the Fe ions is close of 1.5 ± 0.5 μ_B / Fe ion in the heavy RE-Fe_2 compounds. Note also that YFe_2 can be considered as a soft magnetic material because it possesses a small coercivity B_C of 0.03 T at 10 K.

In Fig. 5.03, the hysteresis loops of the epitaxial YFe_2 film for different directions of the applied magnetic field can be seen. The magnetic measurements were carried out at 290 K within a magnetic field range of 0.8 T.

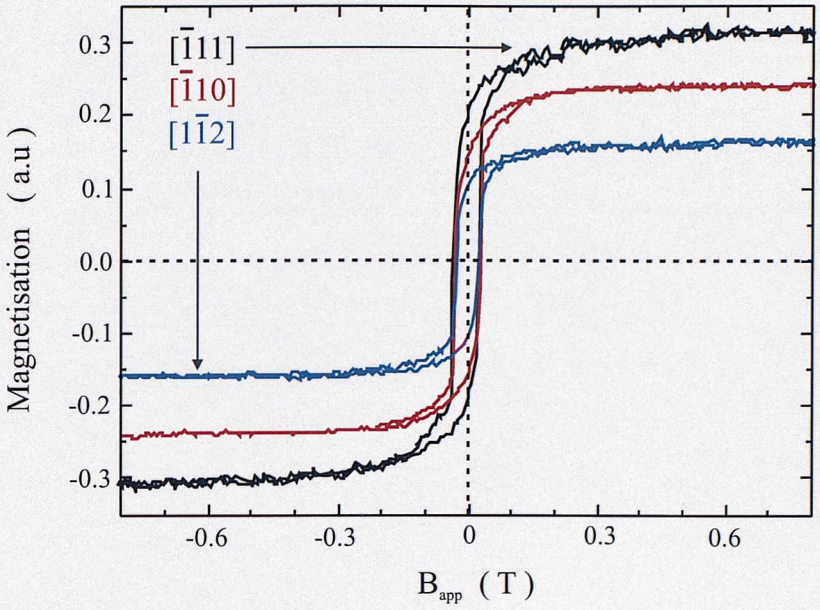

Figure 5.03 Room temperature hysteresis loops of epitaxial a 4000 Å thick YFe_2 film for different in-plane directions of the applied field. The magnetisation is in arbitrary unit (a.u).

The parameters B_C (the coercive field) and M_S (the magnetisation of saturation) are summarized in Table III.

$\vec{B}_{app}$ ‖	[$\bar{1}$ 11]	[1 $\bar{1}$ 2]	[$\bar{1}$ 10]
B_C (T)	0.03	0.024	0.028
M_S (a.u.)	0.31	0.16	0.24

Table III Coercivity and magnetisation of saturation extracted from the hysteresis loops shown in Fig. 5.03.

The M-B_{app} loops prove that the direction of easy magnetisation is close to [$\bar{1}$ 11] at 290 K. Indeed, the largest magnetisation and largest coercivity are obtained when the field is along the [$\bar{1}$ 11] direction. Mougin *et al.* [17] showed that at 4.2 K, the magnetisation of a 1000 Å YFe_2 film epitaxially grown lies preferentially in the

plane of the sample close to the [$\bar{1}$ 11] direction. Thus, it will appear that the easy axis remains along the same direction in the temperature range $4.2 \leq T \leq 290$ K.

Finally, it is worth noting that epitaxial strains in YFe_2 films are not expected to induce much in the way of a change in direction of easy magnetisation with increasing temperature, because YFe_2 is a weakly magnetostrictive compound. But against this, a shift of the magnetisation away from the directions <111> may occur. After Ref. [24], an increase of the exchange anisotropy between Fe ions due to strains induced in the iron sublattice by epitaxy may reorient slightly the magnetisation.

5.3.2 Epitaxial $DyFe_2$ film

5.3.2.a Experimental results

A 1000 Å thick $DyFe_2$ film, epitaxially grown along the direction [110], was magnetically characterised at different temperatures from 5 to 300 K. The magnetic fields in excess of 12 T, were applied along the in-plane [001] axis. The results of the magnetic measurements can be seen in Fig. 5.4.

The film is characterised by a large saturation magnetisation of 7 μ_B / f.u at 10 K. This confirms the anti-ferromagnetic coupling between the Fe ions (1.5 μ_B per Fe atom) and the Dy^{3+} ions (10 μ_B per Dysprosium ion). The 10 K hysteresis loop displays a coercive field of 3 T. The large anisotropy of $DyFe_2$ is due mainly to the single-ion crystal field anisotropy of the Dy^{3+} ions [25]. Thus, $DyFe_2$ is an archetypal strong ferromagnetic material.

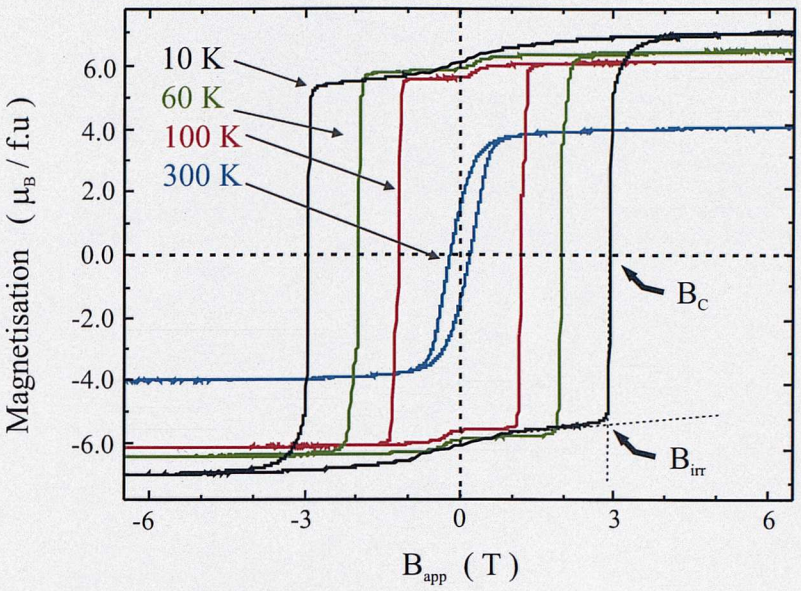

Figure 5.04 The in-plane hysteresis loop of a 1000 Å MBE grown $DyFe_2$ film for different temperatures, and fields applied along an in-plane [001] direction. B_{irr} is the field from which the magnetisation reversal occurs.

The hysteresis loop of the $DyFe_2$ film when the field is applied along the $[\bar{1}\,10]$ (90° away from the [001] axis) was measured at 10 K. The sample exhibits a square hysteresis loop, with a remanent magnetisation close to the high field magnetisation. However, the coercivity is smaller (2.8 T) when $\bar{B}_{app}$ along $[\bar{1}\,10]$. In addition, when a large field of +7 T is applied, the magnetisation reaches 77 % of the saturation magnetisation obtained when $\bar{B}_{app}$ towards [001] axis. It may be conclude therefore that the [001] direction is the easy axis of magnetisation at low temperatures. However, unlike the bulk material, the MBE grown $DyFe_2$ thin film displays uniaxial anisotropy, because:

(*i*) of the shape anisotropy, which favours in-plane directions and

(*ii*) there are only two [001] and $[00\,\bar{1}]$ axes in the plane of the film.

At higher temperatures, however a change in the curvature of the hysteresis loops occurs (Fig. 5.04). The M-B_{app} loops become more and more 'skewed' as the temperature approaches room temperature. Thus at room temperature, the [001] direction is not the direction of easy magnetisation.

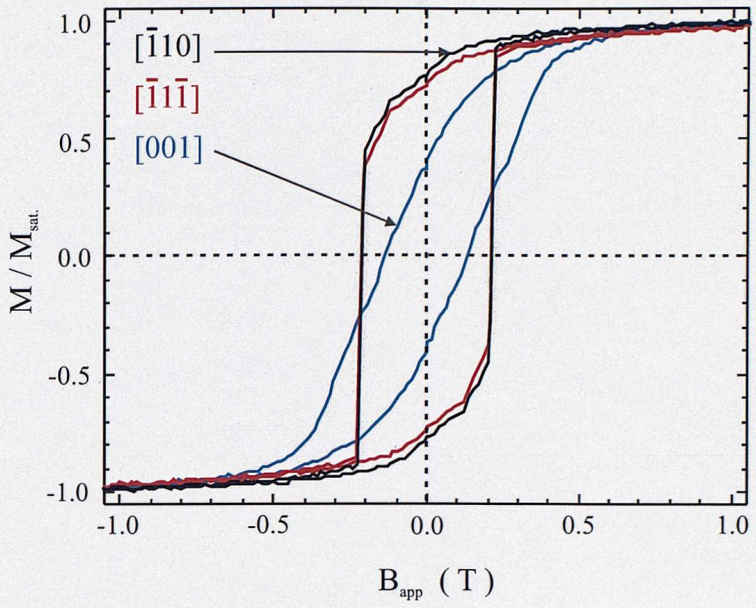

Figure 5.05 Magnetic curves of single crystalline $DyFe_2$ thin film at 290 K, when the field is applied along different cubic crystallographic direction

To investigate the reorientation of the direction of magnetisation, the magnetic profile of the film was measured at room temperature in a field range of 4 T, using a VSM. Fig. 5.05 shows the magnetisation loop for three different directions of B_{app} versus in plane crystallographic axis: [001], [$\bar{1}$ 10] and [$\bar{1}$ 1 $\bar{1}$].

The magnetic loop obtained with the field along [001] direction is nearly 'skewed' and typical of a hard magnetisation axis. However, the magnetisation at 290 K is more easily saturated along [$\bar{1}$ 10] than along the low temperature easy axis [001]. It may be concluded therefore that the easy axis at room temperature is close to the [$\bar{1}$ 10] axis. In addition, it can be seen that the coercivity B_C exhibits the largest value when the field is applied along [$\bar{1}$ 10] and along [$\bar{1}$ 1 $\bar{1}$]: B_C ~0.22 T. A more complete investigation of the variation of B_C versus the angle between the [001] axis and the direction of the field is shown in Fig. 5.06. The field in excess of 1 T was applied in the plane of the film. It is clear that the film still exhibits a uniaxial anisotropy at room temperature. However, the [001] direction is now a hard axis, and the axis of easy magnetisation is close to [$\bar{1}$ 10].

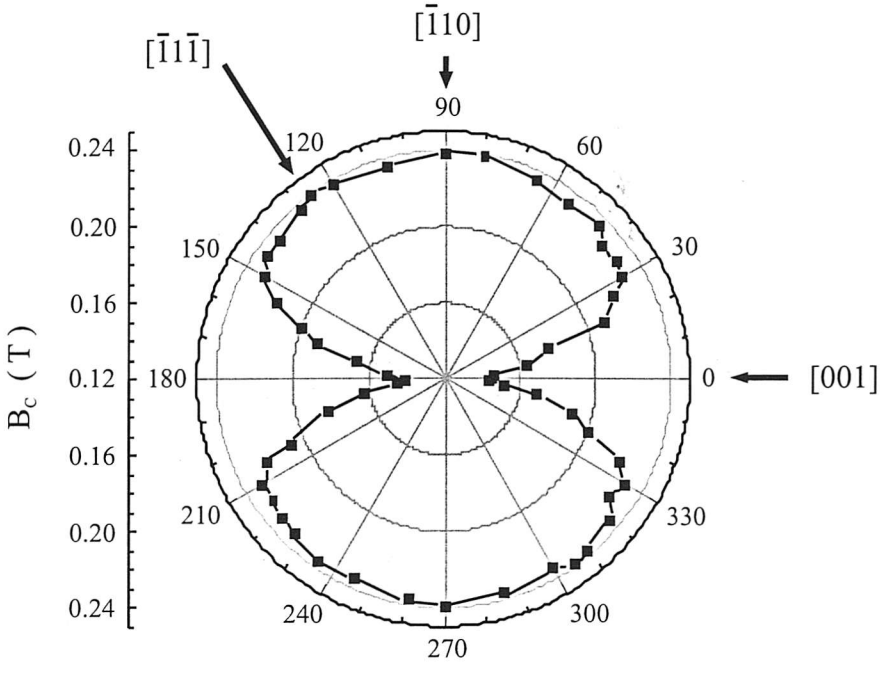

Figure 5.06 Coercivity for different angle between the applied field and the crystallographic direction for single crystalline $DyFe_2$ at 290 K.

5.3.2.b Discussion

The quantity $(B_C - B_{irr})$ can be used to quantify the change of curvature of the hysteresis loop as the temperature is changed. Hence, the re-orientation of the easy axis can be probed. The evolution of this parameter as a function of the temperature can be seen in Fig. 5.07.

For $T < 100$ K, $(B_C - B_{irr})$ is small (~ 0.035 T) and constant. In this flat portion of the graph, the [001] direction is the favoured direction of the magnetisation. But, when $100 \leq T \leq 300$ K, the parameter increases with increasing temperature: $d(B_C\text{-}B_{irr}) / dT \sim 0.0011$ T / K. This indicates that the direction of easy magnetisation reorients for $T > 100$ K. Unlike bulk $DyFe_2$, the easy axis in MBE grown $DyFe_2$ films is therefore temperature dependent.

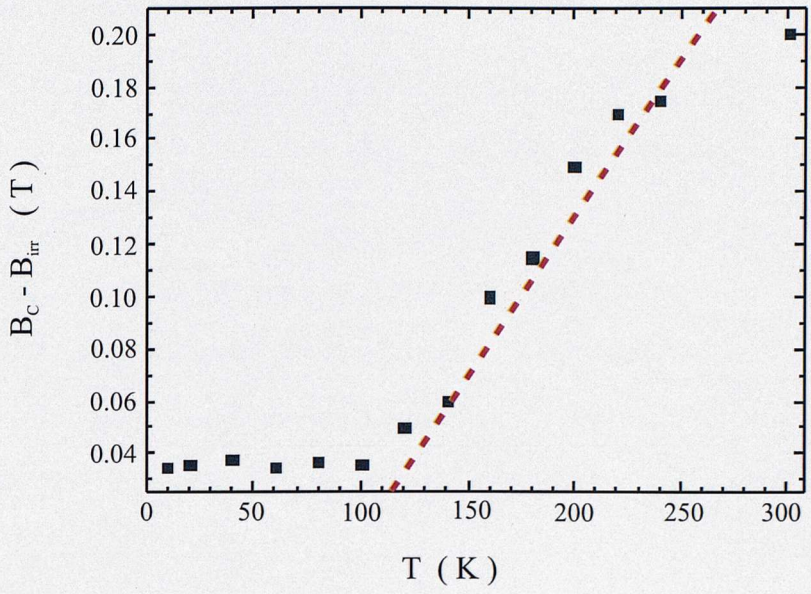

Figure 5.07 ($B_C - B_{irr}$) as a function of temperature T for MBE grown $DyFe_2$ film. The dashed line is a linear fit of the evolution of ($B_C - B_{irr}$) versus T, for T > 100 K.

The result is consistent with Mössbauer experiment by Oderno *et al.* [26] who showed that at 4.2 K the easy axis of $DyFe_2$ epitaxial film is [001], and at room temperature the easy axis is close to the in-plane direction [$\bar{1}$10]. The shape of the respective hysteresis loop around zero applied field (Fig. 5.05) suggests that the MBE film does not exhibit an in-plane magnetisation at 290 K. Indeed, the remanent magnetisation is about 80% of the value of the magnetisation of saturation. This decrease of the magnetisation can be interpreted as follows: when the magnetic field decreases from high value, the magnetisation rotates coherently from the direction of $\vec{B}_{app}$ to the easy axis. It is suggested that the easy axis at 290 K lies along [$\bar{1}$10] and out of the plane of the film. Furthermore, A. Mougin *et al.*, by using Mössbauer technology, found that the most probable direction of the magnetisation at room temperature is [$\bar{3}$51]. [17]

5.3.3 Epitaxial $TbFe_2$ film

The magnetic properties of a 4000 Å $TbFe_2$ film was measured in a field range of 5 T at room temperature. Fig. 5.08 presents the typical hysteresis loops of the $TbFe_2$ sample for $\vec{B}_{app}$ along $[\bar{1}\,10]$, [001] and $[\bar{1}\,1\,\bar{1}]$.

The largest B_C is obtained when $\vec{B}_{app}$ is applied along $[\bar{1}\,10]$ and $[\bar{1}\,1\,\bar{1}]$: $B_C \sim 0.63$ T. Note that the M-B_{app} loops are square and typical of easy axis hysteresis curves. However, the largest remanent magnetisation M_{rem} is seen for $\vec{B}_{app} \parallel [\bar{1}\,10]$: M_{rem} is about 93% of the value of the magnetisation at high field. This suggests that the easy axis is closer to $[\bar{1}\,10]$.

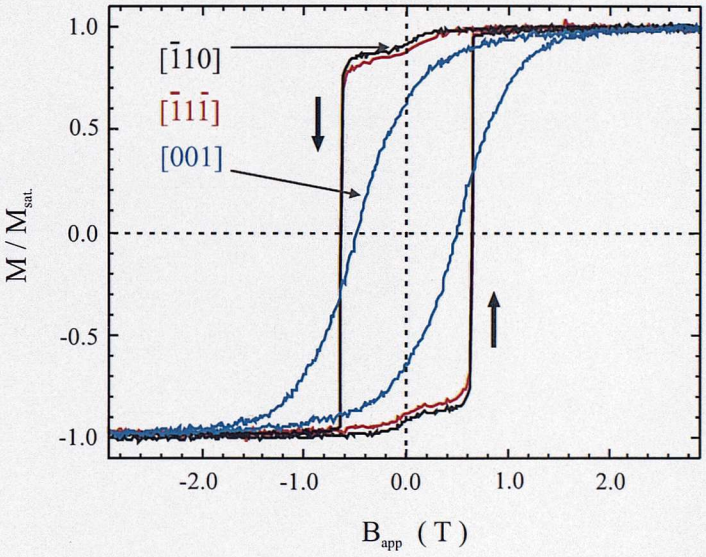

Figure 5.08 Magnetisation curves for single crystalline $TbFe_2$ at 290 K for magnetic field applied along different sample crystallographic axis.

In contrast, when the field is applied along [001], the hysteresis loop shows a 'skewed' shape. The coercivity is small ($B_C = 0.49$ T) and the remanent magnetisation is about 60 % of the value of the saturation magnetisation. Thus [001] axis is definitely not a direction of easy magnetisation.

The magnetic behaviour of epitaxial $TbFe_2$ film is in contrast with that of the bulk. Indeed, it is known that the easy axis of $TbFe_2$ bulk is the equivalent directions

<111> for all temperatures [23]. In Ref. [17], it was found that for epitaxial film, the easy axis at low temperature is the in-plane directions [$\bar{1}$ 1 $\bar{1}$] and [$\bar{1}$ 11]. It can be thus suggested that there is spin reorientation with temperature. At low temperatures, the direction of easy magnetisation is imposed by the crystalline anisotropy. However, for higher temperatures, the MEL energy which favours a [$\bar{1}$ 10] ($b_2 < 0$ [20]) dominates over that of magneto-crystalline anisotropy. Therefore, the MEL term dictates that the [$\bar{1}$ 10] axis is the easy axis at room temperature.

5.4 Conclusions

The growth of epitaxial Laves phase on top of Al_2O_3 substrates has triggered changes in their magnetic characteristics. Indeed, the large epitaxial strain induced by the small sapphire substrate thermal expansion induced a MEL term, which affects the overall anisotropy energy. At low temperatures, the RE magneto-crystalline energy and the shape anisotropy are large enough to dictate the direction of easy magnetisation. However, when the temperature is increased, the relatively strengths of the MEL energy and magneto-crystalline energy change resulting in the domination of the MEL energy over the RE magnet crystal anisotropy. Consequently, unlike bulk, the built-in strain epitaxial Laves phase films gives rise to a re-orientation of magnetisation with temperature. The phenomenon is particularly clear for $DyFe_2$ compound. Indeed, it was found that the easy axis of the epitaxial film is along [001] at temperatures below 100 - 120 K, with [$\bar{1}$ 10] as a hard axis. However, at higher temperatures, the easy/hard axes are reversed, the easy axis being closer to [$\bar{1}$ 10] axis. Thus significant modifications of the magnetic anisotropy, related to the epitaxial strains, and to the sign and the relative importance of the anisotropy and magneto-elastic constants of the compounds, have been observed.

Similar reorientation of the easy axis was seen for other highly magnetostrictive material: $TbFe_2$. The easy axis of the epitaxially grown $TbFe_2$ film shifts from the

in-plane [$\bar{1}$ 11] and [$\bar{1}$ 1 $\bar{1}$] axis at low temperatures to a direction close to [$\bar{1}$ 10] at room temperature.

By way of contrast, the weakly magnetostrictive YFe_2 Laves phase compound displays a different behaviour. Indeed, the epitaxial YFe_2 film and the bulk were found to possess the same direction of easy magnetisation at low temperatures and room temperature, namely the in-plane [$\bar{1}$ 11] axis.
Furthermore, it is worth noting that all three samples display an effective two-fold symmetry, despite their nominally cubic structure.

In conclusion, magnetic anisotropy properties of $TbFe_2$ and $DyFe_2$ epitaxial films can be strongly modified by built-in epitaxial strains. The epitaxial strain and 'clamping' add further complexity to the interplay of various energy contributions that govern key the direction of easy magnetisation.
By varying the epitaxial growth conditions, it should be possible to grow samples with magnetic anisotropy similar to that of their bulk form at all temperatures. One possibility is to reduce the temperature of deposition of the Laves phase materials. This is possible if a Pulse Laser Deposition is used in preference to MBE technique. Indeed, the Laser ablation process generates non-thermal energy species giving a high atom mobility on the substrate. This favours epitaxy even at low temperature.

References

[1] B. Heinrich and J. F. Cochran, *Adv. Phys.* **42** (5): 523 (1993)
M. From *et al.*, *J. Appl. Phys.* **75** (10): 6181 (1994)
B. Hillebrandes *et al.*, *Phylos. Mag. B - Phys. Of Condens. Matter. Stat. Mech. Elect. Opt. and Magn. Prop.* **70** (3): 767 (1994)

[2] R. Bergholz and U. Gradmann, *J. Magn. Magn. Mater.* **45**: 389 (1984)

[3] C. Liu and S. D. Bader, *J. Magn. Magn. Mater.* **93**:307 (1991)

[4] H. Zijlstra, *Rev. Sci. Instrum.* **41**: 1241 (1970)

[5] D. Sander *et al.*, *J. Magn. Magn. Mater.* **200**: 439-455 (1999)

[6] S. W. Sun and R. C. O' Handley, *Phys. Rev. Lett.* **66**: 27983 (1991)

[7] A. E. Clark, *Magnetostrictive RFe_2 intermetallic compounds*, in K. A. Schneider Jr, Eyring (Eds), Handbook on the Physics and Chemistry of RE, North Holland, Amsterdam (1978)

[8] J-P. Locquet *et al.*, Nature **394**: 453-6 (1998)

[9] M. Farle, *Rep. Prog. Phys.* **61**: 755 (1998)
D. Sanders, *Rep. Prog. Phys.* **62**: 809 (1999)

[10] H. Szymczak, *I.E.E.E. Trans. Magn.* 30: 702 (1994)

[11] A. E. Clark, *A. I. P. Conf. Proc.* **18**: 1015 (1974)

[12] Coinasi, *Encyclopedia of Magnetic and Superconducting Materials*, *ed.* J. Evetts, Pergamor Press, Oxford, p.284 (1992)

[13] C-T. Wang *et al.*, *I.E.E.E Trans. Magn.* **32** (5): 4752 (1996)

[14] Y. S. Touloukian *et al.*, *Thermophysical Properties of Matter*, vol. **13**, New York: IFI / Plenum (1977)

[15] A. Mougin *et al.*, *Phys. Rev. B* **59** (8): 5950 (1999)

[16] M. Huth and C. P. Flynn, *J. Magn. Magn. Mater.* **204**: 204 (1999)

[17] A. Mougin *et al.*, *Phys. Rev. B* **62**: 9517 (2000)

[18] W. D. Nix, *Metall. Trans. A* **20**: 2217 (1989)

[19] J. Lee *et al.*, *Phys. Rev. B* **56** (10): 5728 (1997)

[20] W. C. Marra, *J. App. Phys.* **50**: 6927 (1979)

[21] A. E. Clark, *Magnetostrictive RE-Fe_2 compounds on the Physics and Chemistry of RE*, edited by K. Gschneidner Jr, Vol.2, Chap. 15 (1979)

[22] U. Atzmony and M. P. Daniel, *Phys. Rev. B* **13**: 4006 (1976)

[23] A. E. Clark, *Ferromagnetic Materials*, edited by E. P. Wohlfarth, Amsterdam, North-Holland (1980)

[24] G. J. Bowden *et al.*, *J. Phys. F* **3**: 2206 (1976)

[25] G. J. Bowden *et al.*, *J. Phys. C* **1**: 1376-87 (1968)

[26] V. Oderno *et al.*, *Phys. Rev. B* **54**: R17375-8 (1996)

[27] E. C. Stoner and E. P. Wohlfarth, *Phil. Trans. R. Soc.* **240**: 599-642 (1948)

Chapter 6

The coercivity of RE-Fe_2 multilayer and alloy films

Among the parameters characterising magnetic materials is the coercivity B_C. Control over B_C is the critical requirement to optimize the behaviour of magnetic devices for specific practical applications. In particular, high coercive field materials, are widely used in electro-mechanical devices. Concurrently with experiment, it is also useful to develop theoretical models which can be used to interpretate M vs. B_{app} magnetic loops. One of the most successful models is that of Stoner and Wohlfarth [2].

In this chapter, the magnetisation reversal mechanism in the anti-ferromagnetically coupled $DyFe_2 - YFe_2$ multilayer structure and in the highly magnetostrictive $Tb_{(1-x)}Dy_xFe_2$ Terfenol-type alloy system is discussed. The structure of the chapter is as follows.

In the first section, the Stoner and Wohlfarth model for a single phase system is presented and discussed. Secondly, the model is generalised to artificially engineered 2-phase multilayer structures, and its predictions are subsequently compared to the experimental data for a series of $[w\ DyFe_2 - (1-w)\ YFe_2]\times N$ multilayer films, where w is the thickness of the $DyFe_2$ layer and N is the number of the bilayer repeat. The Stoner and Wohlfarth model is also used to predict the coercive field of the epitaxial TbDyFe alloy in the (1-x):x:2 stochiometric ratio.

6.1 Introduction

The original expression of the Stoner and Wohlfarth model

When a hard ferromagnetic (FM) material is magnetised in an applied field, it will not relax back to zero magnetisation when the field is removed. In practice, a reverse field is required to drive the magnetisation to zero. The amount of reverse driving field required is known as the *coercivity* or *coercive field* [3]. Physically, it corresponds to a situation where the barrier between two states of magnetisation is reduced to zero, allowing the system to make a jump to a lower energy state. The coercive field in magnetic materials strongly depends on both their intrinsic magnetic properties and their microstructure. For instance, in thin epitaxial films the main contribution to the coercive field is believed to originate from film imperfections such as roughness and misfit dislocations, as well as intrinsic features such as single-ion anisotropy.

In practice, it is necessary to be specific regarding the way in which the magnetisation reverses since there are two mechanisms by which this may occur: by coherent rotation of the net magnetisation, or by the motion of domains. The coherent rotation is the simplest classical and the most understood form of nucleation process.

The model was introduced 50 years ago by *Néel* [4] and *Stoner and Wohlfarth* [1] to derive an analytical description of the reversal of a magnetic system. However, *Néel*'s model includes the effect of thermal activation that helps to reverse the system's magnetisation, and hence reduces the magnitude of the reverse field.

In the simplest version of the Stoner and Wohlfarth (S-W) model, the effect of a magnetic field upon an ensemble of non-interacting *single-domain* particles is considered [5]. The model assumes that all spins in the system are always parallel with respect to each other and are subject to a uniaxial magneto-crystalline anisotropy. The net magnetisation can then be represented by a single vector $\vec{M}$.

When the magnetic field $\vec{B}_{app}$ is applied along the easy axis, the system exhibits a square hysteresis loop, shown schematically in Fig. 6.1.a.

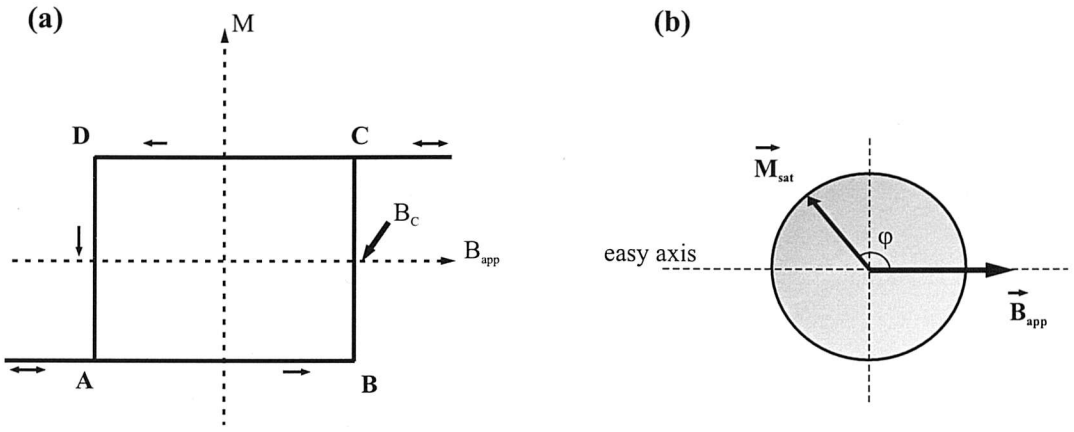

Figure 6.1
a) The hysteresis loop of a single-domain particle. The magnetic field is applied along the easy axis. A, B, C and D designate the points of phase transition.
b) The geometrical configuration of a circular system of single domains particle. B_{app} is along the easy axis and the vector magnetisation M_{sat} rotates to the direction of the increasing magnetic field.

Initially, the system has been magnetically saturated ($-M_{sat}$) by application of a very large negative magnetic field. Upon removal of the field ($A \rightarrow B$), the magnetisation $-M_{sat}$ remains stubbornly pointing in the opposite direction of $\vec{B}_{app}$. Then, there is a discontinuous jump in magnetisation, the magnetisation crossing the $M = 0$ axis at $B_{app} = B_C$. Subsequently, the magnetisation is fixed at $+M_{sat}$ ($C \rightarrow D$).

The M-B loop can be described by minimising the total magnetic energy density of the system. This energy is defined as the sum of the anisotropy energy density and the Zeeman energy density. As the particles are assumed to be parallel, the exchange energy E_{ex} is unaffected and can be safely ignored. Specifically:

$$E = K_A \sin^2 \varphi + M_{sat} B_{app} \cos \varphi + E_{ex} \qquad (6.01)$$

where K_A is the uni-axial crystal field anisotropy parameter, which favours $\varphi = 0^\circ$ or 180°. All other symbols possess their usual meanings. For simplicity, the shape anisotropy is ignored in this analysis.

The stable energy state is found by minimizing the total magnetic energy: $\partial E / \partial \varphi = 0$. The first derivative yields:

$$\frac{\partial E}{\partial \varphi} = 2K_A \cos\varphi \sin\varphi - M_{sat} B_{app} \sin\varphi \qquad (6.02)$$

and results in two possible solutions: $\sin\varphi = 0$ and $\cos\varphi = (M_{sat} B_{app})/2K_A$. To distinguish between the minimum and maximum energy solutions, the second derivative equation $\partial^2 E / \partial \varphi^2 \geq 0$ must be examined:

$$\frac{\partial^2 E}{\partial \varphi^2} = 2K_A \cos 2\varphi - M_{sat} B_{app} \cos\varphi \qquad (6.03)$$

It is then easily shown that the solution $\sin\varphi = 0$ represents the true minimum *i.e.*:

$$\frac{\partial^2 E}{\partial \varphi^2} = 2K_A - M_{sat.} B_{app} \geq 0 \quad \Rightarrow \quad 2K_A \geq M_{sat.} B_{app}$$

Thus we can identify a critical field B_C which is in fact the coercive field:

$$B_C = \frac{2K_A}{M_{sat}} \qquad (6.04)$$

Qualitatively, the equation $(B_C \bullet M_{sat}) \geq 2K_A$ can be understood as followed: the anisotropy energy stabilises the magnetisation vector in a certain crystallographic direction. When a reverse magnetic field is applied to switch the magnetisation, this field must exceed a certain critical value in order to rotate the net magnetic moment M_{sat} over the anisotropy energy barrier.

6.2 Modified form of the Stoner and Wohlfarth model

In this section, a modified form of the S-W model is investigated for a strongly exchange coupled 2-phase system. The specimen is made up of two different FM materials indexed (*i*) and (*j*) (Fig. 6.2.a). The assumptions of the model are briefly reviewed here:

- (*i*) and (*j*) are two single domain particles
- the entire system exhibits a net uni-axial magneto-crystalline anisotropy
- the net magnetisation can be represented by a single vector $\vec{M}_{sat}$
- the magnetisation reversal occurs by coherent rotation of $\vec{M}_{sat}$

However, it is assumed that the two single domain particles are strongly coupled. Consequently, the complete system behaves as a single magnetic entity, and its hysteresis loop is similar to that shown in Fig. 6.1.a.

The equation (6.01) must be modified in order to include the magnetic energy associated with the two materials (*i*) and (*j*) and also the exchange energy E_{ex} associated with the exchange interactions occurring between the 2 phases. Within the frame of those modifications, the equation (6.01) becomes:

$$\begin{aligned} E = {} & K_A^{(i)} \sin^2 \varphi_i + M_{sat.}^{(i)} B_{app} \cos \varphi_i \\ & + K_A^{(j)} \sin^2 \varphi_j + M_{sat.}^{(j)} B_{app} \cos \varphi_j + E_{ex} \end{aligned} \tag{6.05}$$

The different parameters possess their usual meaning and refer to the corresponding magnetic phase by the index (*i*) and (*j*).

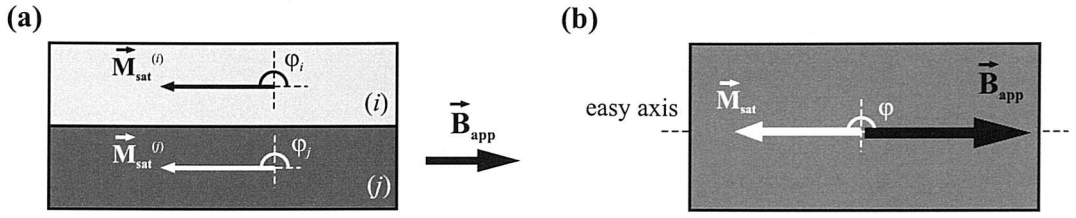

Figure 6.2.a Sketch of the magnetisation arrangement of a magnetic 2-phase system: (*i*) and (*j*) are 2 single domain particles of magnetisation $M_{sat}^{(i)}$ and $M_{sat}^{(j)}$ respectively. **b)** The system on the left is alternative -ly equivalent to a single domain particle with an easy axis which results from the combinaison of the uniaxial anisotropy of (*i*) and of (*j*)

The strong exchange interaction forces the magnetisations $\vec{M}_{sat}^{(i)}$ and $\vec{M}_{sat}^{(j)}$ to point in the same direction. Therefore, $\varphi_i = \varphi_j = \varphi$. In addition, because the exchange energy is a parameter independent of the applied field, it plays no role in the energy minimisation: $\partial E_{ex}/\partial B_{app} = 0$. Consequently, there is competition only between the anisotropy energy of the particles and the effect of the applied field. Therefore, Eq. 6.05 becomes:

$$E = \left(K_A^i + K_A^j\right)\sin^2\varphi + \left(M_{sat.}^{(i)} + M_{sat.}^{(j)}\right)B_{app}\cos\varphi \qquad (6.06)$$

By writing: $M_{sat.} = \left(M_{sat.}^{(i)} + M_{sat.}^{(j)}\right)$, and $K_A = \left(K_A^{(i)} + K_A^{(j)}\right)$, it can be observed that the mathematics for the exchange coupled 2-phase system are identical with those of the single-phase system derived in the previous section. Thus the new coercive field is given by:

$$B_C = 2\frac{K_A}{M_{sat.}} = 2\frac{K_A^{(i)} + K_A^{(j)}}{M_{sat}^{(i)} + M_{sat}^{(j)}} \qquad (6.07)$$

By assuming that each layer of a multilayer structure behaves as a magnetic single domain, it is easy to generalise Eq. 6.07 for a repeated multilayer film:

$$B_C = 2\frac{\left(K_i t_i + K_j t_j\right)}{\left(M_i t_i + M_j t_j\right)} \qquad (6.08)$$

where K_α, M_α and t_α refer respectively to the anisotropy, the net magnetic moment and the thickness of the magnetic phase α, with $\alpha = i, j$. Finally, it is remarked that Eq. 6.08 also holds for a 2-phase alloy film.

Note that for an anti-ferromagnetically coupled hetero-phase system at magnetic compensation, *i.e.* $M_i t_i + M_j t_j = 0$, the coercive field B_C tends to infinity. Thus, composite could be used as a permanent pinning layer in a more complex structure. However, the disadvantage is the zero net magnetisation exhibited.

6.3 The coercivity of MBE grown $Tb_{(1-x)}$ Dy_x Fe_2 alloys

The Laves phase $TbFe_2$ bulk compound is well known for its giant magnetostriction at room temperature. The largest internal distorsion occurs along the axes of easy magnetisation {111}: $\lambda_{111} = 2450$ ppm. However, it displays also a large negative magnetic anisotropy $K_1^{TbFe_2} = -7.6 \times 10^7$ erg.cm^{-3}, which renders it unsuitable for practical application. On the other hand, at room temperature the $DyFe_2$ bulk material shows a rather small magnetostriction $\lambda_{001} = 4 \times 10^{-6}$ ppm, and a large positive magnetic anisotropy $K_1^{DyFe_2} = +2.1 \times 10^7$ erg.cm^{-3}. [6]

In 1980, A. E. Clark *et al.* showed that by combining these two components in a specific ratio, it is possible to tailor the ternary alloy $Tb_{(1-x)}Dy_xFe_2$ to minimise the magnetic anisotropy energy yet maintain the large magnetostriction. It was found that the anisotropy compensation can be realised for the magic ratio $x \sim 0.73$ [7]:

$$0.73 \times K_1^{DyFe_2} + 0.27 \times K_1^{TbFe_2} \sim 0$$

The resulting material ($Tb_{0.73}Dy_{0.27}Fe_2$), called Terfenol-D, is characterised by a high magnetostriction to anisotropy ratio ~650 at room temperature and a large Curie temperature. Nowaday, it is widely used in micromechanical devices like microactuators, microsensors, and micromachines [8].

The preparation of bulk Terfenol is plagued with the problem of reducing the concentration of *Widemanstatten* platelets (RE-Fe_3 precipitates), and crystal twinning [8]. RE-Fe_2 grown by MBE are of high quality ('cleaner'). Moreover, the crystalline nature of the system should improve the magnetostriction properties.
In the following section, the magnetic measurements on epitaxial Terfenol-type films are reported. In particular, room temperature coercivity and easy axis of magnetisation has been determined for $1 \geq x > 0$.

6.3.1 Experimental results

The films were epitaxially grown on a epi-prepared sapphire substrate following the procedure detailed in chapter 4. The co-deposition of the $TbFe_2$ and $DyFe_2$ components, for a total sample thickness of 4000 Å, was operated on a $(11\bar{2}0)$ sapphire substrate. The bulk lattice parameters for $DyFe_2$ and $TbFe_2$ are almost equal: $a_{DyFe_2} = 7.325$ Å and $a_{TbFe_2} = 7.347$ Å [9]. Hence, the lattice mismatch is expected to be minimal, and to induce a minor shear strain.
The magnetic measurements reported in this section, were conducted at room temperature with the magnetic field applied in (110) the growth plane of the samples. Two different magnetometers were used to characterise the properties of the specimen: an *Oxford Instruments Aerosonic 3001* Vibrating Sample Magnetometer (VSM) and a Vector VSM (VVSM). With the VSM, measurements of the hysteresis loops were performed in applied fields $\vec{B}_{app}$ up to 4 T directed along 3 different crystallographic directions (Fig. 6.3):

- $[\bar{1}\,1\,\bar{1}]$, an easy axis of $TbFe_2$ bulk material at room temperature [6],
- [001], a direction of easy magnetisation of $DyFe_2$ bulk at 290 K [6], and
- $[\bar{1}\,10]$ is believed to be close to the easy axis of the epitaxial Terfenol-D material [10].

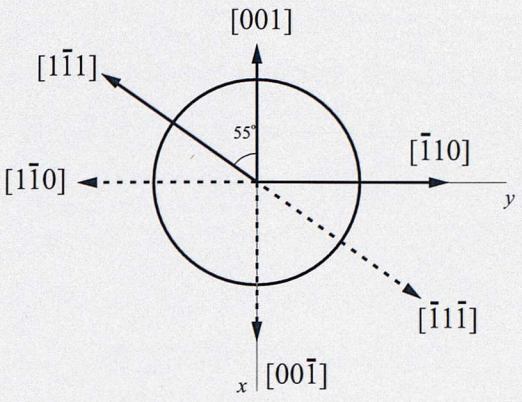

Figure 6.3 The in-plane crystallographic directions of the (110) MBE grown $Tb_{(1-x)}Dy_xFe_2$ alloy films. The growth direction [110] (*i.e.* the *z* direction) is pointing out of the plane of the page.

Typical magnetisation curves of $Tb_{(1-x)}Dy_xFe_2$ alloy films, for $x = 0.2$, can be seen in Fig. 6.4.a. Fig. 6.4.b shows the change of the coercivity of the sample when the field is directed in various sample in-plane directions.

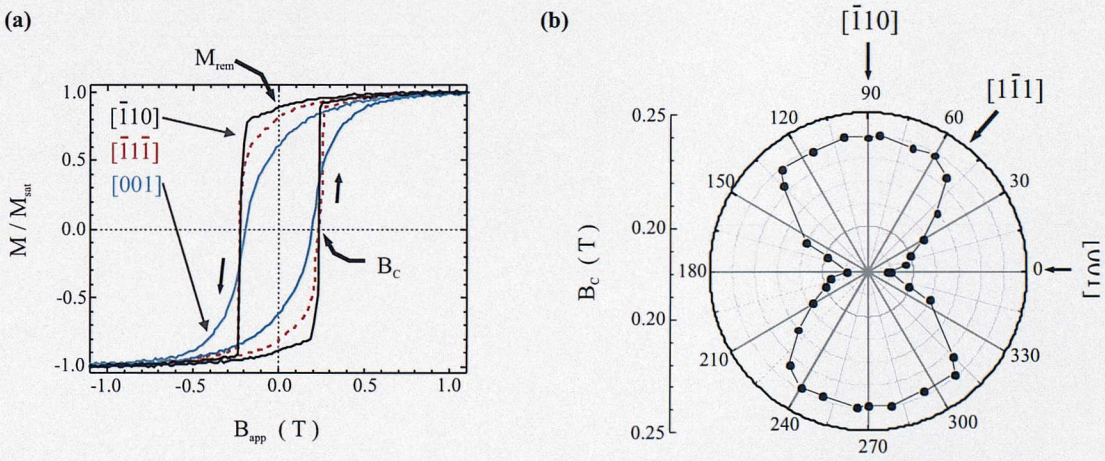

Figure 6.4 Room temperature magnetisation data of a 4000 Å $Tb_{0.8}Dy_{0.2}Fe_2$ alloy film epitaxially grown.
a) Hysteresis loops. B_C is the coercive field and M_{rem} is the remanent magnetisation field.
b) Polar plot of B_C for diverse direction of the applied magnetic (bullets)

The single crystal $Tb_{0.8}Dy_{0.2}Fe_2$ alloy film behaves as an homogeneous system, with a two-fold symmetry of the anisotropy, characteristic of a uniaxial magnetic material. The minimum in coercivity occurs when the magnetic field is applied along the direction [001]. In that geometry, the hysteresis loop is slewed, and a field of 1.2 T, which is much larger than the coercive field $B_C^{[001]} = 0.195$ T (magnetic field along the [001] axis), is needed to magnetically saturate the film. Similar magnetic behaviour was observed for the other films of the sample series. It may be concluded therefore that the [001] axis is a hard axis of magnetisation for the $Tb_{(1-x)}Dy_xFe_2$ alloy films.

Unlike the direction of minimum coercivity which is well localised, it is more difficult to determine that of maximum coercivity. The hysteresis loops of the sample $Tb_{0.8}Dy_{0.2}Fe_2$ show almost the same coercive field ($B_C \sim 0.23$ T) when $\vec{B}_{app}$ is applied along $[\bar{1}\,10]$ and $[\bar{1}\,1\,\bar{1}]$ axis (Fig. 6.4.a). These two directions are 35° away to one another (Fig. 6.4.b). The ratio M_{rem}/M_{sat}, where M_{rem} is the remanent magnetisation (the magnetisation of the sample when $B_{app} = 0$) and M_{sat} is the magnetisation of saturation, is another parameter which can be used to determine the easy axis. Indeed, it is expected that M_{rem}/M_{sat} is maximum when the magnetic field is applied close to the easy axis. From Fig. 6.4.a, it is found that $M_{rem}/M_{sat} = 0.92$ and $M_{rem}/M_{sat} = 0.75$ when $\vec{B}_{app}$ towards $[\bar{1}\,10]$ and $\vec{B}_{app}$ towards $[\bar{1}\,1\,\bar{1}]$, respectively. That result undeniably shows that the easy axis is closer to $[\bar{1}\,10]$ than it is to $[\bar{1}\,1\,\bar{1}]$.

Still, it is clear from the shape of the M-B_{app} loop at 0 T that the easy axis is not in the plane of the film. Assume that such a material is magnetically saturated by application of a very large film in-plane magnetic field. Upon removal of the field, the net magnetic moment of the system will relax back, by rotation to its particular easy axis, which can be out of the plane. This yields a value of the remanent magnetisation M_{rem} that is rather less than the saturation magnetisation M_{sat}. Within the approximation of coherent rotation of the magnetisation, the remanent magnetisation can be written:

$$M_{rem} = M_{sat} \cos\theta \qquad (6.09)$$

where θ is the angle between the easy axis and the applied field. The quantity $\cos\theta = M_{rem}/M_{sat}$ is called the reduced remanence [1].

From the experimental data, $M_{rem}/M_{sat} = 0.92$, and Eq. 6.09, it is found that the easy axis of the epitaxial $Tb_{0.8}Dy_{0.2}Fe_2$ film points $23 \pm 8°$ out of the plane of the film.

For all epitaxially grown $Tb_{(1-x)}Dy_xFe_2$ thin films, the ratio M_{rem}/M_{sat} was the largest for the field applied along the $[\bar{1}\,10]$ direction. In addition, the fact that the reduced remanence never equals unity allows to conclude that for the room temperature easy magnetisation axis of the alloys is close to $[\bar{1}\,10]$, but out of the plane of the film.

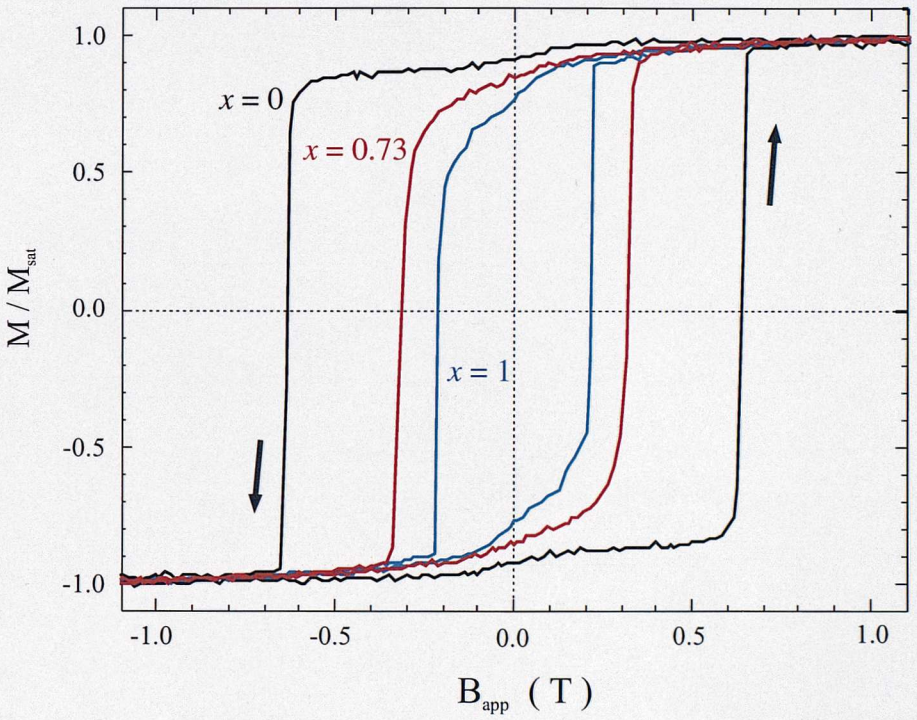

Figure 6.5 Room temperature hysteresis curves of a series of epitaxially grown terfenol-type film $Tb_{(1-x)}Dy_xFe_2$: $DyFe_2$, $Tb_{0.27}Dy_{0.73}Fe_2$, and $TbFe_2$. All the films are 4000 Å thick. The field was applied along $[\bar{1}\,10]$.

The magnetic hysteresis loops for 4 selected alloy films: $x = 0$ ($TbFe_2$), $x = 0.73$ (Terfenol-D) and $x = 1$ ($DyFe_2$) can be seen shown in Fig. 6.5. These loops were obtained with $\vec{B}_{app}$ parallel to the $[\bar{1}\,10]$ crystallographic direction.

A comparison of the M-B_{app} loops shows that the coercivity B_C ($DyFe_2$) = 0.22 T of the $DyFe_2$ epitaxial film is about 3 times smaller than the coercivity B_C ($TbFe_2$) = 0.63 T of the $TbFe_2$ film. The hysteresis curve of the latter is also squarer. It shows a high reduced remanence: $M_{rem}/M_{sat} \sim 1$, whilst for $DyFe_2$ it is found $M_{rem}/M_{sat} \sim 0.8$.

Fig. 6.5 also shows that the coercivity of the epitaxial $Tb_{(1-x)}Dy_xFe_2$ films increases with increasing relative concentration x of the $DyFe_2$ component. In addition, the shape of the hysteresis curves change: it becomes squarer with decreasing x, and the reduced remanence M_{rem}/M_{sat} tends to unity. The $Tb_{0.27}Dy_{0.73}Fe_2$ alloy, the so-called Terfenol-D, presents a coercive field of B_C = 0.36 T. Thus unlike the corresponding bulk material, the epitaxial Terfenol-D does not exhibit magnetic anisotropy compensation.

6.3.2 Discussion and theory

From the magnetisation curves presented in the previous section, it was found that the easy magnetisation direction for epitaxially grown $Tb_{(1-x)}Dy_xFe_2$ alloy film ($0 \leq x \leq 1$) is close to [$\bar{1}$ 10] at room temperature. Moreover, the easy axis of $Tb_{0.27}Dy_{0.73}Fe_2$ film lies ~ 28° out of the film plane. This differs from the Terfenol bulk case for which {111} is the easy axis [7]. The reason for this difference lies in the epitaxial strain, induced at the end of the growth of the Laves phase on the heated sapphire substrate. More details about the epitaxial built-in strain in RE-Fe_2 based films can be found in chapter 5.

Mougin *et al.* have measured the evolution of the crystallographic parameters $a_{(220)}$ and $a_{(2\bar{2}0)}$ for $Tb_{0.3}Dy_{0.7}Fe_2$ (110) films as a function of the temperature in the range 10 - 300 K. Their results can be seen in Fig. 6.6, where $a_{(220)} = a_\perp$ is the appropriate lattice parameter perpendicular to the sample plane, and $a_{(2\bar{2}0)} = a_\parallel$ is the lattice parameter parallel to the sample plane [10].

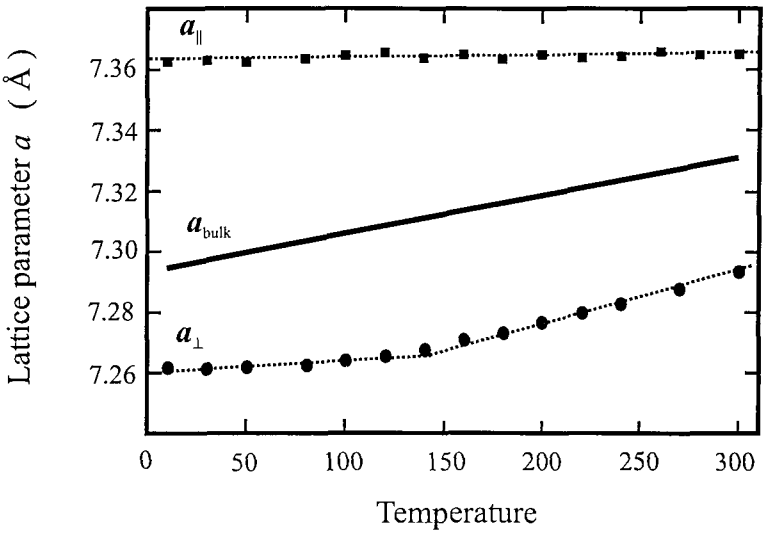

Figure 6.6 Epitaxial strain in $Tb_{0.7}Dy_{0.3}Fe_2$ (110) thin film.
Thermal evolution of the crystallographic parameters $a_{\parallel}$, $a_{\perp}$ in epitaxial form of the Terfenol-D and a_{bulk}. Those parameters were deduced from neutron diffraction measurements [10]. The dotted lines are guides to the eyes.

The lattice parameter parallel to the sample plane $a_{\parallel}$ is practically temperature independent. The film is clamped to the sapphire substrate, and therefore a change in $a_{\parallel}$ is determined solely by the sapphire substrate, as a function of the temperature. By way of contrast, the lattice parameter perpendicular to the sample plane is free to expand along the growth direction. Note that for T > 150K, $a_{\perp}$(T) follows the same linear slope than a_{bulk} and for T < 150K, $a_{\perp}$(T) is practically constant. (a_{bulk} is the lattice parameter of the $Tb_{0.3}Dy_{0.7}Fe_2$ bulk material). Finally, Mougin *et al.* conclude that the $Tb_{0.3}Dy_{0.7}Fe_2$ MBE film is subject to a shear strain $\varepsilon_{xy} = (a_{\perp} - a_{\parallel})/2a$ (a is the average parameter) reaching a value of -0.55 % at room temperature.

The direction of easy magnetisation is related to the sign and value of both K_1 and K_2 anisotropy coefficients. In bulk Terfenol-D, $K_1 = -6.6\times10^6$ erg.cm^{-3} is negative and $K_2 = 3.4\times10^6$ erg.cm^{-3} is positive. Consequently, the easy axis lies along [111] or equivalent directions [7]. The epitaxial strain in MBE grown Terfenol film, results in two additional energy terms: magneto-elastic and elastic energy, with $b_2 = -2.37\times10^9$ erg.cm^{-3} (ref. chapter 5). The analysis performed by Ref. [10], using

energy minimisation, established that [$\bar{1}$ 10] is the easy axis for epitaxial Terfenol-D at room temperature. This is in agreement with the experimental result that shows that the epitaxial $Tb_{(1-x)}Dy_xFe_2$ films are more easily magnetised along [$\bar{1}$ 10].

As discussed previously, at room temperature, the bulk Terfenol-D material is characterised by compensation of the anisotropy between the negative anisotropy of the $TbFe_2$ compound and the positive anisotropy of the $DyFe_2$ component. In epitaxial form of the Terfenol-D, the magneto-crystalline anisotropy of $TbFe_2$ vanishes that of $DyFe_2$. However, the strain term remains and leads to a non-zero net anisotropy.

In Fig. 6.7, the coercivity B_C of the epitaxial $Tb_{(1-x)}Dy_xFe_2$ films versus the relative concentration x ($1 \geq x \geq 0$) is shown (bullets). The coercivity fall almost on a straight line, with a maximum coercivity for $TbFe_2$ film ($B_C = 0.64$ T) and the smallest B_C for $DyFe_2$ ($B_C = 0.22$ T). Given that the easy axis of magnetisation in the $Tb_{(1-x)}Dy_xFe_2$ series lies close to a common [$\bar{1}$ 10] axis, the evolution of B_C versus x can be described by the modified form of the Stoner and Wohlfarth (S-W) given in the section 6.2:

$$B_C = 2\frac{(1-x)K_{TbFe_2} + xK_{DyFe_2}}{(1-x)M_{TbFe_2} + xM_{DyFe_2}} \qquad (6.10)$$

K_{TbFe_2} and K_{DyFe_2} are the uniaxial anisotropy constant for $TbFe_2$ and $DyFe_2$ respectively. The magnetic moments M_{TbFe_2} and M_{DyFe_2} were determined experimentally from the hysteresis loops of the components: $M_{TbFe_2} = 2.99\ \mu_B$ / f.u and $M_{DyFe_2} = 4.22\ \mu_B$ / f.u.

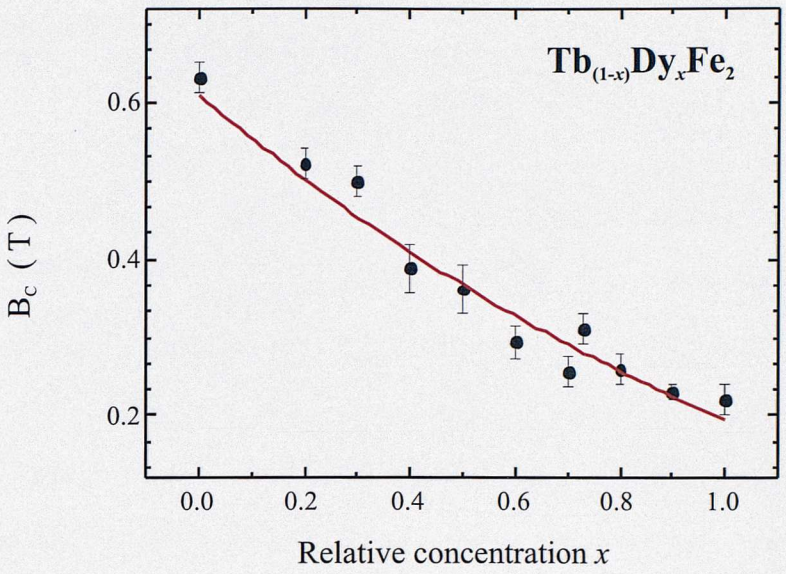

Figure 6.7 The coercivity B_C of epitaxial $Tb_{(1-x)}Dy_xFe_2$ film as a function of the $DyFe_2$ concentration x, at room temperature. The solid line is the theoretical prediction based on Eq. 6.08.

A least squares fit to the experimental data, based on Eq. 6.08 is included in Fig. 6.7. From this fit, the anisotropy parameters are found to be as followed: $K_{TbFe_2} = 0.91 \pm 0.07$ Kelvin per ion, and $K_{DyFe_2} = 0.41 \pm 0.04$ Kelvin per ion. This is in good agreement with the values determined experimentally, using the equation $B_C = 2K/M$.

In conlusion, the S-W model, based on the principle of coherent rotation of the magnetisation, can be used to provide a simple description of the coercive field B_C of the epitaxial $Tb_{(1-x)}Dy_xFe_2$ compound as a function of x. The results suggest that the strain term $b_2\alpha_x\alpha_y\varepsilon_{xy}$ dominates, and the single-ion terms K_1 and K_2 play little role.

It will also be noticed that the majority of the points fall slightly below the S-W prediction. This difficulty may be due to the 'out of plane' magnetic components, alluded to earlier.

6.4 Engineering coercivity of $DyFe_2$ – YFe_2 multilayers

MBE films of $DyFe_2$ can be viewed as an archetypal highly anisotropic ferromagnetic material with a net magnetic moment m_{DyFe_2} = 7±0.3 μ_B / f.u and B_C = 3 T at 10 K for the applied field $\vec{B}_{app}$ along the easy axis [001]. YFe_2 can be considered as a soft ferromagnet, as a result of its low coercive field: B_C = 0.03 T. At 10 K, its net magnetic moment is m_{YFe_2} = 3±0.1 μ_B / f.u. In general, it is assumed that the magnetisation of the YFe_2 compound comes mainly from the iron moment, while the magnetic contribution of the Y^{3+} ions is negligible.

On combining the two Laves phase $DyFe_2$ and YFe_2 into a multilayer structure, a 'ferrimagnet' is obtained (Fig. 6.8). Its direction of easy magnetisation is controlled primarily by the $DyFe_2$ layer. The resultant spin configuration is the result of the strong AFM coupling between $DyFe_2$ and YFe_2 through the positive exchange interaction between the iron magnetic moments and through the negative exchange coupling between iron and Dysprosium moments in the $DyFe_2$ layers [9].

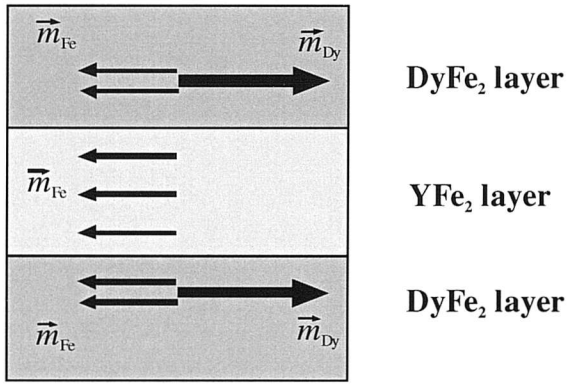

Figure 6.8 Spin arrangements in $DyFe_2$ – YFe_2 multilayer system when the field is decreased from high positive value to 0 T.

6.4.1 Experimental results

The $DyFe_2$ - YFe_2 multilayer systems studied in this section are high quality single crystal superlattice films grown by MBE techniques. Since the bulk lattice parameters for $DyFe_2$ and YFe_2 are 7.325Å and 7.363Å respectively, the mismatch at the superlattice interfaces is expected to be small of the order of 0.5%.

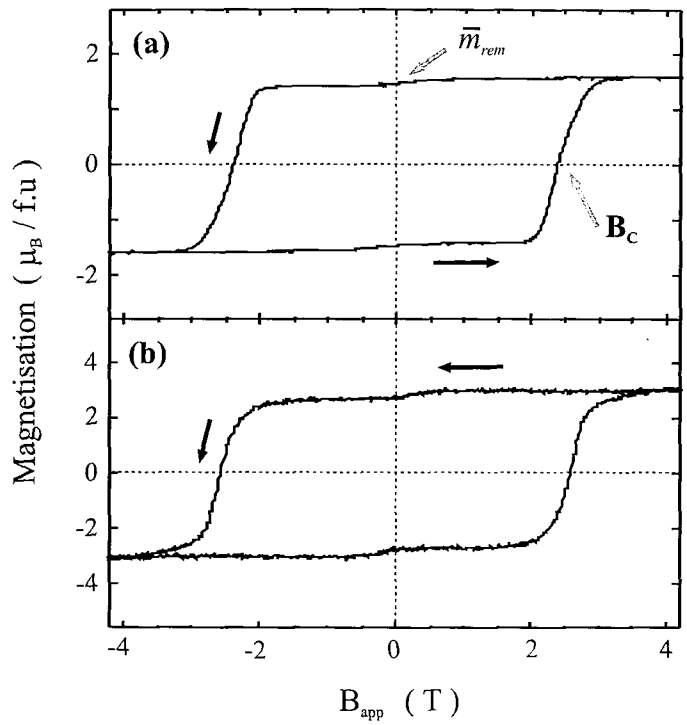

Figure 6.9 Magnetometry measurements performed at 120 K with $\vec{B}_{app}$ along the [001] direction. The remanent magnetisation $\bar{m}_{rem}$ and the coercive field B_C are indicated.
a) 4000 Å $Dy_{0.5}Y_{0.5}Fe_2$ alloy film grown epitaxially.
b) Epitaxial [50Å $DyFe_2$ - 50Å YFe_2]×40 multilayer film.

A series of epitaxially grown multilayer films [x $DyFe_2$ - (100-x) YFe_2]×40, with x = 80 Å, 60 Å, 50 Å, and 45 Å (40 is the number of repeat of the bilayer) have been investigated, using a VSM, at temperatures from 10 K to 300 K. The magnetic field of up to 12 T was applied along [001] axis, which is the easy axis of the MBE (110) $DyFe_2$ film at low temperatures [11].

A typical in-plane magnetisation curve at 120 K for the epitaxial film [50Å $DyFe_2$ - 50Å YFe_2]×40 is shown in Fig. 6.9.b. For comparison, the hysteresis loop for the alloy $Dy_{0.5}Y_{0.5}Fe_2$ is also shown in Fig. 6.9.a. The samples have about the same magnetic profile, with similar coercivities and equal magnetisation at 0 T. The hysteresis loop of the superlattice is a simple square loop, characteristic of a hard magnet, corroborating that [001] is the easy axis. It is therefore concluded that the Dy ions dictate the easy axis of both the alloy and the superlattice. The feature of the M-B_{app} loop also indicates that the multilayer structure behaves collectively, as a coherent 'block', whose the net magnetisation aligns along the field direction. This is due to the strong Fe – Fe exchange coupling between the two phases $DyFe_2$ and YFe_2, which forces the Fe moment in the entire film to point in one direction.

The value of the remanent magnetisation $\overline{m}_{rem}$ (net magnetisation at 0 T after having magnetically saturated the sample) confirms the AFM coupling between YFe_2 and $DyFe_2$ phases:

$$\overline{m}_{rem} = x\, m_{DyFe_2} - (1-x)\, m_{YFe_2} \qquad (6.11)$$

$m_{YFe_2} = 2.9\ \mu_B$ / f.u and $m_{DyFe_2} = 6.2\ \mu_B$ / f.u are the magnetisation of saturation of the components at 120 K (cf. chapter 5). The negative sign in Eq. 6.11 refers to the anti-parallel alignment of the YFe_2 and $DyFe_2$ magnetic moment. The theoretical value given by Eq. 6.11: $\overline{m}_{rem} = 1.65\ \mu_B$ / f.u, agrees reasonably well with the experimental result $\overline{m}_{rem} = 1.55\ \mu_B$ / f.u.

The hysteresis curves collected from the multilayer thin films [x $DyFe_2$ - (100-x) YFe_2]×40, with x = 80 Å, 60 Å, and 45 Å are shown in Fig. 6.10. It may be noticed that the effect of an increasing proportion of the soft component leads to the reduction of the remanent magnetisation $\overline{m}_{rem}$, as it is expected, and to the change in curvature of the M-B_{app} loop (less and less square).

Fig. 6.10 also clearly shows that the coercivity of the multilayer films increases as the $DyFe_2$ layer thickness is reduced. The sample [45Å $DyFe_2$ - 55Å YFe_2]×40 possesses a very high coercivity of 10 T, compared to the 3 T coercive field in $DyFe_2$ film, at 10 K. Actually, the coercivity of the $DyFe_2$ film is lower than any of the superlattice samples.

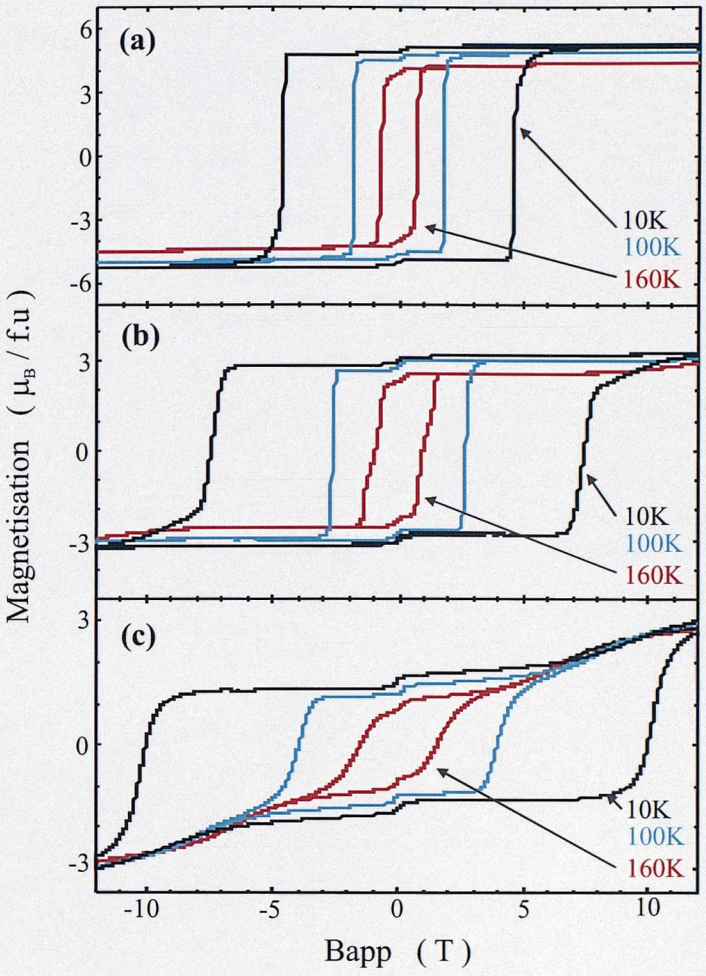

Figure 6.10 A selection of the magnetisation curves for the superlattice samples [x $DyFe_2$ - (100-x) YFe_2]×40. The magnetic field B_{app} is applied along [001].
a) x = 80 Å **b)** x = 60 Å **c)** x = 45 Å

6.4.2 Discussion

The magnetometry measurements suggest that it should be possible to engineer a desired coercivity B_C of the multilayer structures $DyFe_2 - YFe_2$, by adjusting the relative thickness of the magnetic phases. Indeed, it is found that the coercivity B_C decreases as a function of the $DyFe_2$ layer thickness x. The results displayed in Fig. 6.11 show the complete dependence of B_C as a function of $DyFe_2$ thickness x, at 10 K.

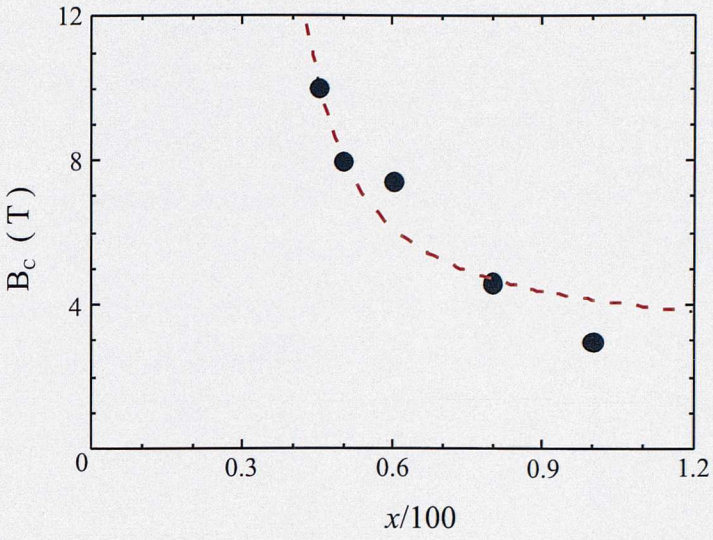

Figure 6.11 The experimentally determined easy axis coercivity B_C at 10 K, as a function of x/100 (bullets). The dashed line is a theoretical plot based on Eq. 6.12.

In what follows, the Stoner and Wohlfarth model in modified form is employed to describe the magnetic reversal mechanism in the AFM coupled multilayer structure. In this analysis, it is assumed that its magneto-crystalline anisotropy is controlled by the $DyFe_2$ layer. The anisotropy associated with the soft phase YFe_2 will be ignored. Therefore:

$$B_C = 2\,\frac{K_h x}{m_h x - m_s(1-x)} \tag{6.12}$$

where the parameters of the magnetically hard and soft layers are indexed by h and s respectively. The magnetisation of the $DyFe_2$ and YFe_2 layers have been set to: $m_h = 7\ \mu_B$ / f.u and $m_s = 3\ \mu_B$ / f.u respectively. The anisotropy constant K_h will be determined by fitting Eq. 6.12 to the experimental data, using a least square method. A comparison of the experimental data and the theoretical predictions shows that the measured coercivity is in semi-quantitative agreement with the simple theoretical expression. From the least square fit, it is found $K_h = 9 \pm 3$ Kelvin per ion.

Thus it would appear that the reversal mechanism in the AFM coupled multilayers [xÅ $DyFe_2$ - (1-x)Å YFe_2]×40 can be partially explained by the model of coherent rotation of the net magnetisation. Nevertheless, it must be acknowledged that Eq. 6.12 is simplistic in that it does not take into account any energy expended in

creating magnetic exchange springs. Indeed, the theory is based on the assumption that the two coupled phases behave as magnetic 'blocks' with uniform magnetic moment. In the case of the sample [45Å $DyFe_2$ - 55Å YFe_2]×40, the large reversible increase of the magnetisation at high field is typical of the formation of magnetic exchange springs (Fig. 6.10.c). In practice, it is likely that exchange springs, originating primarily in the soft layers, will penetrate into neighbouring $DyFe_2$ layers. Furthermore, for small thickness of the hard phase, this feature is likely to become more pronounced, and to affect the reversal mechanism. The effect of magnetic exchange springs on the coercivity will be discussed in more details in chapter 8.

Although the theory of coherent rotation gives a reasonably good description of the coercivity in $DyFe_2$ - YFe_2 multilayers, it must be recognized that in real magnetic materials, this mechanism is not the major cause of the reversal process. Indeed, the coercive field B_C in epitaxial thin films is dominated by the pinning of domain walls by imperfections [12, 13]. In this model, reversed domains nucleate and suddenly propagate through the lattice. In this model, precipitates, inclusions, surface roughness and other defects can lower the wall energy at particular positions in the material, effectively pinning its motion through the defect. As an external field is applied, a pressure is exerted on the wall tending to accelerate it. The presence of the pinning defects leads to an irregular DW motion consisting of a series of Barkhausen jumps as the wall skips from defect to defect. The DW bow out between individual pinning sites and escape when the applied magnetic field, aided by thermal activation, reaches a critical value. Gaunt *et al.* [14, 15] have given a statistical model of the temperature dependence of the coercivity. The model, based on the interaction between DW's and pinning sites, makes a distinction between 'strong' and 'weak' DW pinning. For weak DW pinning sites (WDWP), thermal excitation leads to a linear decrease of the coercive field with temperature. On the other hand, in the limit of strong DW pinning (SDWP), the domain walls are strongly pinned by discrete individual obstacles, and 'bow out' before breaking away. In this case, the coercive field B_C varies with temperature as $T^{2/3}$:

$$B_C = B_C^0\left(1 - C\,T^{2/3}\right) \tag{6.13}$$

with $C = \left(\frac{75 k_B}{\delta_{DW} f} \right)^{2/3}$, where δ_{DW} is the domain wall width, f is the maximum restoring force a single pin can exert on a DW segment, k_B is the Boltzmann constant. B_C^0 is the coercive field without thermal excitation, *i.e.* at 0 K.

So, measurements of the temperature variation of the coercivity can be used to obtain insight into the properties of the pinning centers. In Fig. 6.12, the temperature dependence of the coercivity B_C for the samples [60Å $DyFe_2$ – 40Å YFe_2]×40 and [80Å $DyFe_2$ - 20Å YFe_2]×40 can be seen. For the two specimens, B_C falls off rapidly with temperature, but flattens out at room temperature. The results for temperatures above 150 K will not be included in the analysis presented here, because of the re-orientation of the easy axis, reflected by the clear slope change of B_C (T) at 150 K.

A least squares fit of the experimental results, using Eq. 6.13 for a SDWP model, gives the parameters B_C^0 and C. For the sample [60Å $DyFe_2$ - 40Å YFe_2]×40, it is found: $B_C^0 = 8.9 \pm 0.2$ T and $C = 3180 \pm 5 \times 10^{-5}$ $K^{-2/3}$.

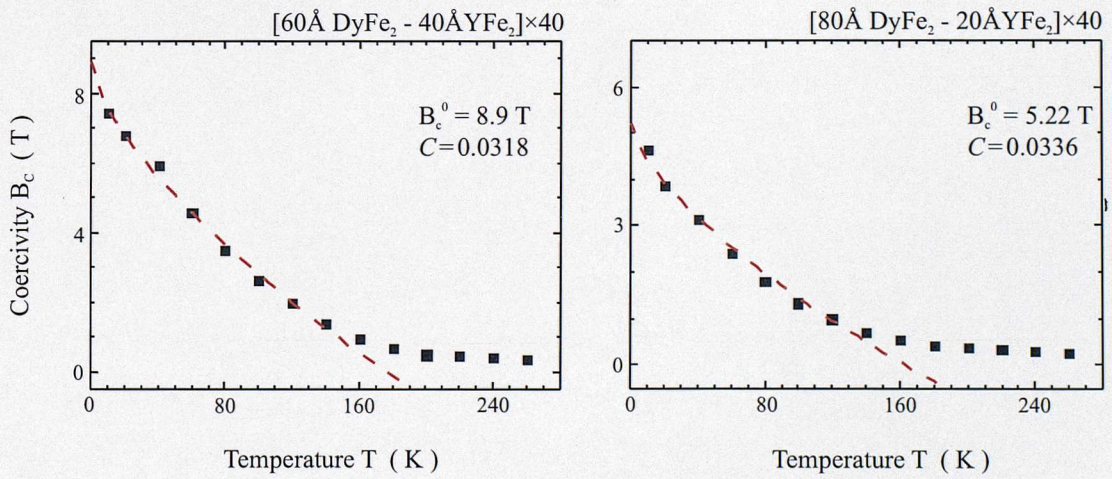

Figure 6.12 Temperature dependence of the coercivity B_C (bullets) for two superlattices. The temperature range covered is 10 K up to 260 K. The dashed lines represent the best fits of the data using the SDWP theory for temperatures below 150 K. The parameters B_C^0 and C determined from the fit are precised.

Using the estimation of the domain wall width given in Appendix ($\delta_{DW} \approx 25$Å), a restoring force f of around 7.3×10^{-6} dyn is determined. As expected, no significant change of C and consequently of f was found when the layer thickness of the hard and soft phases was changed. The results show that the reversal of the magnetisation in the anti-ferromagnetically coupled $DyFe_2$-YFe_2 takes place by strong domain-wall pinning resulting from the interactions of the moving domain wall and discrete individual pins.

Epitaxially grown films are thought as intrinsequely ordered structures. However, in Ref. [16], it has been underlined that in the $DyFe_2$ YFe_2 (110) epitaxially grown multilayers, the first 500 Å of the film is made up of islands elongated along [$\bar{1}$ 10], which is perpendicular to the low temperature easy axis [001]. It is easily understandable that those peculiar microstructures can have a detrimental effect on the motion of the DW through the sample. Also, the epitaxial strain induced by the sapphire substrate upon the Laves phase components and the lattice parameter mismatch triggers off localised lattice distorsions may add other pinning sites.

6.5 Conclusions

Epitaxially grown [x $DyFe_2$ – (1-x) YFe_2]×40 multilayer (x is the thickness of the hard phase) and $Tb_{(1-x)}Dy_xFe_2$ alloy (x is the relative concentration of the $DyFe_2$ component) films have been magnetically characterised. Both structures were found to behave as single magnetic entities, as a result to the strong exchange interaction between Fe magnetic moments. In particular magnetometry measurements on $DyFe_2$ - YFe_2 superlattices attested the strong exchange coupling between the 2 phases, and the peculiar spin distribution in the film, which is similar to a giant ferrimagnet.

By adjusting the microstructure of the films, it has been possible to engineer their coercive field B_C in digital manner. However, in the case of $Tb_{(1-x)}Dy_xFe_2$ alloy films, it was not found possible to tailor a film exhibiting anisotropy compensation. Indeed, unlike the bulk material, no minimum in coercivity was found for the epitaxial

Terfenol-type materials. The underlying reason for this difference is attributed to the presence of a magnetic-elastic (MEL) term in the MBE grown films, which favours the [$\bar{1}$ 10] direction as easy axis at room temperature. The MEL originates from the strain induced by the difference of thermal expansion exerted by the sapphire substrate upon the Laves phase compounds after the growth. The hysteresis loops also suggest that the easy axis might lie out of the sample plane.

The Stoner and Wohlfarth model was used to obtain an estimation of B_C as a function of x. The theory, which is based on the principle that magnetisation reversal takes place by coherent rotation of the magnetic moment, was initially formulated for a single phase system. It has been used to describe successfully the coercivity in ferromagnetically coupled alloys of hard and soft magnets [2]. In this work, a generalised form of the model is applied to two particular magnetic structures:

- the highly magnetostrictive epitaxial $Tb_{(1-x)}Dy_xFe_2$ alloy films, which is subject to the significant strain of the substrate, and also
- the anti-ferromagnetically coupled [x $DyFe_2$ – (1-x) YFe_2]×40 superlattices,

and, it proved to be reasonably successful in predicting their coercivity.

Although the agreement between the experimental results and the calculation is effective, it must be kept in mind that it is a simple model, which cannot be used to describe the magnetisation reversal mechanism in real magnets. Moreover, it is known from the Brown's paradox that the coercive field lies well below the theoretically calculated ideal coercive field [17]. It is generally thought that the coherent rotation law may be observed only in the case of systems smaller than the exchange length and domain wall, in which non-uniform configuration are magnetically unfavourable, *i.e.* single domain particles. However, in real ferromagnetic materials, the magnetisation configuration cannot be assumed to be uniform, and the reversal mechanism proceeds by nucleation and propagation of domain walls. This was highlighted by analyzing the temperature evolution of the coercivity of the Laves phase multilayer structure. It was shown that a model of strong domain-wall pinning describes well that dependence, and enables then to identify the mechanism responsible for the magnetisation reversal. A quantitative study of the strength of the pinning inhomogeneities was given.

References

[1] E. C. Stoner and E. P. Wohlfarth, *Phil. Trans. R. Soc.* **240**: 599-642 (1948)

[2] E. E. Fullerton *et al.*, *Phys. Rev. B* **58** (18): 12193 (1998)
E. E. Fullerton *et al.*, *J. Magn. Magn. Mater.* **200**: 392 (1999)
J. M. D. Coey, *Phys. Scr. T* **49**: 315 (1993)
I. A. Al-Omari *et al.*, *Phys. Rev. B* **52**: 3441 (1995)
M. Shindo *et al.*, *J. Magn. Magn. Mater.* **161**, L1 (1996)

[3] D.S. Rodbell and C.P. Bean, *Phys. Rev. B* **103** (4): 886 (1956)

[4] L. Neel, *J. de Phys. et Radium* **5**: 18 (1994)

[5] Usually, one observes many domain configurations in FM specimen. However, if the size of a magnetic particle is decreased then there is a critical size below which the decrease in magnetostatic energy by splitting into 2 domains is less than the increase in energy due to the introduction of the domain wall. Particles that are below this critical size are known as '*single domain*' particles.

[6] A.E. Clark, *Handbook of the Physics and Chemistry of RE*, vol. 2, K. A. Gschneidner, L. Eyring (Eds.), North-Holland, Amsterdam, p. 531 (1982)

[7] A. E. Clark *et al.*, *AIP Conf. Proc.* **18**: 1015 (1974)
A. E. Clark *et al.*, *AIP Conf. Proc.* **24**: 670 (1975)

[8] D. C. Jiles, *Appl. Phys.* **27**: 1-11 (1994)

[9] K. H. J. Buschow, *Rep. Prog. Phys.* **40**: 1179-1256 (1977)
J. J. M. Franse and R. J. Radwanski, *Handbook of Magnetic Materials*, Vol. 7, edited by K. H. J. Buschow, North-Holland Amsterdam (1993)

[10] A. Mougin *et al.*, *Phys. Rev. B* **62**: 9517 (2000)

[11] V. Oderno *et al.*, *Phys. Rev. B* **54**: R17375-8 (1996)

[12] E. Kneller, *Ferromagnetismus* (Springer, Berlin, 1962)

[13] R. Skomski, and J. M. D. Coey, *Phys. Rev. B* **48**: 15812 (1993)

[14] P. Gaunt, *Philos. Mag. B* **48**: 261 (1983)

[15] P. Gaunt *et al.*, *J. App. Phys.* **59**: 4129, 12 (1986)

[16] A. Mougin *et al.*, *Appl. Phys. Lett.* **76**: 1449, 11 (2000)

[17] W. F. Brown Jr., *Micromagnetics* (Interscience, New York 1963)
A. Aharoni, *Rev. Mod. Phys.* **34**: 227 (1962)

Chapter 7

Magnetic exchange springs in $DyFe_2$ - YFe_2 multilayers

So far in this thesis, in the study of the $DyFe_2$ - YFe_2 epitaxial superlattices, we have limited the discussion to films with thin YFe_2 layers. Their magnetisation curves are characterised by square hysterestic loops similar to those of hard single-phase magnets. But, it was noted that at high magnetic fields, the samples with relative thicker YFe_2 layers, exhibited an increase of magnetisation. This additional magnetisation is due to the formation of magnetic exchange springs.

The physics of exchange springs in ferromagnetically (FM) coupled systems is well understood [1 - 3]. The interest in such materials comes from the fact they constitute a promising alternative for producing high performance permanent magnets [4, 5]. By way of contrast, exchange springs in anti-ferromagnetically (AFM) coupled superlattices has rarely been examined. In this chapter, it is proposed to look at the peculiar properties of the AFM coupled magnetic exchange springs $DyFe_2$ - YFe_2 multilayer films.

In section 7.1, the research on exchange spring coupled systems is outlined and discussed. This is followed by the magnetic characterisation of $DyFe_2$ - YFe_2 superlattices, through the study of both the field and temperature dependency of their magnetic properties. In section 7.3, it is presented and discussed the influence of nano-structural modifications on the magnetic profile of the films. Then, it is shown how magnetic exchange springs can be used to design M-B loops with specific properties. Finally, conclusions are drawn.

7.1. Review of the research on magnetic exchange springs magnets

The maximum energy product $(BH)_{max}$ is the parameter used to gauge the quality of a permanent magnet. An ideal magnet must have a large coercivity B_C, rendering it difficult to demagnetize, and a large remanence M_R. An increase in both these parameters leads to an increase of the $(BH)_{max}$.

Research into magnetic exchange springs has met a growing interest in recent years [2, 3, 6, 7], because it offers the promise of increasing $(BH)_{max}$ in permanent magnet applications [4, 5]. Heterogeneous mixtures of ferromagnetically coupled hard and soft magnetic materials, are mixed together, at the nanoscale level. In general, the hard material provides the coercivity of the composite magnet while the soft material increases the magnetisation. The magnetically hard phase, often a Rare Earth - Transition Metal (RE-TM) intermetallic compounds (like $Nd_2Fe_{14}B_1$ or $SmCo_5$), provides a high coercivity through the large crystal field anisotropy at the RE^{3+} site. On the other hand, the soft magnetic phase, a TM (like Fe, Co...), enhances the net magnetisation via the parallel alignment induced by the FM coupling with the TM elements present in the magnetic hard component. In parallel, with the desire to optimize $(BH)_{max}$, one of the motivations for the development of composite exchange springs magnets is to reduce the content of the costly and highly oxydizable RE elements.

The research has mainly been carried out using sputtered magnets, where the hard and soft phases are combined either in a granular mode or in a multilayer fashion [2, 3, 8 - 11]. The magnetic exchange springs phenomenon, which is similar for the two structures, is illustrated below in Fig. 7.1. This shows the typical hysteresis loop of a FM coupled exchange spring multilayer system. The inserts show the magnetic spin configurations around the M-B loop.

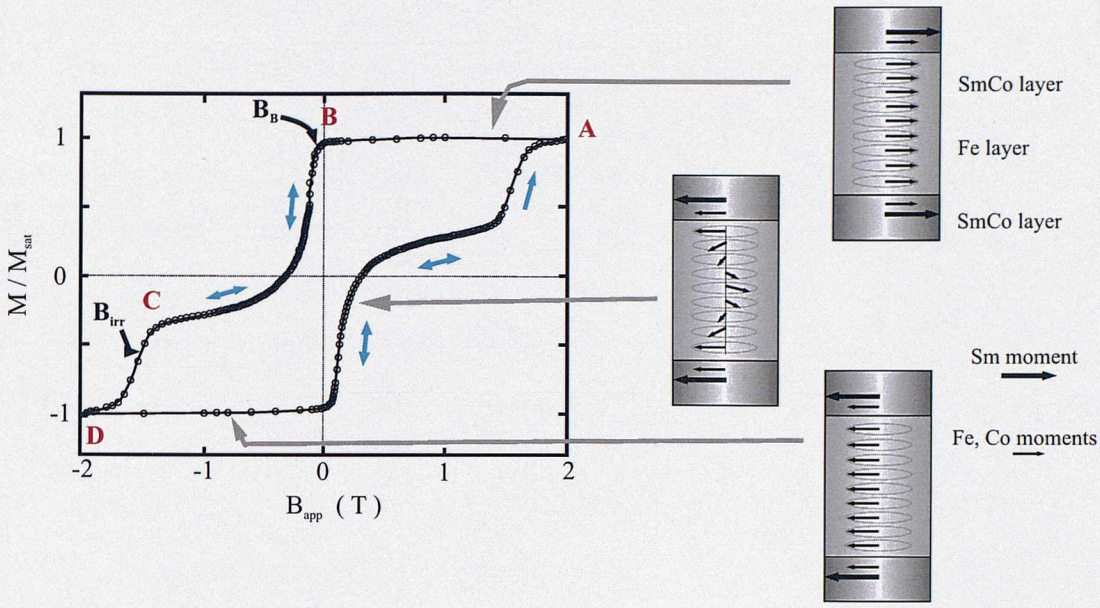

Figure 7.1 Low temperature (25K) hysteresis loop for an exchange spring coupled SmCo/Fe multilayer sample. The single and double arrows indicate respectively irreversible and reversible switching process. The related spin configurations are given in the inserts. [3]

The magnetic loop can be divided up into various region, A → B, …etc.

A → B. The magnetic moment of the hard phase SmCo is pointing to the right, pinned by the moment of the hard material. The magnetisation in the soft layer Fe also points to the right as a result of the FM coupling with the hard layer. When the field is increased in the reverse direction (B → C), the magnetic moments in the soft Fe layer tend to align with $\vec{B}_{app}$, whilst the magnetisation of the hard phase remains pointing to the right, because of its large anisotropy. As the field is increased, two 180° Bloch Domain Wall (DW) like structures develop within the soft layer. While the spins at the center of the soft phase are 'free' to follow the external field, those localised at the interfaces are pinned by the hard layer. In fact, magnetic reversal of the soft layer starts at a critical field B_B the bending field, also sometimes refered to in the literature as the nucleation field (B_N) [2]. Upon increasing the reverse field, the DW's in the soft phase exert a magnetic torque on the hard layers, because of the exchange coupling across the hard/soft interface. Note that when the magnetic field is reduced to zero, the magnetic spins of the soft material can return along the

magnetisation of the hard layer. As a result, the Bloch DW-like spin arrangement that develops at the interfaces act as recall springs. Since the magnetic moments in the soft layer are expected to rotate reversibly during the magnetisation nucleation process, such hetero-phase materials are called exchange springs by analogy with elastic motion of a mechanical spring. Then, there is a significant field range (the B-C-B part of the M-B loop) where the magnetic behaviour is perfectly reversible. As the field is increased (C $\rightarrow$ D), the DW's progressively invade the hard layer. Finally, the layer irreversibly switches to the direction of the field, now pointing to the left.

The different phase transitions in the magnetic system arise from a competition between the anisotropy energy in the hard layer, the exchange energy and, the Zeeman energy of both components. Basically, for small reverse fields, the Zeeman energy is less important and the exchange energy favours the aligned states of the magnetic moment of both the layers. A phase transition occurs when the Zeeman and the exchange energies are equally important. Upon increasing B_{app}, it becomes energetically favourable for the soft layer to develop a magnetic exchange springs.

However, to be suitable for permanent magnets application, the sytem must behave as a single hard magnetic entity *i.e* the bending field must be larger than the irreversible switching field B_{irr}.

A number of models have been formulated to describe the formation of magnetic exchange springs process in bilayer and multilayer structures. Most of them are based on a one-dimensional micro-magnetic model, where the use of the local magnetism theory (nearest neighbouring interactions) is valid. The magnetic configuration of each layer is represented by a chain of spins which runs normal to the layers, and is composed of w discrete magnetic moments. In this model, the magnetic properties are considered to be invariant inside the planes and to depend only on the plane index i. The equilibrium spin configuration for a given applied field B_{app} is determined by minimising the total magnetic energy density $dE/d\theta = 0$ and $d^2E/d\theta^2 \geq 0$, where:

$$E = -\sum_{i=1}^{w-1} \frac{A_{i,i+1}}{a^2} \cos(\theta_i - \theta_{i+1}) - \sum_{i=1}^{w} K_i \cos^2 \theta_i - \sum_{i=1}^{w} B_{app} M_i \cos(\theta_i - \theta_{B_{app}}) \quad (7.01)$$

The first, second and third term refer to the exchange energy between adjacent layers, the anisotropy energy and the Zeeman energy, respectively. The rotation angle θ_i is measured relative to the easy axis of the hard layer. The angle $\theta_{B_{app}}$ is the angle between $\vec{B}_{app}$ and the easy axis. Finally, A_i, K_i and M_i are the exchange constants, the uni-axial anisotropy constants and the magnetic moments respectively. The distance between the adjacent atomic planes is a.

The first attempt to describe analytically the magnetic exchange springs was given in 1965 by Goto *et al.* [12]. They assumed an ideal exchange coupling at the interface, rigid hard layers (infinite anisotropy constant), and soft layers with no anisotropy. Then by converting the problem into a continuous system, they demonstrated that the angular dependence of a symmetric exchange spring could be expressed in terms of a Jacobi elliptic *sn* function. Moreover an analytical expression for the bending field B_B was deduced:

$$B_B = \frac{\pi^2 A}{2(M_{sat}) t_S^2} \quad (7.02)$$

where t_S is the thickness of the soft phase.

The predictions of this model were found to be consistent with experimental studies of NiFe/NiCo bilayers [12], SmCo/NiFe [13], SmCo/CoZr [4, 14] and epitaxial $CoFe_2/(MnZn)Fe_2O_4$ exchange coupled bilayers [15].

Many of the more recent efforts to solve Eq. 7.01 employ an iterative approach similar to that outlined by Camley *et al.* [16], who found that the bending field of exchange springs multilayer and bilayer structures can be well described by the theoretical equation:

$$B_B = \frac{B_0}{(t_S)^n} \quad (7.03)$$

where B_0 and n are two constants for the given hard/soft exchange coupled system.

According to the boundary conditions, the parameter n can take 2 values. If the soft layers have no anisotropy and the hard layers are perfectly rigid, the theory predicts: $B_0 = \pi^2 A/(2M_{sat})$, and $n = 2$ [9], identical to the results found in [12]. If the soft layers are thick and without anisotropy, and the hard phases have a finite anisotropy, theoretical work [7] indicates $n = 1.75$. That prediction was confirmed by experimental studies [2, 3].

More recently, Bowden *et al.* [17] proposed an analytical and a numerical solution for a model of magnetic exchange springs in AFM coupled multilayer and bilayer structures. The authors supposed that the exchange interaction is the same for each nearest neighbour pair, the hard magnetic layers have an infinite anisotropy, and the anisotropy associated with the soft layer is zero.

Under those assumptions, the bending field is given by:

$$B_B = B_{ex}\left(\frac{\pi}{w}\right)^2 \tag{7.04}$$

where w is the number of mono-atomic layers in the soft phase, and B_{ex} is the TM-TM exchange field.

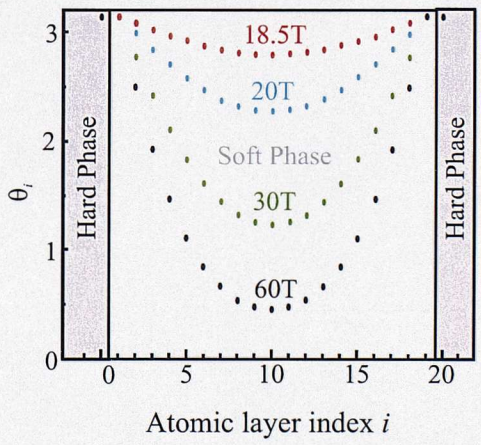

Figure 7.2 The evolution of the angle θ_i in the monoatomic layer i as a function of the applied field. The soft phase, constitued of 31 monoatomic layers, is sandwiched between two infinite hard layers.

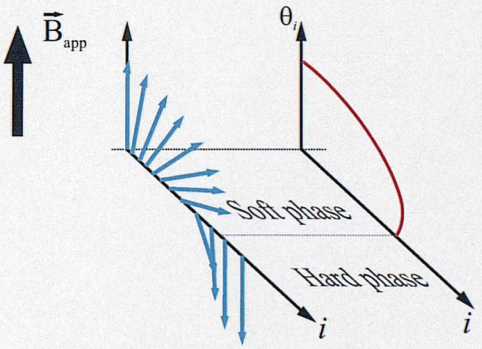

Figure 7.3 Schematic spin profile at the hard/soft phase interface.
The front of the drawing shows the approximate orientation of the TM spins in the soft layer. The background shows a plot of θ_i versus i.

These authors showed that the Jacobi elliptic *sn* function originally developed for bilayer exchange springs [12], provides a robust description of symmetric exchange springs for discrete distribution, as opposed to continuous magnetic moments. Fig. 7.2 and Fig. 7.3 show the evolution of the spin orientation in the multilayer system for different applied fields, when the hard layer anisotropy is infinite. The angular distribution of the magnetic moments is consistent with in-plane Bloch DW-like in the soft magnetic layer. The spins located away from the interface rotate more. By chosing a finite value for the anisotropy of the hard layer, calculations show that the reversible rotation in the soft layer is not pinned rigidly at the interface but rather propagates significantly into the hard layer. Consequently, the exchange spring is not only stored in the soft layer as is often assumed. This feature and its influence on the magnetic profile of the multilayer will be discussed in more detail in chapter 8.

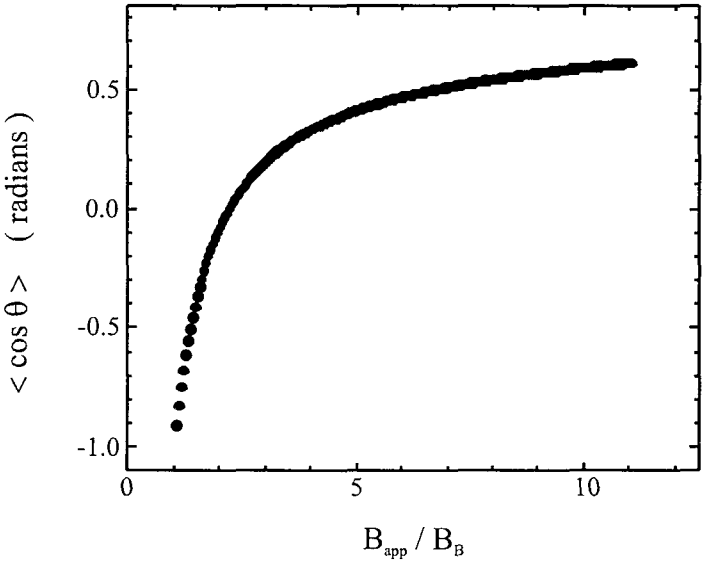

Figure 7.4 The generalised reduced magnetisation $\langle\cos\theta\rangle$ plotted versus B_{app} / B_B. In zero field, the spins in the soft layer are anti-parallel to the field. So the reduced magnetisation is <cos θ> = -1.0

Finally, it was shown that the reduced magnetisation $\langle\cos\theta\rangle$ can be written in a general form as a function of the factor B_{app} / B_B. Fig. 7.4 shows the shape of the

universal reduced magnetisation versus B_{app} / B_B. Therefore, the properties of many magnetic exchange springs that can occur in differing multilayer films can be described universally, regardless their nano-structure. [18].

7.2. Formation of a magnetic exchange springs feature in the YFe_2 layer

7.2.1. Experimental results

In this section, magnetometry measurements are reported for a single crystal Laves phase [100Å $DyFe_2$ – 75Å YFe_2] × 23 superlattice sample.

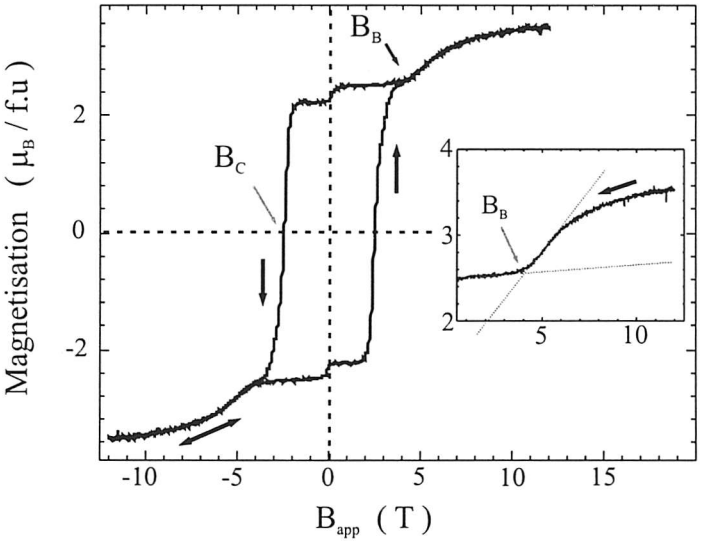

Figure 7.5 The hysteresis loop of [100Å $DyFe_2$ – 75Å YFe_2] × 23 multilayer sample at 100K. The coercivity B_C and the bending field B_B are indicated. The insert shows how B_B is experimentally determined from the M-B_{app} loop.

The isomorphous nature of the component, the nanometer control of the thicknesses, and the high quality interfaces allow the multilayer sample to be 'modelled' reasonably well.

Fig. 7.5 shows the typical hysteresis loop of the multilayer sample at 100K, with the magnetic field applied along [001] axis. The sharp magnetisation reversal is consistent with the expected [001] direction of easy magnetisation.

From an examination of the figure, three transition phases can be identified in the hysteresis loop:

- At zero field, the anti-ferromagnetic configuration

As discussed in chapter 6, at 0 field the state of minimum energy for the $DyFe_2$ - YFe_2 multilayer is obtained for a ferrimagnet-like arrangement, where all the spins in the YFe_2 layers are directed anti-parallel to the net magnetic moment of the $DyFe_2$ layers.

- The irreversible switching of the entire film at 2.55 T

The hysteresis loop presents a square loop indicating that the entire YFe_2 layers are strongly coupled to the adjacent $DyFe_2$ layers. As the result, the two phases switch coherently.

- The extra reversible magnetisation for $B_{app} \geq 4.1$ T

For fields larger than 4.1 T, a significant increase of magnetisation is observed. The overall increase is from $2.5\mu_B$ / f.u to $3.5\mu_B$ / f.u for field, in excess of 12 T.

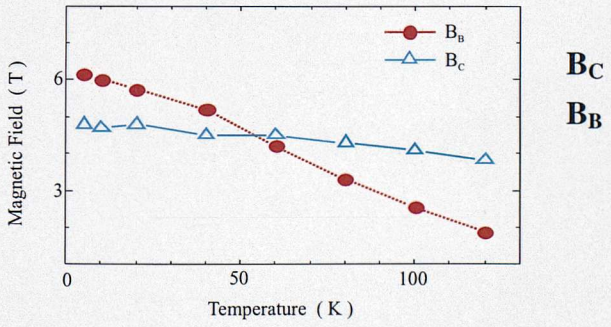

Figure 7.6 The temperature dependence of the the coercive field B_C and the bending field B_B of the multilayer sample: [100Å $DyFe_2$ – 75Å YFe_2] × 23.

To investigate the origin of the extra magnetisation, the hysteresis loop of the film was measured in the temperature range T = 5 K up to T = 150 K. In Fig. 7.6, the temperature dependence of the coercivity and of the bending field can be seen.
It will be observed that B_C and B_B behave differently as the temperature is increased. B_C shows a rapid decrease (~ 70 %) with increasing temperature. This is associated with the thermal evolution of the magneto-crystalline anisotropy at the Dy^{3+} site. However, the influence of temperature upon the bending field B_B is rather weak about 20 % decrease with increasing temperature. It can therefore be suggested that the observed extra-magnetisation is not due to DW pinning in the hard layer, but rather originates from a phenomenon taking place in the weak anisotropic YFe_2 layer. In Fig. 7.7, the hysteresis loop of the epitaxial $Dy_{0.5}Y_{0.5}Fe_2$ alloy film at selected temperatures is shown. Once again, the hysteresis loops are characteristic of a strong magnet. Unlike the multilayer system, the alloy film displays a saturation magnetisation state at all temperatures, and no extra magnetisation is observed. The result highlights the importance of the interface for the increase of magnetisation.

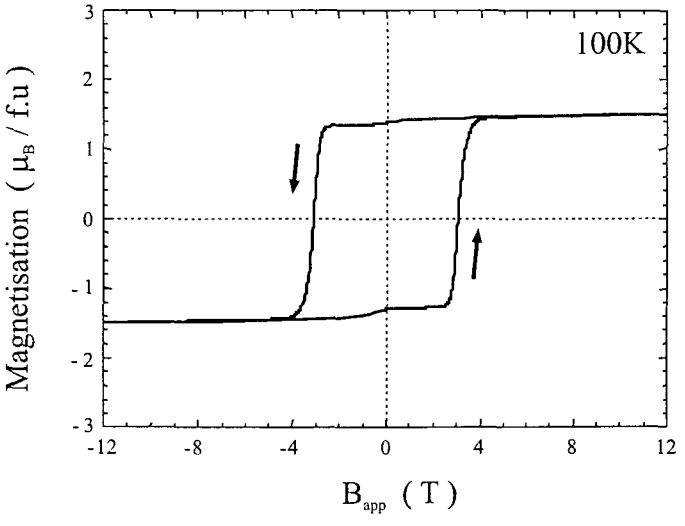

Figure 7.7 Magnetometry measurements of a 4000 Å $Dy_{0.5}Y_{0.5}Fe_2$ alloy film grown by molecular beam epitaxy. The hysteresis loop was measured with the magnetic field applied along a [001] axis.

A series of partial loop measurements was performed within the top and bottom right quadrants of the hysteresis envelop of [100Å $DyFe_2$ – 75Å YFe_2] × 23 multilayer.

After, the irreversible switching of the net magnetic moment in the direction of the field, the magnetisation is found to be reversible when the field is ramped up and down between the irreversible switching field ~ 2 T and +12 T. As long as the reverse field is less than 2 T the minor loop is always reversible. The reversibility of magnetisation is a characteristic signature of a magnetic exchange springs [2].

7.2.2. Discussion

As noted earlier, the increase in magnetisation observed in high fields can be readily understood in terms of magnetic exchange springs in the YFe_2 layers. Moreover a comparison of the experimental data with Bowden *et al.* prediction [17] shows that the theory provides a good description of the magnetic exchange springs in the AFM coupled multilayer.

In Fig. 7.8, the various spin configurations that occurs in the [100Å $DyFe_2$ - 75Å YFe_2] × 23 multilayer film are summarized.

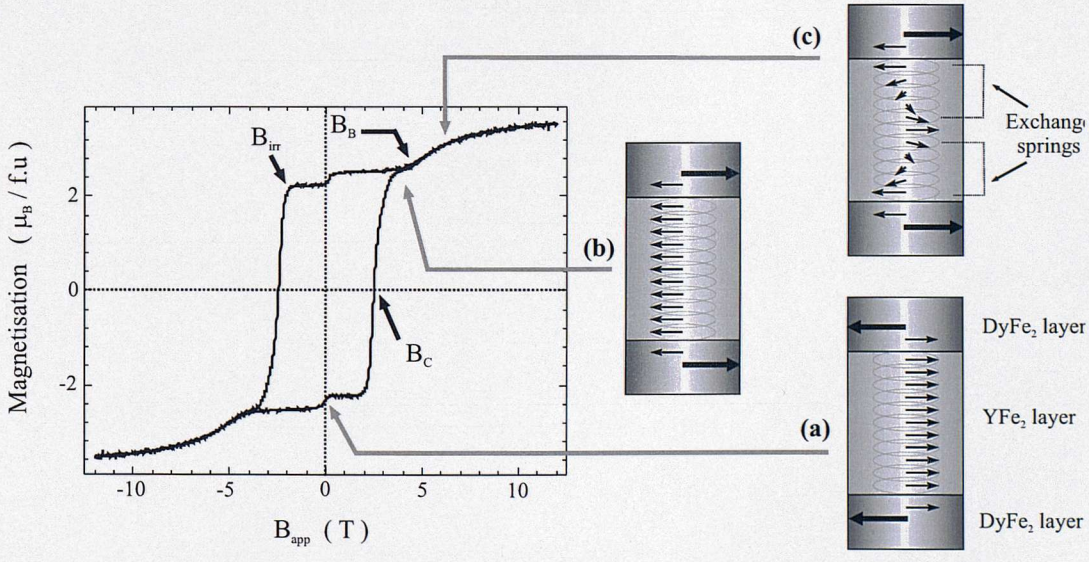

Figure 7.8 Hysteresis curve and spin configurations of the epitaxial film [100Å $DyFe_2$ - 75Å YFe_2] × 23, at different applied field:
a) $B_{app} < +B_C$ **b)** $B_C < B_{app} < +B_B$ **c)** $B_{app} \geq +B_B$
The measurement was performed at 100K, with the field applied along [001].

In the following explanation, it is considered that the film has been saturated in a large positive field. At zero field, the moment of the $DyFe_2$ and YFe_2 layers are pointing in opposite direction. The magnetic film remains in that state as long as the applied magnetic field B_{app} is in the regime $B_{irr} \leq B_{app} \leq B_B$. When the field is increased over B_B the spins in the soft layer starts rotating away from the anti-parallel alignment with the hard layer, as a result of the enhanced Zeeman energy. It was theoretically determined that the magnetic moments at the center of the soft layer first begin to rotate and at fairly high values of field, the DW-like nucleated at the interface is compressed against the hard layer and even penetrate it. The reversible rotation decreases the magnetisation associated with the anti-parallel YFe_2 layers, and thus enhances the magnetisation of the whole sample. Consequently, the increase of the magnetisation for $B_{app} \geq B_B$ is entirely due to the creation of exchange springs.

For thin YFe_2 layer, there is no signature of the formation of magnetic exchange springs for fields up to 12 T (ref. chapter 6). The magnetisation is completely governed by the anisotropy in the $DyFe_2$ layer. It is due to the fact that the magnetic walls have no room to develop in the thin YFe_2 layers, and therefore the soft phase magnetisation is firmly stuck to that of the $DyFe_2$ layer.

7.3. Engineering magnetic exchange springs

7.3.1. Experimental results

In this section, magnetisation curves of two series of epitaxially grown exchange springs $DyFe_2$ / YFe_2 multilayer films are presented and discussed. The first series of samples studied were [60Å $DyFe_2$ - 40Å YFe_2] × 40, [75Å $DyFe_2$ - 60Å YFe_2] × 30 and [75Å $DyFe_2$ - 100Å YFe_2] × 23. Their hysteresis loops at 100 K can be seen in Fig. 7.9.

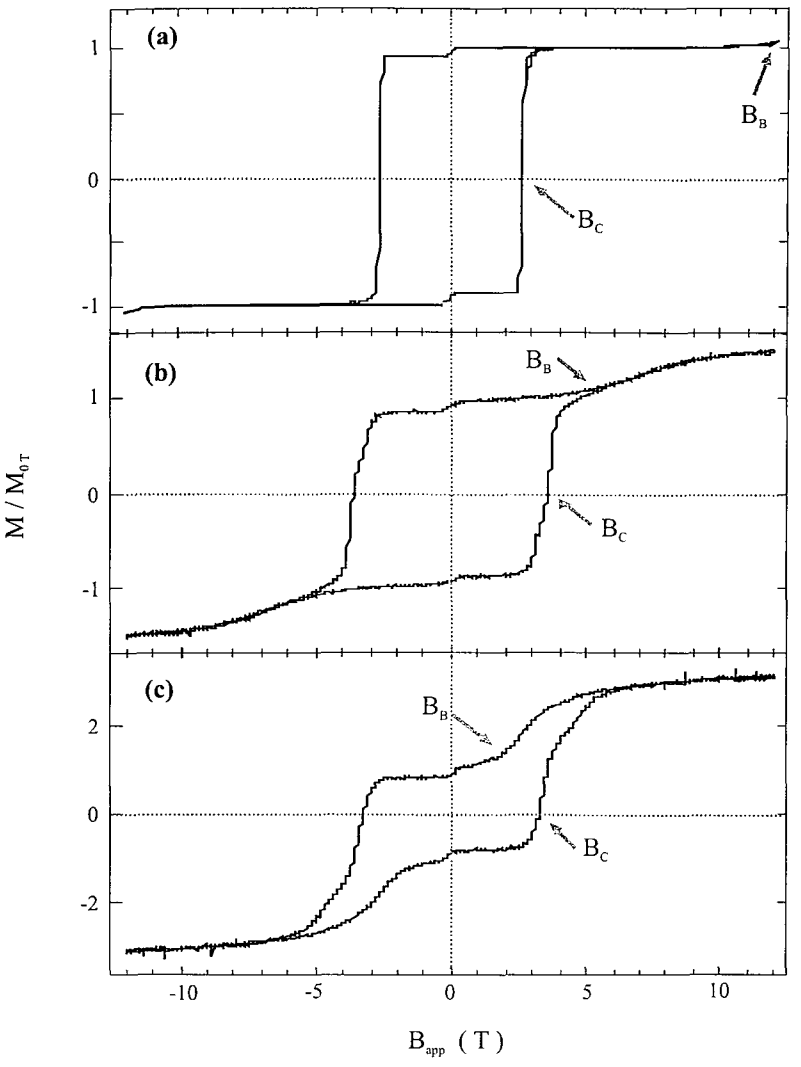

Figure 7.9 Hysteresis loop at 100 K of a selection of multilayer samples:
a) [60Å $DyFe_2$ - 40Å YFe_2] × 40
b) [75Å $DyFe_2$ - 60Å YFe_2] × 30
c) [75Å $DyFe_2$ - 100Å YFe_2] × 23
M_{0T} is the magnetisation of the sample at zero applied field.

The multilayer films are characterised by different nano-structure and different concentration ratio $DyFe_2$: YFe_2. The three specimens possess very different hysteresis loops. The sample [60Å $DyFe_2$ - 40Å YFe_2] × 40 exhibits a square M-B loop and a very small enhancement of its magnetisation at high fields. Actually, it presents the largest bending field B_B ~ 11.5 T compared to the two other films. The exchange springs is very clear in both the samples [75Å $DyFe_2$ - 60Å YFe_2] × 30 and

[75Å $DyFe_2$ - 100Å YFe_2] × 23, which exhibit a bending field of 4.0 T and 1.8 T respectively. As expected (ref. chapter 6), the samples with the thickest hard phase layer (75 Å) show the largest coercivity $B_C \sim 3.5$ T. The coercivity goes down to 20 % when the $DyFe_2$ thickness is reduced from 75 Å to 60 Å, whereas the bending field falls almost of a factor 3 when the YFe_2 thickness is increased from 40 Å to 60 Å.

These results suggest that by adjusting the thicknesses of the $DyFe_2$ and YFe_2 layers, the bending field B_B can be *tailored* so that either $B_B > B_C$ (Fig. 7.9.a), $B_B < B_C$ (Fig. 7.9.b) or $B_B \sim B_C$ (Fig. 7.9.c). However, similar results can be achieved by varying the temperature. In particular, the coercivity B_C falls rapidly with increasing temperature, whereas the bending field B_B falls by only 10-20% as the temperature is increased from 10 K to 300 K.

In Fig. 7.10, the hysteresis loops of $[x\ DyFe_2 - x\ YFe_2] \times N$ superlattices, with $x = 75$ Å, 100 Å, 150 Å and N the number of the bilayer repeat can be seen. The loops show a relatively sharp increase in magnetisation from 2 μ_B to ~ 4 μ_B, when B_{app} exceeds the bending field B_B. This is followed by an asymptotic approach to saturation. At first sight, one might expect these films to possess similar magnetic properties, as they possess the same $DyFe_2$: YFe_2 1:1 composition ratio. However, because of the creation of symmetric magnetic exchange springs, there are differences brought about by differing bending fields B_B. From an examination of both Fig. 7.9 and Fig. 7.10, it is clear that the bending fields B_B is larger when the thickness of the YFe_2 layers is reduced.

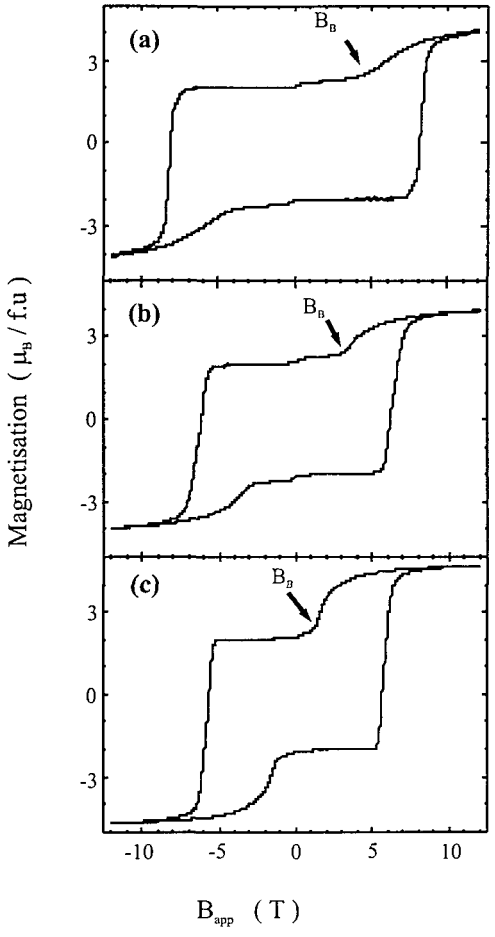

Figure 7.10 The M-B loop at 10 K of 3 structures with relative concentration ratio $DyFe_2$: YFe_2 1 : 1
a) [75Å $DyFe_2$ - 75Å YFe_2] × 27
b) [100Å $DyFe_2$ - 100Å YFe_2] × 20
c) [150Å $DyFe_2$ - 150Å YFe_2] × 13

7.3.2. The bending field B_B as a function of YFe_2 layer thickness

Fig. 7.11 shows how the bending field changes as a function of the thickness of the soft magnetic layer YFe_2, for samples in the relative concentration ratio $DyFe_2$: YFe_2 1 : 1. It is found that by increasing the YFe_2 layer thickness, the bending field B_B reduces quickly and then slowly for further thickness enhancement.

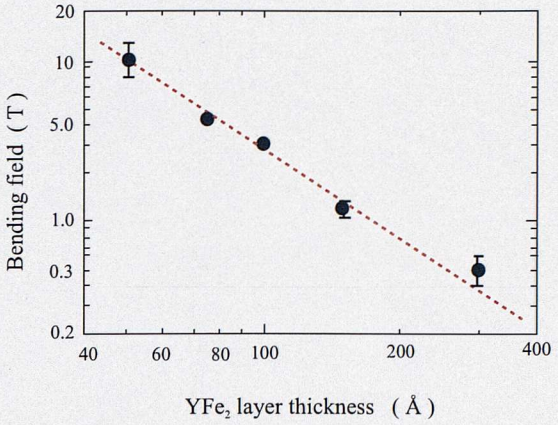

Figure 7.11 *log-log* plot of the bending field B_B as a function of the YFe_2 thickness x in $[x\text{Å } DyFe_2 - x\text{Å } YFe_2] \times N$ multilayer samples. Bullets are the experimental data and the solid line represents the fitted curve.

The experimental data, plotted on a *log-log* scale, falls almost on a straight line which can be fitted by the equation:

$$B_B = k\, x^n \tag{6.05}$$

where $\log_{10}(k) = 4.1 \pm 0.2$ and $n = -1.83 \pm 0.12$.

The behaviour of B_B is very similar in nature to that of a nearest neighbour exchange model of Eq. 7.04 [18].

The exponent n is very nearly equal to -2, while the fitted exchange field is ~ 910 T. However, it should be acknowledged that Eq. 7.04 was deduced, assuming infinite pinning at the hard $DyFe_2$ interfaces. In practice, there will be some penetration of the exchange springs into the hard layers, thus effectively increasing the thickness available to the YFe_2 spring. Note that the exchange field determined experimentally by Ref. [20] is in excess of 680 T. But this may reflect the inadequacies of the nearest neighbour effective field model.

As mentioned earlier, Bowden *et al.* have derived a universal form for the reduced magnetisation $\langle \cos\theta \rangle$, the solution of the Eq. 7.01. The authors showed that $\langle \cos\theta \rangle$ depends on the dimensionless factor B_{app} / B_B, and that the properties of a variety of magnetic exchange spins can be well-fitted in terms of a universal curve.

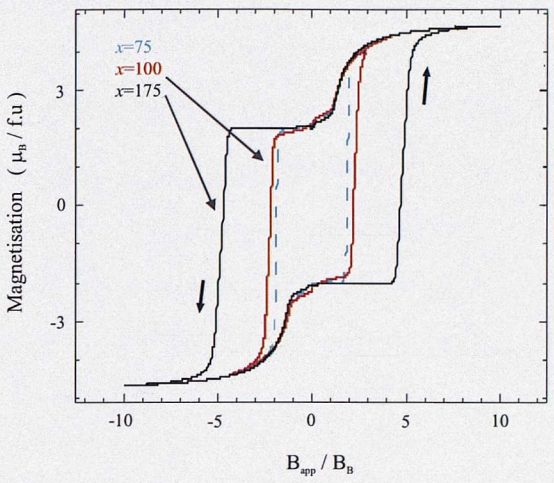

Figure 7.12 The universal form of the hysteresis loop of the epitaxial multilayers [xÅ $DyFe_2$ - xÅ YFe_2]×N, whith $x = 75$, $x = 100$, $x = 150$, plotted versus the factor B_{app} / B_B.

This is illustrated in Fig. 7.12 which shows the magnetisation of the samples [x Å $DyFe_2$ – x Å YFe_2] × N, whith $x = 75$ Å, $x = 100$ Å, $x = 150$ Å, plotted versus B_{app} / B_B. The magnetisation curves fall on a universal curve in the exchange spring region.

7.4. Conclusions

Magnetisation loops for MBE grown $DyFe_2$ / YFe_2 superlattice samples with relatively thick YFe_2 layers, have been presented and discussed. The results show the existence of model exchange springs in the magnetically soft YFe_2 layers, pinned at their edges by the magnetically hard $DyFe_2$ layers. The presence of magnetic exchange springs has a significant influence on the shape of the loop. In high fields, it causes an increase of the magnetisation followed by an asymptotic approach to saturation. This behaviour is characteristic of AFM coupled system exhibiting exchange springs. Moreover, it was shown that the shape of the hysteresis loop in

this field regime is identical for all samples, provided they are plotted in terms of B_{app} / B_B.

By plotting the bending field B_B as a function of YFe_2 thickness x, it was found that $B_B \propto 1 / x^n$, where n is very close to 2. Consequently by adjusting x, it is possible to engineer hysteresis loops with $B_C > B_B$, $B_C \sim B_B$, $B_C < B_B$.

MBE grown $DyFe_2$ / YFe_2 multilayer structure constitute an excellent system to investigate the magnetic exchange springs phenomenon. It provides an alternative means of manipulating Bloch DW.

References

[1] T. Nagahama *et al.*, *J. Appl. Phys.* **31**: 43-49 (1998)

[2] E. E. Fullerton *et al.*, *Phys. Rev. B* **58** (12): 193 (1998)

[3] E. Fullerton *et al.*, *J. Magn. Magn. Mater.* **200**: 392 (1999)

[4] R. Skomski and J. M. D. Coey, *Phys. Rev. B* **48** (21): 1993 (15812)

[5] J. M. D. Coey, *J. Magn. Magn. Mater.* **248**: 441-456 (2002)

[6] J. S. Jiang *et al.*, *I.E.E.E Trans. Magn.* **35**: 3229 (1999)

[7] T. Leineweber and H. Kronmuller, , *J. Magn. Magn. Mater.* **176**: 145 (1997)

[8] I. A. Al-Omari and D. J. Sellmyer, *Phys. Rev. B* **52**: 3441 (1995)

[9] S. Wuchner *et al.*, *Phys. Rev. B* **55**: 11576 (1997)

[10] S. M. Parhoter and J. Wecker, *IEEE Trans. Magn.* **32**: 4437 (1996)

[11] M. Shindo, *J. Appl. Phys.* **81**: 4444 (1997)

[12] E. Goto, *J. Appl. Phys.* **36**: 2951, 1965

[13] R. Coehoorn *et al.*, *J. Magn. Magn. Mater.* **80**: 101 (1989)

[14] J. M. D. Coey, *Solid State Commun.* **102**: 101 (1997)

[15] J. Ding *et al.*, *J. Magn. Magn. Mater.* **124**: L1 (1993)

[16] R. E. Camley, *Phys. Rev. B* **35**: 3608 (1987)
R. E. Camley and D. R. Tilley, *Phys. Rev. B* **37**: 3413 (1988)
R. E. Camley, *Phys. Rev. B* **39**: 12316 (1989)

[17] Bowden *et al.*, *J. Phys. Condens. Mater.* **12**: 9335-9346 (2000)

[18] G. Bowden et al., *J. Magn. Magn. Mater.* **240**: 556-558 (2002)

[19] E. F. Kneller and R. Hawig, *IEEE Trans. Magn.* **27**: 3588 (1991)

[20] J. J. M. Franse and R. J. Radwanski, *Handbook of Magnetic Materials* vol. 7, edited by K. H. J. Buschow (North-Holland, Amsterdam (1993)

Chapter 8

Influence of magnetic exchange springs on the coercive field

In the chapter 7, it was shown that for sufficiently thick YFe_2 layers, pinning by $DyFe_2$ layers gives rise to the creation of magnetic exchange springs into the soft phase. In fact, multilayer structures provide an excellent model system for the study of magnetic exchange springs.

In this chapter, the influence of the exchange springs on YFe_2 magnetically dominated multilayers systems are presented and discussed. Magnetic measurements on two series of nano-structured $DyFe_2$ / YFe_2 multilayer films are reported:

- *YFe_2 layers are magnetically dominant,*
- *YFe_2 layers magnetically compensate the hard layers.*

In the first section, the physics of two mechanisms based on interfacial interactions in layered systems, and their influence on their magnetic properties, is reviewed. In the second section, the role played by exchange spring penetration, from the soft YFe_2 into the hard $DyFe_2$ layers, on the irreversible switching of the $DyFe_2$, is presented and discussed.

8.1 Interfacial interactions

Magnetic interfacial interactions have been intensively studied in recent years [1 – 19]. Layered structures have been chosen preferentially because they offer a large interface area between the two magnetic phases present.

Exchange bias is one of the interfacial interactions that has attracted the widest attention in the last few years. Specifically, it dictates the effect that an AFM layer has on the magnetic response of neighbouring FM layer. It was first mentioned in 1956 by Meiklejohn and Bean who studied Co particles embedded in their native AFM oxide CoO [1]. But, it was the reduction of the saturation fields required to observe GMR in exchange biased systems [2], as compared to standard GMR multilayer systems [3], which triggered a renewed interest in the phenomenon [4]. Exchange bias has been observed in many different systems containing FM / AFM interfaces, such as small particles [1, 5-7], inhomogeneous materials [1, 6-9] and thin films [1, 7, 10 - 12]. However, thin AFM / FM layered systems are favoured because of the improved control over the interface, and because they are more amenable for the development of devices [4, 13].

The most notable changes in the FM hysteresis loop due to the surface exchange coupling are a coercivity enhancement, and a shift in the hysteresis loop of the FM. This shift is generally referred to as the exchange biased shift B_E. Fig. 8.1 shows a schematic illustration of a typical exchange biased system, at some points around the hysteresis loop.

At magnetic saturation, the AFM spins next to the FM layer align themselves ferromagnetically to those of the FM layer, as a result of ferromagnetic coupling. Note that the other spin planes in the AFM 'follow' the AFM order, producing net zero magnetisation (Fig. 8.1.a). When the field is reversed, the FM spins start to rotate, whereas the AFM spins remain unchanged due to the large AFM anisotropy (Fig. 8.1.b). The interfacial interaction between the FM / AFM spins at the interface, tries to align the FM spins with the AFM spins ferromagnetically at the interface. In other words, the AFM spins at the interface exert a microscopic torque on the FM

spins, to keep them ferromagnetically aligned. Therefore, the FM spins possess just one single stable configuration in zero magnetic field.

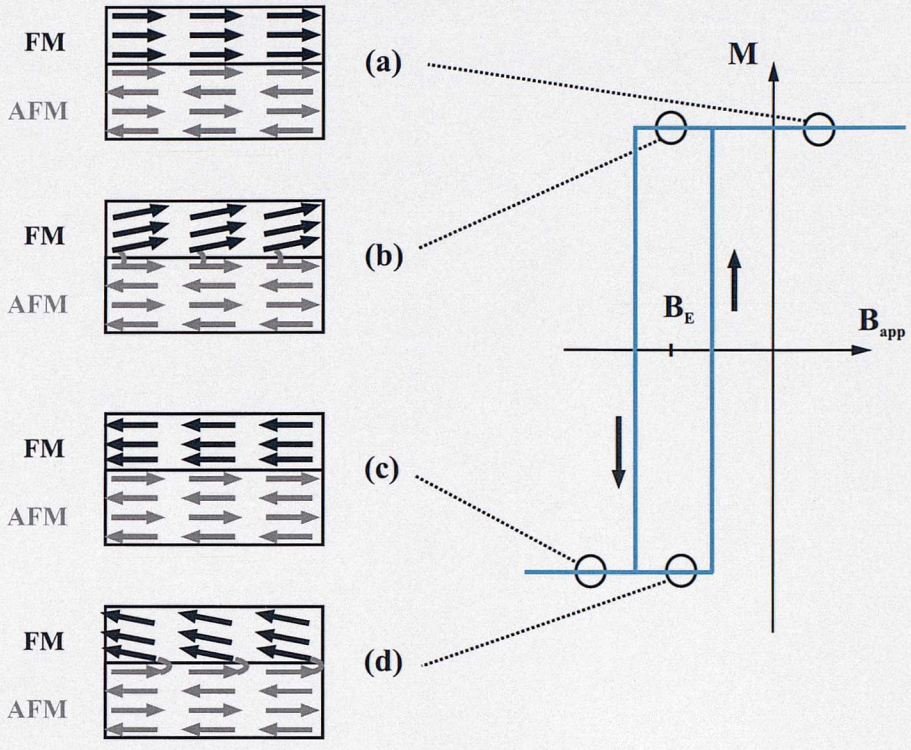

Figure 8.1 Schematic diagram of the spin configuration of an FM / AFM bilayer at different stages (a)-(d) of an exchange biased hysteresis loop.

To reverse the ferromagnetic layer, it is necessary to apply a reverse field of greater than B_E, the exchange bias field (Fig. 8.1.c). The material behaves as if there was an extra (internal) biasing field B_E. Consequently, the FM hysteresis loop is shifted in the field axis, *i.e.* exchange bias [1, 6, 7]. Although this simple phenomenological model gives an intuitive picture, there is little quantitative understanding of the phenomena. Experimental studies and theoretical models [7, 14] indicate that intrinsic magnetic properties of the AFM layer such as the magneto-crystalline anisotropy, exchange stiffness, and crystalline texture [11, 15-17] as well as intrinsic properties such as domain size and interface roughness [16, 18, 19] will influence the resulting response of the FM layers.

Another peculiar feature, triggered by interfacial exchange is the inverted magnetic hysteresis loops, where the forward and reverse branches are shifted in opposite directions so that they completely cross over. This topic has been of increasing interest in recent years [20-24]. In Fig. 8.2, it is shown an example of inverted hysteresis loops for a Co-based layer alternating with Cu layers [25].

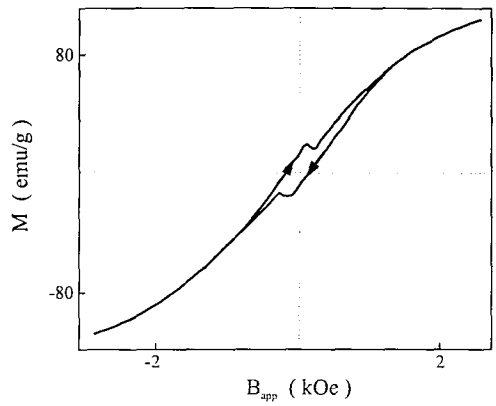

Figure 8.2 Hysteresis loops for CoO / Cu multilayer with B_{app} perpendicular to the film plane. [26]

When the field is reduced to zero after saturation, the magnetisation crosses the zero magnetisation axis well above the irreversible switching field. Then, the magnetisation increases in reverse direction, and a negative remanence at zero field is observed.

Negative coercivities have also been observed in the systems CoO / Co composite films [25 - 26], δ-MnGa / (Mn, Ga, As) / δ-MnGa trilayer films [20], Gd-Fe / Tb-Fe bilayer films [21], Gd / Co bilayer films [22] and NiFe / TbCo bilayer films [23].

This peculiar behavior has been attributed to exchange field biasing across the interface between the two layers, characterized by different magnetic hardness and coupling to the AFM layers. However, a different mechanism has been proposed by Ref. [24]. These authors argued that negative coercivity is a consequence of the dipolar fields emanating from the hard magnetic layers which leads to demagnetization of the soft layers.

In addition, a theoretical investigation using a model with two non-identical A and B phases, both with uniaxial anisotropy, has been reported by Ref. [25], as a function of (*i*) anisotropy strength, (*ii*) interface exchange strength, and (*iii*) angle between the anisotropy axes and applied field. The calculations show that partially inverted hysteresis loops can be obtained for selected values of anisotropy and selected negative (AFM) values of interface exchange (Fig. 8.3). Further, if the assumption of rigid rotation is relaxed (*i.e.* the spins in phase A and B are able to deform), then the field range over which inverted behavior occurs is reduced.

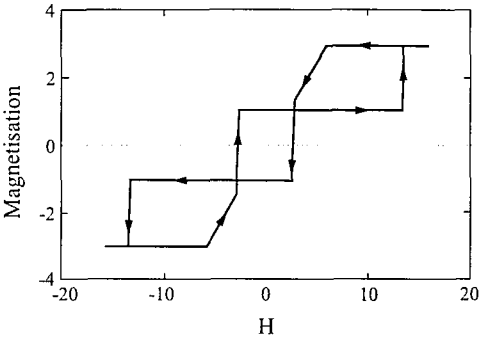

Figure 8.3 Magnetisation of a bilayer system calculated by Ref. [25]. The system is characterised by a partially inverted hysteresis loop.

8.2 The effect of the magnetic exchange springs on the magnetisation reversal mechanism

8.2.1 Experimental results

In this work, the irreversible switching field B_{irr} is defined as the field from which the magnetisation starts reversing to the direction of the applied field. To probe the influence of the magnetic exchange springs on B_{irr}, magnetometry measurements were carried out on multilayer samples [75 Å $DyFe_2$ –w YFe_2] × N with fixed

thickness of $DyFe_2$ layers and varying thickness of YFe_2 layers: w = 75 Å, 100 Å and 150 Å. The samples are all 4000 Å thick.

Typical hysteresis loops of the superlattices at 10 K can be seen in Fig. 8.4.

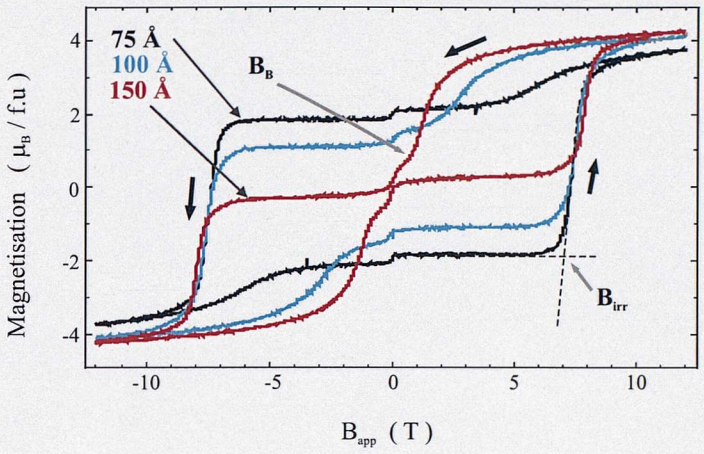

Figure 8.4 10 K hysteresis loops of $DyFe_2$ / YFe_2 multilayers with various YFe_2 layer thickness w but fixed $DyFe_2$ layer thickness of 75 Å. The magnetic field is applied along [001].

The samples exhibit magnetic exchange springs, and are characterised by well defined bending fields B_B and switching fields B_{irr}. The film with w = 150 Å possesses a peculiar magnetic hysteresis loop, which is discussed in more details in section 8.5. Nevertheless, the parameters B_B and B_{irr} can be determined also for that specimen.

The three samples are characterised by bending fields B_B smaller than B_{irr}. Therefore, while the magnetisation reversal of the hard layer occurs, magnetic exchange springs develop simultaneously in the soft phase. As expected from Eq. 7.04, the bending field decreases strongly with increasing YFe_2 layer thickness, a reduction of more than 80 % when the thickness of the soft phase is doubled. The evolution of B_{irr} is less pronounced. It increases from 6.98 T to 7.5 T when the thickness ratio w / 75 is doubled. The results for the three samples are summarised in Table 8.1

w	75	100	150
B_{irr} (T)	6.98	7.1	7.5
B_B (T)	4.5	2	0.8

Table IV The switching field B_{irr} and the bending field B_B of the series of the samples, whose the hysteresis loops are shown in Fig. 8.4

The experimentally determined B_{irr} for the three samples are in consirable disagreement with the predictions of theory (Eq. 6.12). This is particularly clear for the superlattice [75 Å $DyFe_2$ – 150 YFe_2] × 18, for which the exchange springs dominates the magnetic behaviour of the film. It is experimentally found B_{irr} = 7.5 T whereas the theory gives a much larger value. It is clear therefore that the actions of magnetic exchange springs tend to reduce the coercivity of the superlattice films.

Note also that the three samples present the same slope of the magnetisation reversal in the field regime of B_{irr}.

In Fig. 8.5, the hysteresis loops in the top positive quadrant, and their first derivatives dM / dB_{app} are shown for the two samples [80 Å $DyFe_2$ - 20 YFe_2] × 40 (Fig. 8.5.a) and for the sample [75 Å $DyFe_2$ - 150 YFe_2] × 18 (Fig. 8.5.b), respectively.

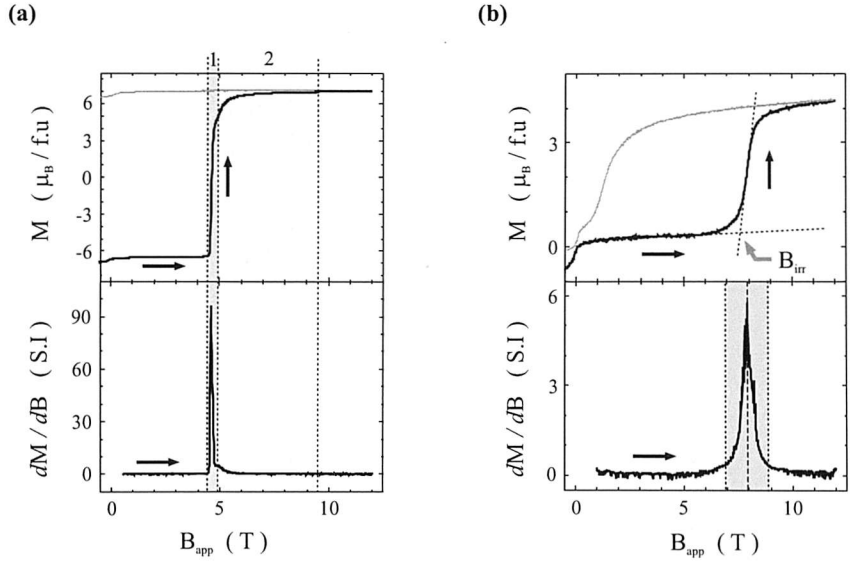

Figure 8.5 Hysteresis loop at 10 K and dM / dB_{app}, the first derivative of the magnetisation M versus increasing applied field B_{app}, for the samples:
a) [80 $DyFe_2$ – 20 YFe_2] × 40 **b)** [75 $DyFe_2$ – 150 YFe_2] × 18

The [80 Å $DyFe_2$ - 20 YFe_2] × 40 film is characterised by a strong exchange coupling between the hard and the soft layers which leads to the uniform reversal of the magnetisation as a single entity. However, the [75 Å $DyFe_2$ - 150 YFe_2] × 18 film possesses a thick soft phase which enables magnetic exchange springs to develop. The two films show different slopes in magnetisation reversal. The sample with thin YFe_2 layer presents a sharp magnetisation reversal, in the range field $B_{app} = 4.6 \pm 0.3$ T. Furthermore, it is observed that the magnetisation reversal is not symmetric about the field of maximum value of dM / dB_{app}. This suggests that the magnetisation reversal occurs by two different mechanisms. In the field range indexed '1', the sharp magnetisation jump is typical of magnetisation reversal by DW motion. In the field range indexed '2', the magnetisation increase is more progressive.

For the exchange springs sample (Fig. 8.5.b), the magnetisation reversal occurs in a broader field range: 7.9 ± 1 T. dM / dB_{app} displays a symmetric feature about the field of maximum value of dM / dB_{app}.

8.2.2 Discussion and theory

It is evident that for the samples with thick YFe_2 layers, the coercivity cannot be described by the Stoner and Wohlfarth models. For small YFe_2 layers, the Stoner-Wohlfarth (S-W) model does apply because the bending field B_B of the YFe_2 layer is well in excess of the irreversible field of the $DyFe_2$ layer. But as the YFe_2 layer is increased, the incipient presence of an exchange spring makes an impact. The formation of the magnetic exchange springs in the soft layer can be taken into account in the modified form of the S-W model by writing:

$$B_C = \frac{2K_H t_H}{M_H t_H - M_S \langle \cos\theta \rangle t_S} \tag{8.01}$$

where $\langle \cos\theta \rangle$ is the average of the projection of the spin moments of the YFe_2 layers along $\vec{B}_{app}$. When exchange springs are set up in the soft magnetic layers, the magnetisation $M_S \langle \cos\theta \rangle$ associated with the YFe_2 layers will fall in magnitude,

eventually changing sign. Thus, the denominator in Eq. 8.01 will increase in magnitude, causing the coercivity to fall. Nevertheless, there is still disagreement between theory and experimental data. Eq. 8.01 does not include the influence of the penetration of the magnetic exchange springs into the hard phase. Because the Bloch-type wall penetrates into the hard layer, the effective thickness of the soft phase layer is increased.

In the following, the temperature dependence of the coercivity B_C is studied.

In chapter 6, Gaunt's theory for the temperature dependence of B_{irr}, was used to investigate the magnetization reversal mechanism in strongly coupled $DyFe_2$ / YFe_2 multilayers. In brief, Gaunt *et al.* believe that the reversal of the magnetisation in a ferromagnet occurs by motion of domain walls, which strongly perturbed by either WDWP or SDWP pinning sites [27].

In chapter 6, it was found that in the samples which do not exhibit magnetic exchange springs, the motion of the DW was affected by SDWP centres.

In Fig. 8.6 it is shown the temperature dependence of the switching field B_{irr} for the samples [75 Å $DyFe_2$ - 150 Å YFe_2] × 18 and [75 Å $DyFe_2$ - 100 Å YFe_2] × 23 in the temperature range from 5 K to 120 K.

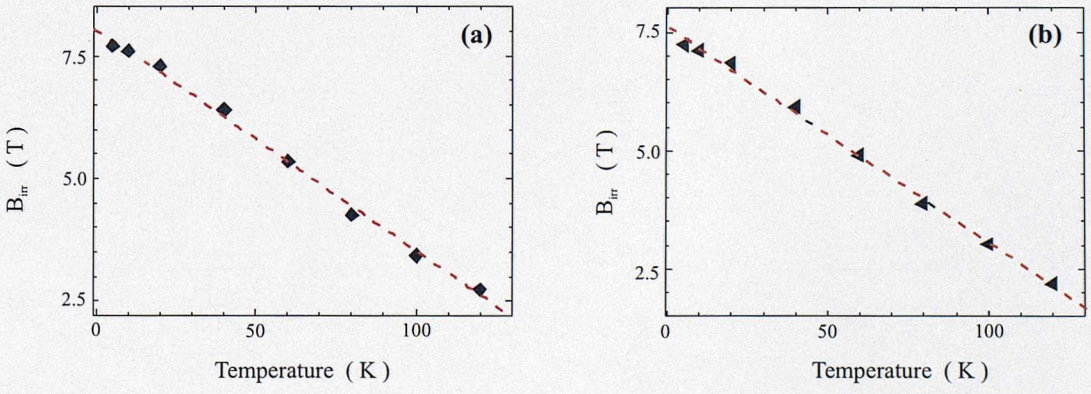

Figure 8.6. Temperature dependence of the switching field B_{irr} of the sample:
a) [75 Å $DyFe_2$ - 150 Å YFe_2] × 18 **b)** [75 Å $DyFe_2$ - 100 Å YFe_2] × 23
The bullets are experimental data extracted from the M-B loop, and the dashed line is the best fit using the Weak DW Pinning model.

For both samples, the best fit is obtained using the WDWP model (dashed line):

$$B_{irr} = B_0(1-\alpha T) \tag{8.02}$$

where B_0 is the irreversible field at 0 K and α is a constant. Somelike $DyFe_2$ dominated films, the B_{irr} of exchange springs superlattices display a linear dependence with the temperature. This result can be understood in terms of competition between localised magneto-crystalline anisotropy (from the $DyFe_2$) and strong exchange interactions Fe-Fe (from the $DyFe_2$ and the YFe_2 layers).

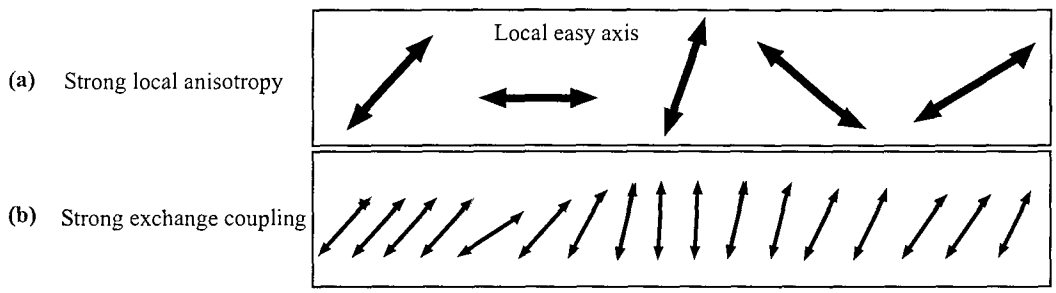

Figure 8.7
a) Schematic representation of the variation of the local anisotropy easy axis with position with weak exchange interaction between the magnetic moments.
b) Variation of the local anisotropy when a strong exchange interaction unbalances the local magneto-crystalline anisotropy.

For films with thin YFe_2 layers, the soft phase thickness is too short for magnetic exchange springs to develop. The magnetic profile is dominated by the strong magneto-crystalline anisotropy of the $DyFe_2$ phase. During the magnetisation reversal, DW's with strong local anisotropy form. They can be considered to be moving in an irregular and rapidly changing potential. Therefore the material parameters change abruptly at the interface between the defects and the matrix (Fig. 8.7.a) and thus the magnetisation reversal mechanism can be described by the model of SDWP. On the other hand, the sample [75 Å $DyFe_2$ - 150 Å YFe_2] × 18 is a so-called YFe_2 dominated sample, for which the exchange springs is the principle *driving force*. The exchange interaction Fe-Fe in the large amounts of YFe_2, unbalances the strong Dysprosium anisotropy and smoothes the variation in local anisotropies (Fig. 8.7.b). It tries to minimise misalignment of neighbouring spins. As

a result, the DW's can be considered to be moving in an irregular but slowly changing potential, thus the magnetisation reversal of the structure is better described by the WDWP model.

8.3 Engineering negative coercivity in $DyFe_2$ - YFe_2 multilayer films

8.3.1. Experimental results

In this section, it is presented and described the easy axis magnetisation curves for the YFe_2 magnetically dominated samples $[x$ Å $DyFe_2 - 4{\times}x$ Å $YFe_2] \times N$, where x = 20 Å, 30 Å, 40 Å, 45 Å, 50 Å, 55 Å and N = 40 Å, 27 Å, 20 Å, 18 Å, 16 Å, 15 Å.

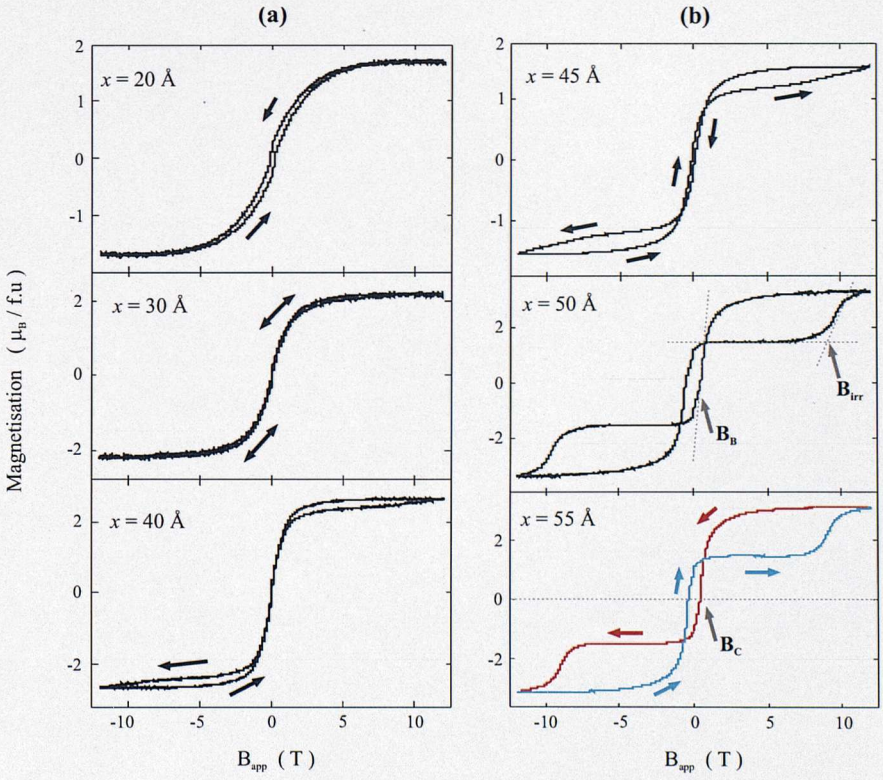

Figure 8.8 M-B loop (B_{app} along [001] direction) at 20 K for multilayer samples with the thickness ratio x / $4x$ where:

a) x = 20, 30, 40 Å **b)** x = 45, 50, 55 Å

In principle, the multilayer films should possess similar magnetic characteristics, because they are all nominally $Dy_{0.2}\ Y_{0.8}\ Fe_2$. However, the measurements show that their magnetic properties are strongly dependent on the width of the layers.

The results are subdivided in two groups according to the thickness of the $DyFe_2$ layers: $x \leq 40$ Å (Fig. 8.8.a) and $x > 40$ Å (Fig. 8.8.b).

- For $x \leq 40$ Å

The magnetisation loops of that series of superlattices exhibit positive coercive field B_C and remanent magnetisation M_{rem}. Note that B_C and M_{rem} are almost equal to zero. For example, the multilayer [40 Å $DyFe_2$ / 160 Å YFe_2] × 20 has a coercivity $B_C = + 0.02$ T. The M-B loops do not exhibit a clear hysteretic feature. In fact, they are practically reversible for applied field in the range +12 T / -12 T. However for the sample with $x = 40$ Å, the magnetisation loop shown some hysteretic behaviour when the applied magnetic field exceeds ± 7.9 T. The saturation, which should be greater than 3 μ_B / f.u [5], is not achieved in the available field range. This suggests that the $DyFe_2$ moments are not flipped by the applied magnetic field and it is quite possible that the magnetic response is that of the magnetic exchange springs. With increasing (decreasing) the applied field, magnetic exchange springs in the YFe_2 layers wind (unwind) reversibly. B_{app} is not large enough to switch the magnetisation of the $DyFe_2$ layers, which remains frozen in one direction. Therefore, there is no indelible trace of irreversibility for the hysteresis envelope.

- For $x > 40$ Å

The first significant result is that the hysteresis loops are inverted and they exhibit a negative coercivity. In going from -12 T to +12 T, the magnetisation loop crosses zero in the positive applied field regime. The larger negative coercivity $B_C = - 0.5$ T is observed for the sample with $x = 55$ Å. The magnetisation reversal occurs before the applied field is reduced to zero. There is a cross over between both branches of the major hysteresis loop, with negative remanence in zero magnetic field. The experimental results do not break the 3rd law of thermodynamics because the net work $W_H \propto \oint \vec{B} \bullet d\vec{M}$ in going around the loop is positive.

[5] The saturation of the magnetisation is achieved when there is a FM alignment between the $DyFe_2$ and the YFe_2 magnetic moments i.e. : (7 + 3×4)/5 ~3.8 μ_B / f.u

The magnetisation curves show several phase transitions as a function of the applied magnetic field. For B_{app} in the range $0 \leq B_{app} \leq B_{irr}$, the magnetisation is constant $M \sim 1.0\ \mu_B$ / f.u. But when a field in excess of B_{irr} is applied, there is a sharp increase of the magnetisation to $M = 3\ \mu_B$ / f.u. Subsequently, when the field is reduced, the magnetisation decreases reaching zero. The bending field B_B for all the three samples is positive and smaller than 1 T.

To probe the irreversible behaviour of the magnetisation of the samples with $x > 40$ Å, partial hysteresis loop measurements were performed. This can be done by first saturating the sample in a large positive magnetic field, and subsequently reducing and reversing the field up to a value of B_{min}, where $-6\ T \geq B_{min} \geq -12\ T$, before increasing the field back to +12 T. The results of this asymmetric cycling procedure can be seen in Fig. 8.9.

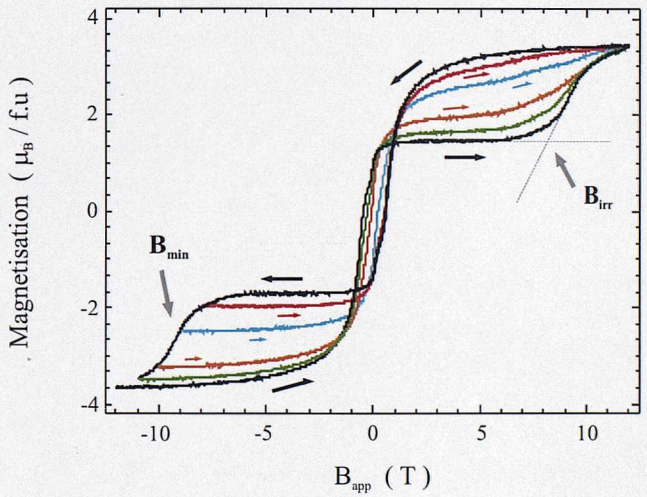

Figure 8.9 Minor loops for [50 Å $DyFe_2$ / 200 Å YFe_2] × 16 at 20 K for various asymmetric magnetic cycles.

When the magnetic cycle is only taken to $B_{min} = -7$ T, the magnetisation curve is practically reversible. Indeed, provided the magnetic field is not taken below $-B_{irr}$, the magnetisation curve between $-B_{irr}$ and +12 T is completely reversible. This suggests therefore that all of the $DyFe_2$ layers remain pointing in their respective directions during the whole asymmetric magnetic cycle. The reversible nature of the magnetic response is therefore due solely to the winding and unwinding of the

exchange springs with increasing and decreasing field respectively. But when B_{app} is taken below $-B_{irr}$, the system becomes unstable and some of the magnetic moments of the $DyFe_2$ layers flip in the direction of the reverse field, accompanied by the simultaneous creation of magnetic exchange springs in the YFe_2 layers. When the field B_{min} exceeds -10 T, the coercivity takes on a negative value and saturates at a maximum value of -0.5 T.

It is clear therefore that the degree of irreversibility is strongly dependent on the magnitude of the final applied field B_{min} of the partial loop.

The measured coercivities versus the thickness of the hard phase of the multilayer films [x Å $DyFe_2$ – $4x$ Å YFe_2] × N are summarised in Fig. 8.10.a.

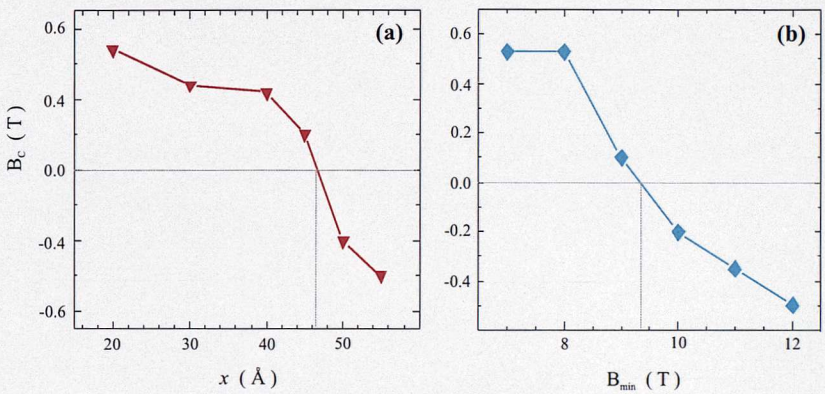

Figure 8.10 Dependence of the coercivity B_C with:
a) the thickness of the $DyFe_2$ layer, **b)** the maximum reversal field B_{irr}

It can be seen that the sign of the coercivity of the superlattices changes from negative to positive with decreasing thickness x, passing through zero at ~ 41 Å. Fig. 8.10.b shows the behaviour of B_C versus the value of the maximum reversal field B_{min}. It will be observed that the coercivity decreases with increasing B_{min}, vanishing at B_{min} = 9.4 T. From a comparison of the two figures, it is clear that the reversibility of the magnetisation observed for the samples with $x \leq 40$ Å is due solely to the limitations of the available applied field. Fields which are less than 12 T are not large enough to flip the $DyFe_2$ moments. For such samples, the magnetisation of the $DyFe_2$ layers is fixed. So the applied field enables only the winding and unwinding of the magnetic exchange springs.

8.3.2 Discussion

When the thickness of YFe_2 is increased, the existence of the exchange springs is found to have a strong impact on the hysteresis loop. The spin configurations of the negative coercivity samples as a function of the magnetic field are summarised, as inserts, in Fig. 8.11.

In a large negative applied field in excess of -12 T, the minimum energy configuration is achieved with all the $DyFe_2$ moments pointing in the direction of the applied field (Fig. 8.11.a). This means that the exchange springs are necessarily set up in the thicker YFe_2 layers. Subsequently, as the field is reduced, the springs unwind, eventually reaching the stable AFM state between the adjacent $DyFe_2$ - YFe_2 layers (Fig. 8.11.b). The Dy moments are pointing in the direction of the field, but due to the strong AFM coupling, the Fe moments through the entire films are anti-parallel to B_{app}. Since this state is characterised by a positive magnetic moment ~1μ_B / f.u, the magnetisation is positive even though B_{app} is still negative. Thus the M-B_{app} loop is characterised by a negative coercivity.

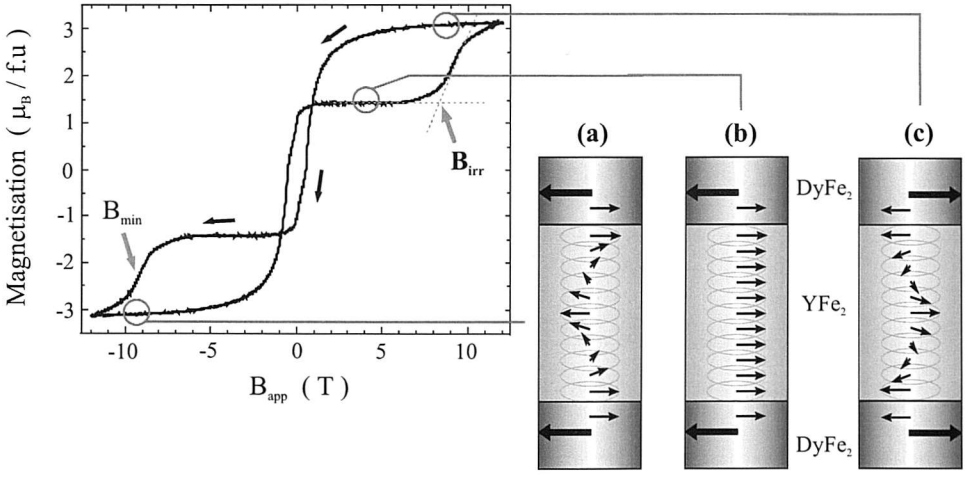

Figure 8.11 The hysteresis loop at 20 K of the negative coercivity multilayer [50 Å $DyFe_2$ / 200 Å YFe_2] × 16. Also included is the spin arrangement at different applied field.
a) Development of magnetic exchange springs in the YFe_2 layer
b) Anti-ferromagnetic state
c) Magnetisation reversal and simultaneous formation of exchange springs
The large (small) arrows represent Dy (Fe) magnetic moments.

This occurs because an overall gain in energy is achieved by maximizing the Fe-Fe exchange energy in the YFe_2 layers, while maintaining the Zeeman energy and crystal field anisotropy energy of the $DyFe_2$ layers. Indeed, it is the latter, which pins the Fe spins in the $DyFe_2$ layers, thereby allowing this interesting transition to take place. On increasing the field still further, the magnetic moment stays constant until $B_{app} = -B_{irr}$. At this point, the system becomes unstable. The $DyFe_2$ layers switch to the direction of the field, accompanied by the simultaneous creation of magnetic exchange springs in the YFe_2 layers. Finally, when all the $DyFe_2$ layers have been flipped irreversibly, the spins take the configuration shown in Fig. 8.11.c.

8.4 Metastable state in negative coercivity samples

8.4.1 Experimental results

The magnetometry measurements reported in this section, were performed on a 'YFe_2 dominated' multilayer film [60 Å $DyFe_2$ / 240 Å YFe_2] × 13, with the field applied along the [001] direction. The results for selected temperatures within the range 10 K – 120 K are shown in Fig. 8.12.

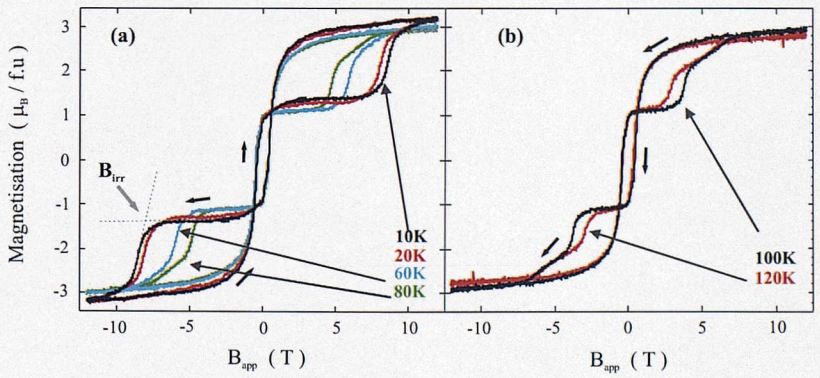

Figure 8.12 Selected hysteresis loop of [60 Å $DyFe_2$ / 240 Å YFe_2] × 13 when: **a)** the temperature T is below 80 K **b)** the temperature T is above 100 K. The field is applied in the [001] direction.

The results for temperature over 150 K are not shown here because the reorientation of the $DyFe_2$ easy axis above that temperature, generates an extra degree of complexity.

From an examination of the magnetic loops shown in Fig. 8.12, it will be observed that there are clear differences in the magnetisation curves at 10 K and 100 K. For measurements performed at 100 K and above (Fig. 8.12.b), the M-B loop is still characterised by a negative coercivity. However, this time a double step in magnetisation is observed. Similar behaviour was observed for the multilayers [50 Å $DyFe_2$ / 200 Å YFe_2] × 17 and [55 Å $DyFe_2$ / 220 Å YFe_2] × 15. The feature is highlighted in Fig. 8.13, where the first derivative of the magnetisation versus the applied field dM / dB_{app} is displayed.

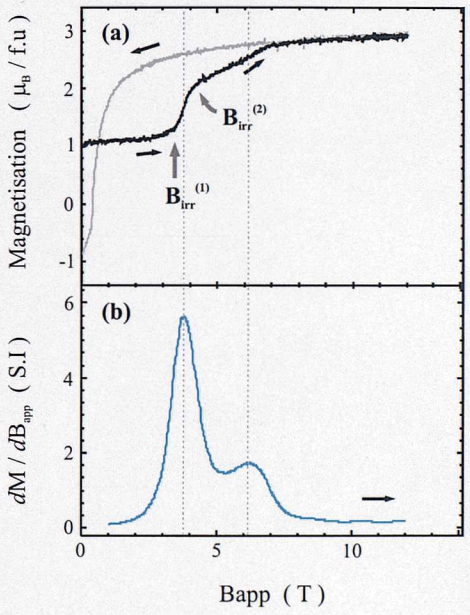

Figure 8.13 Magnetic behaviour of the multilayer [60 Å $DyFe_2$ / 240 Å YFe_2] × 13 at 100 K.
a) Hysteresis loop for positive applied field B_{app}.
b) First derivative of the magnetisation M versus B_{app}. M is the magnetisation when the field is swept from 0 to +12 T.

The first jump of magnetisation, which occurs for field larger than $B_{irr}^{(1)}$ ~ 3.4 T, is much sharper than the second one, which takes place from $B_{irr}^{(2)}$ ~ 4.12 T. Also it can be seen that each jump give rise to a magnetisation enhance of ~0.9 μ_B / f.u each.

To investigate the magnetisation reversal further, partial hysteresis loops were obtained. The results are shown in Fig. 8.14.

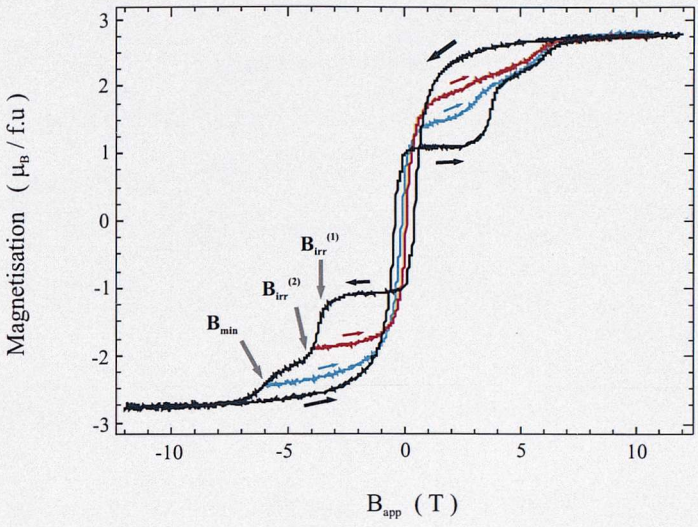

Figure 8.14 Partial hysteresis loop of the sample [60 Å $DyFe_2$ / 240 Å YFe_2] × 13, at 100 K. The sample is initially saturated along [001] by applying a large positive field. B_{min} is the maximum reversal field of the minor loop: B_{min} = -4 T, -6 T and -12 T.

After having saturated the film in a high magnetic field of +12 T, directed towards [001], the field is reduced to 0 T. It is found M = 0 for B_{app} = +0.43 T, *i.e.* a negative coercivity B_C of -0.43 T. B_{app} is subsequently reversed to a maximum reversal field B_{min}, and the field is increased back to +12 T. It is found that the multilayer exhibits different magnetic behaviour, as a function of B_{min}.

- For $B_{min} \geq - B_{irr}^{(1)}$

The hysteresis loop is reversible. All the $DyFe_2$ moments are pinned along the field, and the exchange springs created in the soft layer at high field unwind when the field is reduced. For B_{app} in the range $0 \geq B_{app} \geq - B_{irr}^{(1)}$, the sample is in the AFM state, the $DyFe_2$ moments point along [001], and YFe_2 moments are directed towards $[00\bar{1}]$.

- For $- B_{irr}^{(1)} \geq B_{min} \geq - B_{irr}^{(2)}$

An irreversible and sharp decrease of the magnetisation occurs from when the applied field is over $- B_{irr}^{(1)}$. When $B_{app} = - B_{irr}^{(2)}$, the field is reduced to zero, and the

magnetisation curve crosses the axis of zero magnetisation at practically zero field. In positive field regime, the magnetisation continues increasing, and the plateau of magnetisation characteristic of the AFM state is not observed anymore.

- For $B_{min} < - B_{irr}^{(2)}$

The magnetisation progressively decreases in an irreversible manner. When the field is reduced back to zero, the minor loop crosses the zero magnetisation axis at $B_{app} \sim -0.15$ T. When B_{min} is over 10 T, the remanent magnetisation decreases and the magnetisation branch in the first quadrant of the M-B curve gradually approaches the plateau of magnetisation, associated with the AFM state.

8.4.2 Discussion

In this section, an interpretation of the M-B loop of negative coercivity samples at 100 K is provided. Fig. 8.15 displays the spin configuration in the material for selected applied field.

At +12 T, the minimum energy state is achieved with the net moment of the $DyFe_2$ layers pointing along the applied field $B_{app} \parallel [001]$, and the formation of magnetic exchange springs in the YFe_2 layers (Fig. 8.15.a).

As the strength of the applied field is reduced, the magnetic exchange springs unwinds until the applied field reaches a critical bending field B_B. The system finally stabilizes in the AFM state: the $DyFe_2$ moments are along [001] and the YFe_2 moments are along $[00\bar{1}]$ direction (Fig. 8.15.b). Upon increasing the reversed field over $B_{irr}^{(1)}$, the $DyFe_2$ moments switch irreversibly to an in-plane direction 90° away from of [001], *i.e.* $[\bar{1}10]$ or $[1\bar{1}0]$. Simultaneously, $(0 \rightarrow 90°)$ magnetic exchange springs develops in the YFe_2 layers. This must be related to the magnetic behaviour of the epitaxial $DyFe_2$ compound. Indeed, it was seen in chapter 5 that the easy axis of the epitaxial $DyFe_2$ film is temperature dependent.

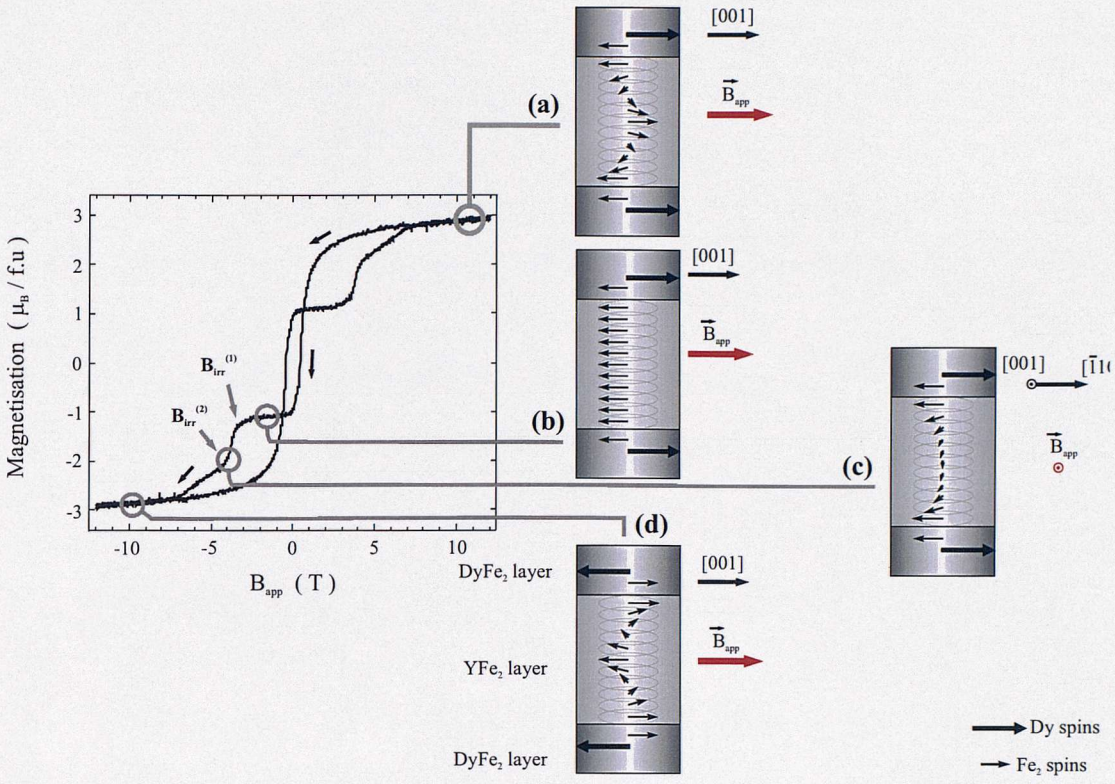

Figure 8.15 Schematic representations of the magnetic moments and exchange springs in the configuration [60 Å $DyFe_2$ / 240 Å YFe_2] × 13 multilayer film for different value of the magnetic field (a, b, c, d).

At low temperatures, the easy axis is the in-plane [001] direction, and at room temperature it is the [$\bar{1}$10] direction. It was also found that [$\bar{1}$10] and [001] are almost equivalent direction of easy magnetisation.

Note that according to the initial misalignment between $\vec{B}_{app}$ and [001], $DyFe_2$ moments in the multilayer film will preferably switch to either the [$\bar{1}$10] or [1 $\bar{1}$0] direction. The magnetisation reversal is likely to occur by domain wall motion, because the sample exhibits a sharp increase of magnetisation, characteristic of that mechanism.

At $B_{app} = - B_{irr}^{(2)}$, all the $DyFe_2$ moments are polarised perpendicular to the applied field (Fig. 8.15.c). If the B_{app} is swept back to 0, the ($0 \rightarrow 90°$), the exchange springs unwinds. At zero applied field, the system is in the AFM state, but aligned along an in-plane [$\bar{1}$10] or [1 $\bar{1}$0] direction. Experimentally, the measured magnetisation was practically equal to zero. This may be due to the geometry of the VSM employed for

the measurements. Only the component of the net magnetic moment parallel to the field can be measured. Thus, the transverse magnetic moment is to all intents and purposes, invisible.

When the field is decreased over $-B_{irr}^{(2)}$, the $[\bar{1}10]$ or $[1\bar{1}0]$ AFM state becomes unstable. The $DyFe_2$ moments rotate irreversibly towards the direction of the reversed field, *i.e.* $[00\bar{1}]$. At the same time, the $(0 \rightarrow 90°)$ magnetic exchange springs in the soft layers become $(0 \rightarrow 180°)$ magnetic exchange springs (Fig. 8.15.d). The irreversible decrease of magnetisation is progressive which implies that the magnetisation reversal occurs primarily by coherent rotation of the magnetisation.

The contrast between the sharp magnetisation reversal from $-B_{irr}^{(1)}$ to $-B_{irr}^{(2)}$, followed by the slower magnetisation reversal from $-B_{irr}^{(2)}$ to saturation, suggests that the magnetisation switching from [001] to $[\bar{1}10]$ is not equivalent to the switching from $[\bar{1}10]$ to [001]. Thus, it implies that in the negative coercivity multilayer film, the directions [001] and $[\bar{1}10]$ are not energetically equivalent at 100 K. $[\bar{1}10]$ axis is the direction of minimum energy, whereas [001] is a local minimum of energy. Further support for this interpretation can be gleaned from the hysteresis loop shown in Fig. 8.16.

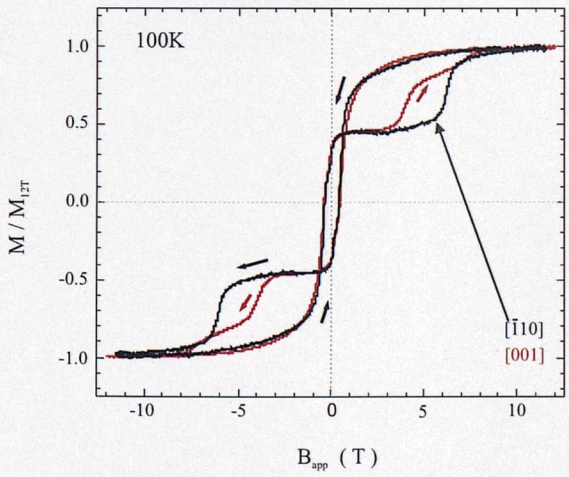

Figure 8.16 Hysteresis loop of [60 Å $DyFe_2$ / 240 Å YFe_2] × 15 at 100 K, when the field is applied parallel to [001] and when it is applied parallel to $[\bar{1}10]$. The magnetisation is normalised by the value of the magnetisation at 12 T.

This diagram shows loops obtained at 100 K for fields applied along [$\bar{1}$10] and [001] axes respectively, for the [60 Å $DyFe_2$ / 240 Å YFe_2] × 13 multilayer film. If [001] and [$\bar{1}$ 10] are assumed to be energetically equivalent crystallographic direction, then magnetic measurements on the magnetic film when $\vec{B}_{app}$ is along [$\bar{1}$ 10] should result to a double magnetisation step similar to that obtained when $\vec{B}_{app}$ is along [001]. However, it is found that the M-B loop for B_{app} ∥ [$\bar{1}$ 10] presents a shape very similar to that of the sample at 10 K when the field is applied along [001]. There is a single switching field B_{irr} = 5.49 T, which is larger than $B_{irr}^{(1)}$ = 3.34 T and $B_{irr}^{(1)}$ = 4.46 T found from the [001] experiments.

In summary, the experiments clearly show that when B_{app} ∥ [$\bar{1}$ 10], there is no metastable state or second step in the reversal of the magnetisation. The magnetic moments switch from [$\bar{1}$ 10] to [1 $\bar{1}$ 0] in an irreversible manner.

8.5 Tailoring magnetically compensated $DyFe_2$ - YFe_2 superlattices

8.5.1 Experimental results and discussion

This section presents magnetic characterisation of the superlattice film [75 Å $DyFe_2$ / 150 Å YFe_2] × 18. The hysteresis loops at selected temperature from 120 K down to 10 K are reported in Fig. 8.17.

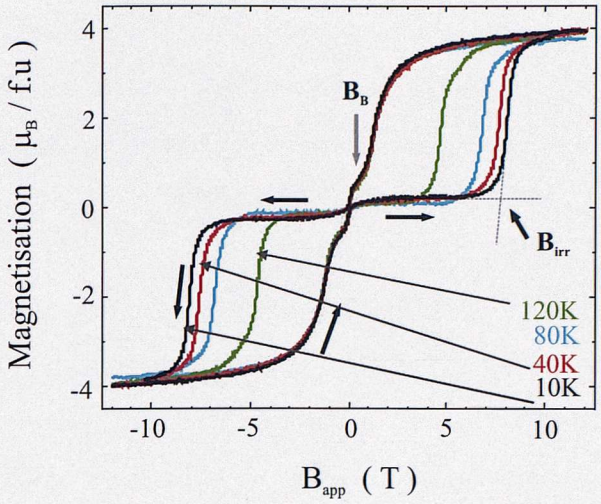

Figure 8.17 Selection of in plane magnetisation curves for the sample [75 Å $DyFe_2$ / 150 Å YFe_2] × 18.

The spin configurations of the magnetic exchange springs multilayer, as a function of the applied magnetic field is described in what follows.

After having saturated the film in large positive magnetic field in excess of 12 T, the magnetic field is reduced to zero. It can be seen that the multilayer is magnetically compensated. It displays a remanent magnetisation $M_{rem} \sim 0\ \mu_B$ / f.u at all temperatures in the range 10 K – 300 K. At zero applied field the minimum energy configuration is a simple AFM spin arrangement with the $DyFe_2$ moments (~ 7 μ_B / f.u) pointing in the direction of positive magnetic field. Because of the strong Fe - Fe exchange field, the Fe moments in both the $DyFe_2$ and YFe_2 layers are constrained to be parallel to each other, and antiparallel to the Dy moments. Consequently, the YFe_2 moments (~ 3 μ_B / f.u) lie AFM to the $DyFe_2$. As a result of the AFM spin configuration of the system at zero field, the net magnetisation of the soft layers cancel that of the hard layers. So, it is possible to balance the net magnetic moments associated with the Dy and Fe atoms in a digital fashion.

The AFM state holds from 0 T up to $-B_{irr}$, where B_{irr} is the field associated with the irreversible switching of the $DyFe_2$ layers. Note that B_{irr} is much larger than B_C, which is practically equal to zero. When the reversed applied field is increased beyond $-B_{irr}$, the $DyFe_2$ moments switch and exchange springs develop simultaneously in the YFe_2 layers. When the field is decreased to zero, the exchange

springs unwind, reaching the AFM state when the field falls below the bending field $B_B \sim 0.9$ T. It is interesting to note that the magnetisation is entirely confined to the top right and bottom left quadrants of the magnetisation loop. The formation of exchange springs gives rise to a magnetic enhancement of over 400 % in a field of 12 T.

In ordinary FM, DW's develop in the material in order to decrease the energy of the system. But in [75 Å $DyFe_2$ / 150 Å YFe_2] × 18 multilayer film, the remanent magnetisation is equal to zero, which means that the system is already in the lower state energy. Then, there is no need for DW's to form. This feature could have practical applications in hard drive technology.

8.5.2 Possible practical application

FM - AFM arrangements are nowadays implemented as basic elements in magnetic recording media, where the AFM layer is used as a pinning system [28]. Devices based on such structures are revolutionizing electronic data storage. In particular, Magnetic Random Access Memories (MRAM's), are standard in magnetic storage having replaced the semi-conductor based Dynamic Random-Access Memories (DRAM's). The advantages of MRAM's include non-volatility (they retain information when the computer is switched off), high storage density, and low energy consumption.

Nowadays, magnetic storage media are thin films of magnetic materials. The ideal system must support high density recording area. In other words, the magnetic media must be very thin with small grain size, exhibit high magnetisation, possess reasonable coercivity, and have a well defined direction of easy magnetisation [28]. However, there are limits to a continually increasing bit area density. Indeed, very thin films with a low density of magnetic particles may approach the *superparamagnet limit*, where the thermal energy k_BT approaches the anisotropy energy K_H δV. Another issue is that of the coupling between neighbouring bits. Bits which have different directions of magnetisation create a torque on one another causing some bits to lose their initial magnetisation direction, and hence information.

One way of avoiding this problem is to use thin magnetically compensated films. In such systems, magnetic bits cannot interact with other. Yet the information contained in the bits can be revealed via the creation of magnetic exchange springs. Thus, the bilayer film [75 Å $DyFe_2$ / 150 Å YFe_2] could constitute an interesting system as a compensation point sample.

Consider a single domain bit of the bilayer [75 Å $DyFe_2$ / 150 Å YFe_2]. The data stored in the magnetic bit is related to its exchange springs magnetic polarisation as displayed in Fig. 8.18. Thus, the branch of the loop shown in Fig. 8.18.a has a positive magnetisation M in positive applied field. Bit '1' is ascribed to this state. Likewise the branch of the loop shown in Fig. 8.18.b has a negative magnetisation, in negative applied fields, which we ascribe as bit '0'.

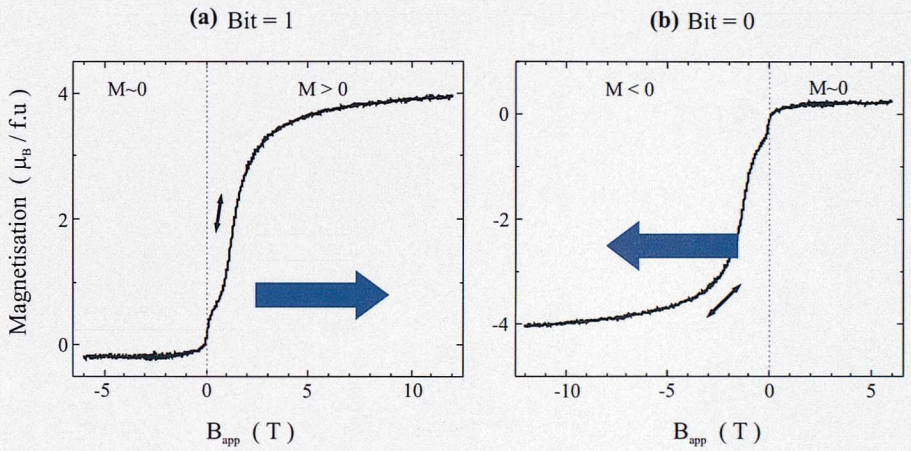

Figure 8.18 Possible association of the magnetic state of the film with bit-data. The blue arrows show the direction of the $DyFe_2$ magnetic moments.

In zero applied field, where there is no net magnetisation, the domain cell cannot exert any torque on neighbouring bits. The question then remains what sort of sensor must be used to reveal the data stored on the domain bits?

One possibility is to attach a magnet to the sensor. When the sensor approaches the magnetic cell to read the information, a small read field B_{app} is applied. This field is swept from negative to positive value. The field must be smaller than a critical field B_{irr}. If the sensor measures that:

- for $B_{app} > 0$, M increases in value and for $B_{app} < 0$, M is constant. The bit is '1'.
- for $B_{app} > 0$, M is constant, and for $B_{app} < 0$, M decreases. The bit is '0'.

Once, the sensor has read the information in the cluster, the field is reduced to zero and the net magnetisation comes back to zero.
Because the compensation point is relatively independent of the temperature, data stored in this way should be relatively stable.

8.6 Conclusions

Magnetic exchange springs have been shown to have a major influence upon the coercive field B_C and on the irreversible switching field B_{irr} of the hard phase. They can reduce significantly the coercive field.
The coercivity is usually a parameter associated with reversal of the magnetisation, which originates from effects such as magneto-elastic in lattice clamping, imperfections and lattice defects. However, in $DyFe_2$ / YFe_2 multilayers with thick YFe_2 layers, the negative coercivity is caused primarily by the properties of the exchange springs in the soft phase. This feature dominates the magnetic profile of the structures, and it allows thin films with negative coercive field and magnetically compensation to be engineered.

In an earlier chapter, it was shown that for YFe_2 dominated samples, the irreversible switching of the film is best described by WDWP model, in contrast to that of $DyFe_2$ dominated samples for which the process is best described by SDWP model. Due to the critical influence of the nucleation of the Bloch-type wall in the YFe_2 layers, the usual form of the Stoner and Wohlfarth model (Eq. 6.12) cannot be used to describe the irreversible switching of the magnetic moment of the multilayer film.
It has also been proved that the irreversible switching of the negative coercivity samples occurs with the help of a metastable state aligned along a $[\bar{1}10]$ direction. Arguments have been presented which show that the reversal of the YFe_2 dominated $DyFe_2$ / YFe_2 film at 100 K is accomplished in two steps. The first step is associated

with an irreversible jump from [001] to $[\bar{1}10]$ direction, while the 2nd step is related to the reorientation of the moment from $[\bar{1}10]$ to $[00\bar{1}]$. Indeed, it has been argued that in the multilayer under discussion the $[\bar{1}10]$ direction is energetically lower than that of the [001] axis, usually regarded as the direction of easy magnetisation in the $DyFe_2$ layers below 100 K.

References

[1] W. H. Meiklejohn, *J. Appl. Phys.* **33**: 1328 (1962)
C. P. Bean in: C. A. Neugebauer, J. B. Newkirk, D. A. Vermilyea (Eds.), *Structure and properties of Thin Films*, Wiley, New York, p. 331 (1960)
W. H. Meiklejohn and C. P. Bean, *Phys. Rev.* **105**: 904 (1957)

[2] B. Dieny *et al.*, *Phys. Rev. B* **43**: 1297 (1991)

[3] M. N. Baibich *et al.*, *Phys. Rev. Lett.* **61**: 2472 (1988)

[4] J. C. S. Kools, *I. E. E. E. Trans. Magn.* **32**: 3165 (1996)

[5] E. P. Wohlfarth, *Adv. Phys.* **8**: 87 (1959)
H. Schmid, *Cobalt* **6**: 8 (1960)

[6] I. S. Jacobs, G. T. Rado, H. Suhl (Eds.), *Magnetism*, Academic Press, N. Y., p.271 (1963)

[7] A. Yelon, M. H. Francombe, R. W. Hoffman (Eds.), *Physics of Thin Films*, vol. 6, Academic Press, N. Y, p.205 (1961)

[8] J. S. Kouvel, *J. Phys. Chem. Sol.* **24**: 795 (1963)

[9] N. H. March *et al.*, *J. Magn. Magn. Mater.* **44**: 1 (1984)

[10] K. Fukamicki, *J. Magn. Soc. Japan* **21**: 1062 (1997)

[11] R. Jungblut *et al.*, *J. Appl. Phys.* **75**: 6659 (1994)

[12] M. Takahashi *et al.*, *Jpn J. Appl. Phys.* **19**: 1093 (1980)

[13] C. Tang, *J. Appl. Phys.* **55**: 2226 (1984)

[14] A. P. Malozemoff, *J. Appl. Phys.* **63**: 3874 (1988)
D. Mauri *et al.*, *J. Appl. Phys.* **62**: 3047 (1987)
S. Soeya *et al.*, *J. Appl. Phys.* **76**: 5356 (1994)

[15] A. J. Devasahayam and M. H. Kryder, *I. E. E. E. Trans. Magn.* **31**: 3820 (1995)

[16] J. X. Shen and M. T. Kief, *J. Appl. Phys.* **79**: 5008 (1996)

[17] P. J. van der Zaag *et al.*, *J. Appl. Phys.* **79**: 5103 (1996)

[18] D. H. Han *et al.*, *J. Appl. Phys.* **81**: 340 (1997)

[19] T. J. Moran *et al.*, *J. Appl. Phys.* **78**: 1887 (1995)

[20] W. van Roy *et al.*, *J. Magn. Magn. Magn. Mater.* **165**: 149 (1997)

[21] T. Kobayashi *et al.*, *Jpn. J. Appl. Phys.* **20**: 2089 (1981)

[22] H. Tsujimoto and Y. Saburai, *Jpn J. Appl. Phys.* **22**: 1845 (1983)

[23] N. Smith and W. C. Cain, *J. Appl. Phys.* **69**: 2471 (1991)

[24] A. Aharomi, *J. Appl. Phys.* **76**: 6977 (1994)

[25] C. Gao and M. J. O' Shea, *J. Magn. Magn. Mater.* **127**: 181 (1993)

[26] M. J. O' Shea and A. L. Al-Shariff, *J. Appl. Phys.* **75**: 6673 (1994)

[27] P. Gaunt, *Philos. Mag. B* **48**: 261 (1993)
P. Gaunt, *J. App. Phys.* **59**: 4129, 12 (1986)

[28] R. J. Astalos, *Phys. Rev. B* **58**: 13 (1998)
T. Ando *et al.*, *I. E. E. E. Trans. Magn.* **33**: 5 (1997)
G. A. Prinz, *Phys. Today* **48**: 24-25 (1995)

Chapter 9

Summary

The aim of this research project was to study the magnetic properties of Laves phase multilayer and alloy films, grown by Molecular Beam Epitaxy on top of a (110) Nb $(11\bar{2}0)$ sapphire substrate structure.

The epitaxial structures which are single-crystal in nature, possess directions of easy magnetisation which differ from their respective bulk compounds. In particular, because the RE-Fe_2 compounds are characterised by giant magnetostriction, strains built into the Laves phase structure during the crystal growth procedure, profoundly modify the direction of easy magnetisation. Magnetic measurements on epitaxial films of the highly magnetostrictive materials $DyFe_2$ and $TbFe_2$ showed that the epitaxial strain influences the direction of easy magnetisation. The MBE films exhibit a re-orientation of their easy axis which is temperature dependent. This magnetic feature is associated with the different thermal evolution of the magneto-crystalline anisotropy constants and the magneto-elastic coupling coefficient.

At low temperature, the easy axis of the epitaxial $DyFe_2$ film for example is found to be the same than the easy axis of the bulk *i.e.* [001]. However, at room temperature, the magnetostriction term which favors $[\bar{1}10]$ as easy axis [1], becomes significant and determines the axis of easy magnetisation. Similar effects were observed for $TbFe_2$ films. In contrast, for the YFe_2 Laves phase compound, which is unsensitive to stress, the easy axis remains temperature independent.

Another example of the significant effect of the epitaxial strain upon the magnetic properties of the materials can be clearly observed in the magnetic characterization of

the strongly magnetostrictive $Dy_{(1-x)}\,Tb_x\,Fe_2$ epitaxial alloy. Indeed, it has been found by A. E. Clark *et al.* that $Dy_{(1-x)}\,Tb_x\,Fe_2$ alloy bulk showed a minimum of coercivity for $x = 0.3$ [2]. In contrast, the epitaxial film shows a linear dependence of the coercivity B_C with the relative concentration x. The maximum of coercivity is displayed by the $TbFe_2$ film and the minimum by the $DyFe_2$ film. The magnetisation reversal mechanism can be successfully described by Stoner and Wohlfarth model, which is based on the principle of coherent rotation of the magnetisation [3]. Adjusting the model to multilayer composites, B_C can be successfully predicted by:

$$B_C = \frac{K_1 t_1 + K_2 t_2}{M_1 t_1 + M_2 t_2} \tag{9.01}$$

where the parameters possess their usual meaning, and the indices refer to the different components of the film.

The $DyFe_2 - YFe_2$ superlattices are layered magnetic systems consisting of two single crystalline Laves phase compounds, with very close crystal structures, but with different magnetic behaviour. In $DyFe_2$, the Dysprosium and Iron moments are aligned anti-parallel. It is a hard magnetic material characterised by large anisotropy and saturation magnetisation. By contrast, YFe_2 is a typical soft phase with negligible anisotropy and relatively small magnetisation. The exchange coupling at the interface between the two compounds arises via positive exchange between Iron moments. Thus, the system is a kind of *giant* ferrimagnet where the net magnetisation in the $DyFe_2$ and YFe_2 compounds is anti-parallel.

If the soft layer is sufficiently thin, the net magnetisation remains rigidly coupled to that of the hard layer and the composite film reverses as a coherent unit at a coercive field B_C. For such composites, the prediction of the Stoner and Wohlfarth model is in reasonable agreement with experiments. Consequently, by adjusting ratio and thickness of the layers accordingly, it is possible to tailor the coercivity B_C of the MBE grown $DyFe_2$ - YFe_2 multilayer films. However, it should be noted that while the coherent rotation model allows prediction of B_C to be made, the temperature dependence of the coercivity suggests that the magnetisation reversal occurs via domain walls, as expected. In particular, it was shown that the coercivity is affected by strong domain wall pinning (SDWP) [4].

When the thickness of the magnetically soft layers is increased, magnetic exchange springs can be created. Here, the Fe spins at the hard/soft phase interface are pinned by the magnetically hard $DyFe_2$ layers, while the Fe spins in the magnetic exchange springs rotate towards the direction of the applied magnetic field. The anti-ferromagnetically coupled $DyFe_2$ / YFe_2 layered structure provides a realization of the ideal nanostructure of symmetric exchange-springs magnets. The exchange springs profoundly modifies the properties of the magnetic loops. In particular, it gives rise to an additional magnetic moment in the high field region, which is fully reversible, a classic signature of a magnetic exchange springs. The magnetisation behaviour of an exchange springs film can be characterised by two fields, known as the bending field B_B and the irreversible field B_{irr}. For

- $B_{app} < B_{irr}$, the soft layer remains anti-parallel to the hard layer
- $B_{app} > B_{irr}$, the magnetic reversal proceeds via an irreversible switches of the magnetisation in the hard layer and the simultaneous creation of the magnetic exchange springs.
- $B_{app} > B_B$, the applied field creates a sufficiently large torque on the Fe moments so that the gain in Zeeman energy from rotation of Fe magnetic spins in the YFe_2 blocks outweights the concomitant loss in magnetic exchange energy.

From the theoretical point of view, a very simple relationship was established for the bending field B_B, the Fe-Fe exchange field B_{ex}, and the number of mono-atomic layers in the YFe_2 phase N [5]. Namely:

$$B_B = B_{ex}\left(\frac{\pi}{N}\right)^2 \tag{9.02}$$

This result, based on (*i*) an essentially 1-D model and (*ii*) infinite pinning at the $DyFe_2$ / YFe_2 interfaces, can be used as a guide.

It is possible to tune the magnetic exchange springs in the magnetically soft YFe_2 layers to produce films with: $B_B > B_C$, $B_B < B_C$, and $B_B \sim B_C$.

In addition, it is found that the magnetic exchange springs strongly influence the switching field (B_{irr})of the hard layer. It was shown that B_{irr} changes linearly with the temperature, and this result suggests that magnetisation reversal occurs by motions of domain walls perturbed by weak domain wall pinning (WDWP) centers [4]. The

evolution from WDWP centers, found in exchange springs multilayers, to SDWP found in strongly coupled multilayers can be explained by the competition between localized strong magneto-crystalline anisotropy of the $DyFe_2$ and exchange interaction Fe-Fe. For increasing thickness of YFe_2 layers, the Fe-Fe exchange interactions smooth out the strong magneto-crystalline anisotropy.

However, it is worth noting that the model does not take into account influences such as next nearest neighbour interactions and the possibility that the exchange spring may extend into the $DyFe_2$ layers. The latter effect is particularly important because it implies that the actual thickness for the creation of the magnetic exchange springs is larger than the thickness of the YFe_2 layer and hence B_B is smaller.

Using traditional magnetometry techniques it is impossible to probe the penetration of magnetic exchange springs. Static magnetisation measurement techniques only measure the average magnetic moment from the entire multilayer film. Therefore, because the magnetic profile within the $DyFe_2$ layers should reflect the degree of spring penetration, the technique to be used must allow independent measurements of the hysteresis loops of the different component layers. C. T. Chen *et al.* [6] have developed such a method to determine element-specific hysteresis loops of heteromagnetic materials. By recording the absorption intensity of circular polarized soft X-Rays at each transition metal L3 absorption edge as a function of applied field, the hysteretic behaviour of each magnetic element in a compound or multilayer structure can be determined using magnetic circular dichroism (MCD) [7].

It should also be mentioned that local variations in the $DyFe_2$ anisotropy due to interface roughness in particular, could influence the reversal behaviour. However, it is difficult to obtain unambiguous information on the magnetic structure of surfaces and interfaces. One method of investigating surface and interface magnetism, which has proven useful in studies of ferromagnetic films, is to probe the spin-wave the magnetic moments at each site precess about their individual equilibrium directions. Since the spins are coupled with one another through exchange and dipolar interactions, spin-wave excitations are the eigen-modes of the magnetic system. Thus the frequency of a spin wave may depend quite sensitively on the exchange coupling between spins as well as other effective fields caused by, for example, anisotropies and magneto-elastic effects. These interactions will not only affect the frequency of

precession but also the relative phase precession between spins at neighbouring lattice sites. In ferromagnetic systems such as Fe and Co the lowest spin-wave frequencies are typically of the order of 10 GHz. These are long wavelength excitations which can be studied using ferromagnetic resonance and Brillouin light scattering [8].

To date, most of the 'model calculations' of magnetic exchange springs have been carried out on the assumption that the spins remain confined to the plane of the film. However, recent measurements on the uniaxial in-plane anisotropy SmCo/Fe exchange springs films show that at high field, the magnetisation rotation created in the magnetically soft Fe layers is an out-of-plane fanning mode [9].

The $DyFe_2 - YFe_2$ structure constitutes an interesting example of how novel magnetic phases can be engineered by tuning the interfacial interaction. The present work paves the way for experiments on more magnetically complicated systems consisting of magnetostrictive multilayer materials. Indeed, combining giant magnetostrictive and high susceptibility / high moment materials is promising, as most giant magnetostrictive alloys require large fields to achieve a large magnetostriction [10]. Previous attempts to reduce the switching field have focused on reducing the anisotropy by either alloying Dy to control the Tb / Dy ratio in order to achieve compensation of fourth order anisotropy $[(Tb_{0.3}Dy_{0.7})Fe_2]$ [1]. The multilayer approach to increase the magnetostrictive susceptibility $d\lambda / dB_{app}$ is based on the exchange-spring-magnet concept [11]. Using this approach, the switching field ($\propto K_S / M_S$) is reduced by increasing M_S, a degree of freedom otherwise limited in single films [12].

Finally, the exchange springs multilayer serves as an ideal model system for studying the whole process of the nucleation, compression, decompression and propagation of an artificial in-plane domain wall. In particular, it can be used to investigate Giant Magneto-Resistance (GMR) effect due to magnetic exchange springs. In particular, Gordeev *et al.* [13] have shown that up to 12 % GMR due to the formation of short magnetic exchange springs in the magnetically soft YFe_2 layers can be achieved. The results were explained in terms of the domain wall scattering model, developed by Levy and Zhang [14].

References

[1] A. Mougin *et al.*, *Phys. Rev. B* **62**: 9517 (2000)

[2] A. E. Clark, *Ferromagnetic Materials*, edited by E. P. Wohlfarth (North-Holland, Amsterdam) (1980)

[3] E. C. Stoner and E. P. Wohlfarth, *Phil. Trans. R. Soc.* **240**: 599-642 (1948)

[4] P. Gaunt, *Philos. Mag. B* **48**: 261 (1993)
P. Gaunt *et al.*, *J. App. Phys.* **59**: 4129, 12 (1986)

[5] Bowden *et al.*, *J. Phys. Condens. Mater.* **12**: 9335-9346 (2000)

[6] C. T. Chen, *Phys. Rev. B* **48**: 642 (1993)

[7] L. H. Tjeng, *J. Magn. Magn. Mater.* **109**: 288 (1992)
J. G. Tobin *et al.*, *Phys. Rev. Lett.* **68**: 3642 (1992)
Y. Wu *et al.*, *Phys. Rev. Lett.* **69**: 2307 (1992)
Y. U. Idzerda *et al.*, *J. Magn. Magn. Mater.* **127**: 109 (1993)
Y. U. Idzerda *et al.*, *Phys. Rev. B* **48**: 4144 (1993)

[8] P. Grunberg, *Light Scattering in Solids* **V** (*ed.* M. Cardona and G. Guntherodt (Berlin: Springer)) (1989)
C. E. Patton, *Phys. Rev.* **103**: 251 (1984)
B. Hillebrands, and G. Guntherodt, *Ultrathin Magnetic Structures* **II** (*ed.* J. A. C. Bland and B. Heinrich (Berlin: Springer)) (1993)
M. Grimsditch, *Light Scattering in Solids* **V**, *ed.* M. Cardona and G. Guntherodt (Berlin: Springer) (1989)
A. S. Borovik-Romanov, and N. M. Kreines, *Spin Waves and Magnetic Excitations*, *ed.* A.S. Borovik-Romanov and S.K. Sinha (Amsterdam: Elsevier) (1988)

[9] J. S. Jiang *et al.*, *J. Phys. D: Appl. Phys.* **35**: 2339 (2002)

[10] Y. S. Choi *et al.*, *J. Appl. Phys.* **83**: 7270 (1998)

[11] E. Kneller and K. Hawig, *I. E. E. E. Trans. Magn.* **27**: 3588 (1991)

[12] E. Quandt *et al.*, *J. Appl. Phys.* **81**: 5420 (1997)
E. Quandt *et al.*, *J. Appl. Phys.* **83** (11): 7267 (1998)

[13] S. Gordeev *et al.*, *Phys. Rev. Lett.* **87**: 186808 (2001)

[14] P. M. Levy and S. Zhang, *Phys. Rev. Lett.* **79**: 5110 (1997)

Appendix

Appendix 1

Conversion of the measured magnetisation in Bohr magneton per formula unit

A Bohr magneton, μ_B, is the magnetic moment carried by a single electron: $1\mu_B = 9.274 \times 10^{-21}$ emu. The output of the magnetometry measurement on a magnetic sample, using a VSM, is the average magnetisation expressed in emu. It is a function of the total volume V_T of the specimen. However, to compare different samples, it is more appropriate to express the magnetisation in a unit independent of the specimen volume, hence the choice of the Bohr magneton per formula unit (μ_B / f.u).

The first step consists in determining the total volume V_T of the magnetic sample, which has the form of a cylinder of surface area A:

$$V_T = m\omega_m A + n\omega_n A \qquad (1)$$

Total volume of $(RE\text{-}Fe_2)_1$ component

Total volume of $(RE\text{-}Fe_2)_2$ component

m (n) is the number of repeats of the $(RE\text{-}Fe_2)_1$ ($(RE\text{-}Fe_2)_2$) single layer, and ω_m (ω_n) the thickness, respectively.

A typical $RE\text{-}Fe_2$ Laves phase unit cell with a lattice parameter L is shown in Fig. 1.

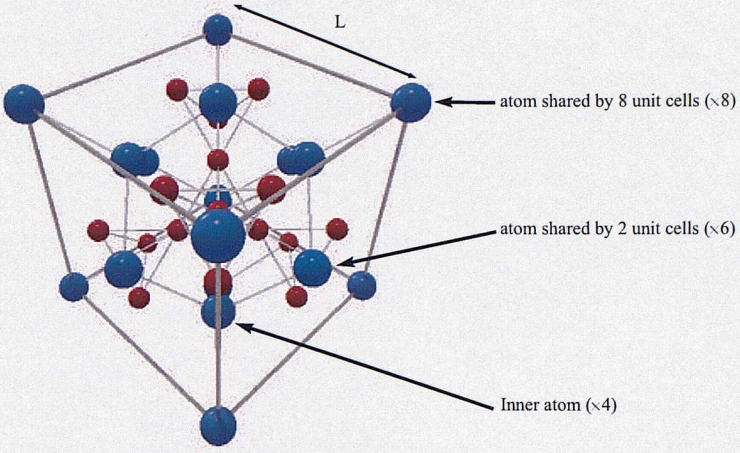

Figure A.1 Typical Laves phase unit cell.

The unit cell contains an average of 8 RE atoms and 16 Fe atoms. Hence, there are 8 formula units in a single Laves phase unit cell.

The number N_i of $(RE\text{-}Fe_2)_i$ (i = 1 or 2) formula unit in the sample is given by:

$$N_i = i\frac{\omega_i A}{(L_i)^3}\times 8 \qquad (2)$$

Finally, the measured magnetisation in emu ($M_{[emu]}$) can be converted in Bohr magneton per formula unit ($M_{[\mu_B]}$) using the following equation:

$$M_{[\mu_B]} = \frac{M_{[emu]}}{(N_1 + N_2)\times \mu_B} \qquad (3)$$

Appendix 2

Estimation of the domain wall width of the $DyFe_2$ / YFe_2 multilayer films

The width δ of a domain wall (DW) in a ferromagnet is governed by the competition between the exchange energy and the anisotropy energy:

$$\delta = \pi\sqrt{\frac{2A}{K_1}} \tag{4}$$

A and K_1 is the exchange constant and the first order anisotropy constant respectively [1]. The exchange constant for the Laves phase materials is related to the exchange integrals $J_{RE\text{-}RE}$, $J_{RE\text{-}Fe}$ and $J_{Fe\text{-}Fe}$ (chapter 2). The largest contribution to the exchange constant is attributed to the Fe-Fe exchange interaction. Therefore, within a simplistic approximation the exchange constant A can be assumed to have a value on the order of the exchange constant of the pure Fe metal: $A = 1.3 \times 10^{-11}$ J.m^{-1} [2].

Given the magneto-crystalline anisotropy in the multilayers is driven by the hard phase, it is acceptable to allocate to K_1 the value of the $DyFe_2$ compounds: $K_1 = 4\times 10^7$ J.m^{-3} [3].

The DW width δ is found to be equal to 25 Å. This estimation seems realistic in the light of the values of the DW width found for Fe and for the permanent magnet $Nd_2Fe_{14}B$ (heavy Rare-earth rich): $\delta_{Fe} = 400$ Å and $\delta_{NdFeB} = 43$ Å, respectively [4].

References

[1] A. Mougin *et al.*, *Phys. Rev. B* **62**: 9517 (2000)

[2] R. F. Soohoo, *Magnetic Thin Films*, Harper International Student Reprint (1965), pp. 43-45

[3] Heider F. and W. Williams, *Geophysique Res. Lett.* **15**: 184-187 (1988)

[4] R. Skomski and J. M. Coey, *Permanent Magnetism*, Studies in Condensed Matter Physics, Institute of Physics Publishing (1999), pp. 157-161

Publications

Room temperature coercivities of $Tb_{(1-x)}Dy_xFe_2$ (110) MBE grown films.
J-M. L. Beaujour, G. J. Bowden, A. Zhukov, B. D. Rainford, P. A. J. de Groot, R. C. C. Ward, M. R. Wells, (*submitted to J. Appl. Phys.*)

Modelling the magnetic properties of $DyFe_2$ - YFe_2 superlattices
G. J. Bowden, J-M. L. Beaujour, A. Zhukov, B. D. Rainford, P. A. J. de Groot, R. C. C. Ward, M. R. Wells, (*submitted to J. Appl. Phys.*)

Vector Magnetometer studies of the easy magnetisation direction in epitaxially grown $DyFe_2$ film.
A. Zhukov, G. J. Bowden, J-M. L. Beaujour, B. D. Rainford, P. A. J. de Groot, R. C. C. Ward, M. R. Wells, (*to be submitted*)

Anisotropic magnetoresistance in an epitaxial (110) $DyFe_2$ film: a meta-stable magnetic state at 100K
J-M. L. Beaujour, G. J. Bowden, A. Zhukov, B. D. Rainford, P. A. J. de Groot, R. C. C. Ward M. R. Wells, and A. G. M. Jansen, *J. Magn. Magn. Mater. (2002) (in press)*

Some universal results for exchange spring magnets and applications to $DyFe_2$ - YFe_2 superlattices
G. J. Bowden, G. Daniell, S. Gordeev, J-M. L. Beaujour, P. A. J. de Groot, B. Rainford, R. C. C. Ward M. R. Wells, *J. Magn. Magn. Mat.* **240**: 556-558 (2002)

Giant Magnetoresistance by exchange springs $DyFe_2$ - YFe_2 superlattices
S. Gordeev, J-M. L. Beaujour, G. J. Bowden, P. A. J. de Groot, B. D. Rainford, R. C. C. Ward, M. R. Wells, and A. G. M. Jansen, *Phys. Rev. Lett.* **87**: 186808 (2001)

Spin configuration and negative coercivity in epitaxially grown $DyFe_2$ / YFe_2 superlattices
S. Gordeev, J-M. L. Beaujour, G. J. Bowden, P. A. J. de Groot, B. D. Rainford, R. C. C. Ward, M. R. Wells, *J. Appl. Phys.* **89**: 6828 (2001)

Negative coercivity in epitaxially grown (110) $DyFe_2$ - YFe_2 superlattices
J-M. L. Beaujour, G. J. Bowden, S. Gordeev, P. A. J. de Groot, B. D. Rainford, R. C. C. Ward, M. R. Wells, *Appl. Phys. Lett.* **78**: 964 (2001)

Exchange springs in YFe_2 dominated $DyFe_2$ - YFe_2 superlattices
J-M. L. Beaujour, G. J. Bowden, S. Gordeev, P. A. J. de Groot, B. D. Rainford, R. C. C. Ward, M. R. Wells, *J. Magn. Magn. Mat.* **226**: 1870-2 (2001)

Effect of exchange springs on the coercivity of $DyFe_2$ - YFe_2 superlattices
J-M. L. Beaujour, G. J. Bowden, S. Gordeev, P. A. J. de Groot, B. D. Rainford, R. C. C. Ward, M. R. Wells, *J. Magn. Magn. Mat.* **226**: 1714-6 (2001)

Discrete exchange springs in magnetic multilayer samples
G. J. Bowden, J-M. L. Beaujour, S. Gordeev, P. A. J. de Groot, B. D. Rainford, R. C. C. Ward, M. R. Wells, *J. Phys. Cond. Matt.* **12**: 9335-9346 (2000)

Exchange springs in anti-ferromagnetically coupled $DyFe_2$ - YFe_2 superlattices
M. Sawicki, G. J. Bowden, P. A. J. de Groot, B. D. Rainford, J-M. L. Beaujour, R. C. C. Ward, M. R. Wells, *Phys. Rev. B* **62**: 5817-20 (2000)

Engineering coercivity in epitaxially grown (110) films of $DyFe_2$ - YFe_2 superlattices
M. Sawicki, G. J. Bowden, P. A. J. de Groot, B. D. Rainford, J-M. L. Beaujour, R. C. C. Ward, M. R. Wells, *Appl. Phys. Lett.* **77**: 573-5 (2000)